UNIVERSITY OF KWAZULU-NATAL

A Study of the Effects of the Doping of Yttrium Barium Copper Oxide with Graphene Oxide and Reduced Graphene Oxide

by

Mohammed Zaahid Gaffoor

Supervised by:
Professor A. L. Leigh Jarvis

A thesis submitted in fulfillment for the
degree of Doctor of Philosophy in
Engineering
in the
Discipline of Electrical, Electronic and Computer Engineering,
College of Agriculture, Engineering and Science,
University of KwaZulu-Natal, Durban, South Africa

Date April 2023

Declaration of Authorship

I, MOHAMMED ZAAHID GAFFOOR, declare that this thesis titled, 'A STUDY OF THE EFFECTS OF THE DOPING OF YTTRIUM BARIUM COPPER OXIDE WITH GRAPHENE OXIDE AND REDUCED GRAPHENE OXIDE' and the work presented in it are my own. I confirm that:

- The research reported in this thesis, except where otherwise indicated, is my original work.
- This thesis has not been submitted for any degree or examination at any other university.
- This thesis does not contain other persons data, pictures, graphs or other information, unless specifically acknowledged as being sourced from other persons.
- This thesis does not contain other persons writing, unless specifically acknowledged as being sourced from other researchers. Where other written sources have been quoted, then: i) their words have been re-written, but the general information attributed to them has been referenced and ii) where their exact words have been used, their writing has been placed inside quotation marks, and referenced.
- Where I have reproduced a publication of which I am an author, co-author or editor, I have indicated in detail which part of the publication was written by myself alone and have fully referenced such publications.
- This thesis does not contain text, graphics or tables copied and pasted from the Internet, unless specifically acknowledged, and the source being detailed in the thesis and in the References Sections.

Signed: [redacted]

Date: 18/04/2023

As the candidate's supervisor, I, ALAN LAWRENCE LEIGH JARVIS, agree to the submission of this thesis.

Signed: [redacted]

Date 18/04/2023

University of Kwa-Zulu Natal

Abstract

Doctor of Philosophy in Engineering
by Mohammed Zaahid Gaffoor

High temperature superconductors (HTSs) have a wide range of both small scale and large scale electronic and electrical applications. Therefore, research is constantly being done in order to improve the properties of existing superconductors and to find new superconductors with superior properties.

Important characteristic properties, which are being investigated, range from the critical transition temperature (T_C), critical current density (J_C) to microhardness i.e. electrical to mechanical. An important system, within bulk polycrystalline HTSs material, is a network of weak links which exists at grain boundaries. This network of weak links in bulk superconductors, influences characteristic properties such as reducing the critical current density, increases the normal state resistivity and structurally weakens the bulk material.

In present work, bulk high temperature superconductor Yttrium Barium Copper Oxide, the Y123 phase ($Y_1Ba_2Cu_3O_{7-\delta}$), was doped with various concentrations of graphene oxide (GO) and reduced graphene oxide (rGO). Resistance vs. Temperature measurements were carried out in zero field and field cooling conditions to determine T_C and the effect that the doping has on the weak links at grain boundaries. The weak links has been seen to improve with both rGO and GO doping.

T_C was seen to increase with an increase in graphene oxide and reduced graphene oxide doping in the range of 0.1 to 1 %wt. This was attributed to the increase in the non-stoichiometric oxygen content due to doping. This increase in non-stoichiometric oxygen content was measured by iodometric titration and X-ray diffraction. In certain GO doped samples T_C increased above 93 K, the maximum T_C of YBCO, which cannot be attributed to an increase in oxygen content. The increase in T_C beyond 93 K led to investigations into possible GO doping pressure and impurity effects. The increase in T_C was confirmed with magnetic measurements. It was discovered that the formation of manganese particles from impurities in the GO dopant led to an increase in T_C = 101 K. The hypothesized mechanism responsible for this improvement in T_C is the increase in the CuO_2 planar buckling angle. Increase in the buckling angle results in the flattening of copper oxide planes which can be observed by the increase in surface area of the planes. These flatter planes have a more 2D structure thus resulting in an enhancement in T_C.

Micro-hardness of GO and rGO doped samples increased with increase in doping concentrations. This increase in micro-hardness was attributed to the reduction in motion of defects, which is attributed to a decrease in grain size and filling of voids and pores at grain boundaries.

Acknowledgements

I would like to thank my family for allowing me this opportunity to complete this degree and for all the support they have provided me throughout this journey. A special thank you to my supervisor, colleague and friend Prof. A.L.L Jarvis for his unwavering confidence in me to complete this research even when I did not think it was possible. Thank you to my wife (Ummul Warah) for supporting me and motivating me and to my colleagues in the material science lab Jonathan Archer and Solan Perumal I am ever so grateful for all the help and advice they have provided during my experimental procedures.

"Believe in yourself and you will succeed."

~ Fortune Cookie

List of Symbols and Units

a	Lattice parameter **(Å)**
b	Lattice parameter **(Å)**
B	Brittleness index **($m^{\frac{1}{2}}$)**
B_{hkl}	Sum of size and strain broadening
c	Lattice parameter **(Å)**
χ'	AC susceptibility **(a.u)**
d	Diagonal length of indentation **(um)**
D	Crystallite size **(um)**
d_p	Plastic deformation component from elastic plastic deformation model **(um)**
d_e	Elastic deformation component from elastic plastic deformation model **(um)**
δ	Non-stoichiometric oxygen content
E	Elastic modulus **(GPa)**
ε	Lattice strain
F	Applied load force **(N)**
F_O	Energy dissipative portion of the load **(N)**
H_{C1}	Lower critical magnetic field **(A/m)**
H_{C2}	Upper critical magnetic field **(A/m)**
H_{EPD}	Vickers hardness calculated by the elastic plastic deformation model **(GPa)**
H_{HK}	Vickers hardness calculated by the hays kendall model **(GPa)**
H_{irr}	Irreversibility Field **(A/m)**
H_O	True hardness **(GPa)**
H_{PSR}	Vickers hardness calculated by the proportional sample resistance model **(GPa)**
H_V	Vickers hardness **(GPa)**
I_C	Critical current **(A)**
I_D	Intensity of D peak from RAMAN **(a.u)**
I_G	Intensity of G peak from RAMAN **(a.u)**
J_C	Critical current density **(A/cm^2)**
K	Dimensionless shape factor
K_{IC}	Fracture toughness **($Pa/m^{\frac{1}{2}}$)**
λ	X-ray wavelength **(Å)**
M	Mass of sample **(g)**
N	Avogadro's number **(mol^{-1})**
P	Percentage porosity **(%)**
R	Resistance **(Ω)**
ρ	Bulk density **(g/cm^3)**
$ρ_x$	Xray density **(g/cm^3)**
T	Temperature **(K)**

$\mathbf{T_C}$	Critical transition temperature **(K)**
$\mathbf{\Delta T_C}$	Width of normal-superconducting state transition **(K)**
$\mathbf{T_{CMID}}$	Temperature at the middle of normal-superconducting transition state **(K)**
$\mathbf{T_{COFF}}$	Temperature at the end of normal-superconducting transition state **(K)**
$\mathbf{T_{CONSET}}$	Temperature at the start of normal-superconducting transition state **(K)**
$\mathbf{T_{curie}}$	Curie Temperature **(K)**
$\mathbf{T_N}$	Neel Temperature **(K)**
$\mathbf{V_1^{eq}}$	Volume from first iodometric titration **(ml)**
$\mathbf{V_2^{eq}}$	Volume from second iodometric titration **(ml)**
$\mathbf{V_{bulk}}$	Bulk volume of sample **(cm^3)**
$\mathbf{V_{cell}}$	Cell volume **($Å)^3$**
$\mathbf{W_{HK}}$	Critical applied load force from the elastic plastic deformation model **(N)**
Y	Yield strength **(GPa)**

Acronyms

AFM	Antiferromagnetic
BCS	Bardeen-Cooper-Schrieffer
CNTS	Carbon Nano Tubes
C-rGO	Chemically reduced Graphene Oxide
EDX	Electron Dispersive X-ray
EPD	Elastic Plastic Deformation
FC	Field Cooling
FM	Ferromagnetic
FIM	Ferrimagnetic
FTIR	Fourier Transform Infrared Spectroscopy
FWHM	Full Width Half Maximum
GO	Graphene Oxide
HK	Hays Kendall
HTS	High Temperature Superconductor
HTSs	High Temperature Superconductors**ISE** Indentation Size Effect
LRC	Linear Regression Coefficient
MAUD	Materials Analysis Using Diffraction
PM	Paramagnetic
PSR	Proportional Sample Resistance
RISE	Reverse Indentation Size Effect
rGO	Reduced Graphene Oxide
TEM	Transmission Electron Microscope
T-rGO	Thermally reduced Graphene Oxide
TS-GO	Thermally Stable Graphene Oxide
TU-GO	Thermally Unstable Graphene Oxide
XRD	X-ray Diffraction
YBCO	Yttrium Barium Copper Oxide ($Y_1Ba_2Cu_3O_{7-\delta}$)
ZFC	Zero Field Cooling

Contents

Declaration of Authorship ..... **i**

Abstract ..... **ii**

Acknowledgements **1**

List of Symbols and Units **2**

Acronyms **4**

List of Figures **8**

List of Tables **12**

1. Research Background **13**
1.1 Introduction 13
1.1.1 Overview of High Temperature Superconductivity 13
1.1.2 Improving Superconducting and Structural Properties of Bulk HTSs by Doping 14
1.1.2.1 Critical Transition Temperature (T_C) 14
1.1.2.2 Critical Current Density (J_C) 16
1.1.2.3 Critical Magnetic Field (H_C) 18
1.1.2.4 Mechanical Properties 19
1.2 Yttrium Barium Copper Oxide ($Y_1Ba_2Cu_3O_{7-\delta}$) 21
1.3 Graphene and Graphene Oxide 23
1.4 Manganese Oxides 25
1.5 Research Objectives and Questions 27
1.6 Contributions 28
1.6.1 Paper Contributions 28
1.6.1.1 Paper 1 28
1.6.1.2 Paper 2 (Chapter 2) 29
1.6.1.3 Paper 3 (Chapter 3) 29
1.6.1.4 Paper 4 (Chapter 4) 29
1.6.1.5 Paper 5 (Chapter 5) 30
1.6.2 Novel Contributions 31

References **32**

Chapter One Summary **36**

2 Peer-Reviewed Journal Article 1 ..... **37**
2.1 Abstract 38
2.2 Introduction 39
2.3 Experimental 40
2.4 Results and Discussion 42
2.5 Conclusion 47

References **48**

Chapter Two Summary **50**

3 Peer-Reviewed Conference Article 1 ..... **51**
3.1 Abstract 52
3.2 Introduction 53
3.3 Background 54
3.4 Experimental 56
3.5 Results and Discussion 59
3.6 Conclusion 63

References **64**

Chapter Three Summary **65**

4 Peer-Reviewed Journal Article 2 ..... **66**
4.1 Abstract 67
4.2 Introduction 68
4.3 Experimental 70
4.4 Results and Discussion 72
4.4.1 X-ray Diffraction Analysis 72
4.4.2 Microhardness and Modeling 74
4.4.3 Analysis According to Meyers Law 77
4.4.4 Analysis According to PSR Model 78
4.4.5 Analysis according to EPD Model 80
4.4.6 Analysis according to HK Model 81
4.5 Conclusion 85

References **86**

Chapter Four Summary **89**

5 Peer-Reviewed Journal Article 3 ..... **90**
5.1 Abstract 91
5.2 Introduction 92
5.3 Experimental 94
5.4 Results 96
5.4.1 Characterization of TS-GO and TU-GO 96
5.4.2 Xray Diffraction Analysis 98
5.4.3 Nano-Magnetic Impurity Analysis 100
5.4.4 Characterization of Manufactured Magnetic Nano Particles 101
5.4.5 Critical Transition Temperature Analysis of TS-GO and TU-GO doped YBCO 102
5.4.6 Critical Transition Temperature Analysis of Manganese Oxide doped YBCO 104
5.4.7 AC Susceptibility 105
5.4.8 Interpretation of TS-GO and TU-GO results 106
5.5 Conclusion 108

References **109**

6 Concluding Remarks 114

Appendix A – R vs. T Experimental Procedure 116

Appendix B – AC Susceptibility Experimental Procedure 119

List of Figures

Figure 1:1: Resistance versus temperature curve showing transition from normal state to superconducting state 14

Figure 1:2: Diagram showing interaction between magnetic field and supercurrent. 16

Figure 1:3: Difference in foot structure in an actual and ideal R vs. T curve 17

Figure 1:4: Ideal magnetization curve for high temperature superconductors 18

Figure 1:5: Behaviour of foot structure in an applied magnetic field 19

Figure 1:6: Indentation size effect and reverse indentation size effect response of a ceramic due to increasing load force. 19

Figure 1:7: a) Dopants filling voids and pores resulting in improved grain connectivity, b) Reduction in grain size resulting in increased number of grain boundaries thus trapping defects and c) Strain locking fields resulting in locking of defects. 20

Figure 1:8: Orthorhombic and tetragonal crystal structure of YBCO 21

Figure 1:9: a) Change in YBCO crystal structure due to change in non-stoichiometric oxygen content and b) Variation in T_C and Neel Temperature (T_N) with variation in non-stochimetric oxygen content of YBCO [18]. 22

Figure 1:10: Structure of copper oxide plane with a) showing a buckling angle less than 180˚ and b) showing a maximum buckling angle of 180˚. 23

Figure 1:11: Atomic structure of graphene and graphene oxide 24

Figure 1:12: Atomic structure of thermally unstable graphene oxide 25

Figure 1:13: Atomic structure of thermally stable graphene oxide 25

Figure 1:14: a) Atomic structure of MnO, b) Atomic structure of MnO_2, c) Atomic structure of Mn_2O_3 and d) Atomic structure of Mn_3O_4 26

Figure 2:1 : Vickers hardness indenter applying load on sample surface 40

Figure 2:2 : Diamond shaped indentation on sample surface with diagonals d_1 and d_2. 40

Figure 2:3 : TEM images of a) multilayered (2-3 layers) GO and b) a single sheet of rGO 42

Figure 2:4 : FTIR for graphite, GO and rGO 42

Figure 2:5 : RAMAN spectrum of GO and rGO 42

Figure 2:6 : ZFC R (T) curves for all GO doped samples 43

Figure 2:7 : ZFC R (T) curves for all rGO doped samples 43

Figure 2:8 : Applied Magnetic Flux density vs. ΔT_C for GO doped samples 44

Figure 2:9 : Applied Magnetic Flux density vs. ΔT_C for rGO doped samples 44

Figure 2:10 : Vickers hardness, H_v vs. applied load, F, for GO and rGO doped samples. 45

Figure 2:11 : Applied load, F vs. the diagonal of the impression squared, d^2, for GO and rGO doped samples. 45

Figure 3:1 : Change in YBCO phase due to variation in oxygen content. 54

Figure 3:2 : Orthorhombic and tetragonal structure of YBCO 54

Figure 3:3 : Curve demonstrating change in T_C as a function of oxygen content [3] 55

Figure 3:4 : a) Experimental setup inside glove bag and **b)** dissolving of sample inside glove bag with magnetic stirrer 56

Figure 3:5 : Testing pH level of the YBCO, KI and HCl solution in a nitrogen atmosphere using a pH meter. 56

Figure 3:6 : Colour changes which occur during titration 57

Figure 3:7 : a) dissolving of YBCO sample in HCl solution and **b)** solution after dissolving of YBCO sample 58

Figure 3:8 : Data from EDX showing elemental content of GO and rGO 59

Figure 3:9 : a) TEM image of GO and **b)** TEM image of rGO 59

Figure 3:10 : TEM image of YBCO grains 60

Figure 3:11 : rGO sheets with YBCO particles in doped samples 60

Figure 3:12 : Graphene sheets at YBCO grain boundary in doped samples 60

Figure 3:13 : R vs. T curves in ZFC conditions 61

Figure 3:14 : R vs. T curves in FC (5 mT) conditions 62

Figure 4:1: XRD spectrum of GO and rGO doped samples. 72

Figure 4:2: F vs. H_V for rGO doped samples 76

Figure 4:3: Ln F vs. Ln d for GO and rGO doped samples according to Meyers law. 77

Figure 4:4: F/d vs. d for GO and rGO doped samples according to PSR model 79

Figure 4:5: $F^{0.5}$ vs. dp for GO and rGO doped samples according to EPD model 80

Figure 4:6: F vs. d^2 for GO and rGO doped samples according to HK model. 81

Figure 4:7: Comparison between measured (H_V is measured at the plateau of F vs. H_V curve) and calculated H_V for rGO doped samples according to different models. 83

Figure 4:8: Comparison between measured (H_V is measured at the plateau of F vs. H_V curve) and calculated H_V for rGO doped samples according to different models. 83

Figure 5:1: FTIR spectrum of graphite, TS-GO and TU-GO. 96

Figure 5:2: RAMAN spectrum of graphite, TS-GO and TU-GO. 96

Figure 5:3: (a) TU-GO at 25 ◦C, (b) TU-GO at 200 ◦C, (c) TS-GO at 25 ◦C, (d) TS-GO 97

Figure 5:4: XRD pattern for control, TS-GO doped and TU-GO doped samples 98

Figure 5:5 : Williamson Hall plots of (a) control (b) 0.1 %wt. TS-GO (c) 0.5 %wt. TS-GO (d) 0.7 %wt. TS-GO (e) 0.1 %wt. TU-GO (f) 0.5 %wt. TU-GO (g) 0.7 %wt. TU-GO. 99

Figure 5:6 : EDX spectra of nano magnetic impurities. 100

Figure 5:7: XRD spectra of MnO_2 and Mn_3O_4. 101

Figure 5:8: FTIR spectra of MnO_2 and Mn_3O_4. 101

Figure 5:9: ρ vs T curves for TU-GO doped samples. 102

Figure 5:10: ρ vs T curves for TS-GO doped samples. 103

Figure 5:11: ρ vs T curves for MnO_2 andMn_3O_4 doped samples 104

Figure 5:12: AC susceptibility versus temperature curves. 105

Figure 5:13: Relationship between T_C and the area of CuO_2 planes. 107

Figure A:1 : Experimental stage attached to cold head 116

Figure A:2 : Helmholtz coils 116

Figure A:3 : Graph showing the relationship between the amount of current passing through the coil and magnetic field generated by the coil. 117

Figure A:4 : Experimental stage in ZFC conditions 117

Figure A:5 : Experimental stage in FC conditions 118

Figure B:1: Diagram of AC susceptibility experiment. 119

Figure B:2: Experimental stage for AC susceptibility experiment. 120

Figure B:3: Dimensions of primary coil (mm) 121

Figure B:4: Dimensions of sample and reference coil (mm) 121

Figure B:5: Block diagram of lock-in amplifier 122

Figure B:6: a) Primary coil b) Reference and sample coil c) Reference and sample coils inside primary coil 122

Figure B:7: Experimental stage for AC susceptibility experiment 123

List of Tables

Table 2:1 : Analysis of ZFC curves 44

Table 2:2 : Hardness test results for GO and rGO doped samples 45

Table 3:1 : Analysis of ZFC curves 61

Table 4:1: Lattice strain, oxygen content, crystallite size, lattice parameters and orthorhombicity of GO and rGO samples. 72

Table 4:2: Average oxygen content, Cu(1) and Cu(2) atomic site occupancies of control, GO and rGO samples 73

Table 4:3 : Calculated load dependent H_V, E, Y and K_{IC} for control, GO and rGO doped samples 75

Table 4:4: X-ray density, bulk density and percentage porosity 77

Table 4:5: Best fit experimental data according to meyer's law 78

Table 4:6: Best fit parameters for GO and rGO doped samples according to the PSR model. 79

Table 4:7: Best fit parameters for GO and rGO doped samples according to the EPD model. 80

Table 4:8: Best fit parameters for GO and rGO doped samples according to HK model 82

Table 4:9: Load independent mechanical parameters according to HK model. 82

Table 5:1: Average of several EDX points of TU-GO and TS-GO. 98

Table 5:2: Oxygen content, lattice strain, T_C and lattice parameters of control, TS-GO and TU-GO doped samples. 99

Table 5:3: T_{CONSET} from ρ vs. T curve and χ' vs. T curves 105

Chapter 1

Research Background

1.1 Introduction

1.1.1 Overview of High Temperature Superconductivity

The first high temperature superconductor (HTS) discovered was La-Ba-Cu-O in 1986 with a T_C = 35 K [1]. This discovery was of great importance as at this period in time Bardeen-Cooper-Schrieffer (BCS) theory suggested that it is impossible to have a T_C above 30 K [2], thus began the evolution of high temperature superconductors (HTSs).

Thereafter many ideas were tested in order to discover new HTSs with higher critical transitional temperatures (T_Cs) or improve the T_C's of existing material. One of the successful methods carried out by Chu was the application of hydrostatic pressure which increased T_C above 40 K for the La-Ba-Cu-O system [3]. This gave rise to the idea of conducting controlled atomic substitutions on the La-Ba-Cu-O system in order to increase the pressure on the lattice internally instead of application of external pressure.

These controlled atomic substitutions resulted in the discovery of superconductivity in Y-Ba-Cu-O (YBCO) system at a T_C = 93 K in 1987 [4]. This was of significance as it was the first HTS with a T_C above the boiling point of liquid nitrogen (77 K) [5] which is a much cheaper cryogen than liquid helium. This allowed for a wider range of applications as the cost of cryogenic systems decreased. After the discovery of YBCO, the Bi-Sr-Ca-Cu-O system (BSCCO) was discovered in 1988 with a $T_C \approx 110$ K [6] [7]. Many other HTS systems were discovered with the highest T_C in that of the Hg-Ba-Ca-Cu-O system with a T_C of 153 K with an applied external pressure of 150 kbar [8].

The major downfall of bulk HTSs is the network of weak-links that occurs at grain boundaries. These weak-links in bulk material severely reduce the critical current density (J_C) [5] [9] [10], broaden the normal-superconducting phase transition [11], and diminish the mechanical structural properties of the bulk material [12].

The idea of atomic substitutions to achieve new HTS systems gave rise to the idea of doping bulk HTSs in order to improve their properties such as J_C, T_C, grain connectivity and mechanical properties. Another approach to increase grain connectivity led to specialized expensive techniques to texture HTS material especially for electrical conductors [13].

1.1.2 Improving Superconducting and Structural Properties of Bulk HTSs by Doping

This section discusses how doping improves the superconducting and mechanical properties of bulk HTSs.

1.1.2.1 Critical Transition Temperature (T_C)

T_C is defined as the temperature at which a superconductor transitions from the normal state to the superconducting state [14]. This property is of vital importance as the expense of cryogenic cooling systems limits the range of applications in which superconductors can be used. There is a direct link between increasing the T_C of a material and enhancing its J_C at operational temperatures [15]. The R vs. T curve in Figure 1:1 shows three different definitions of T_C that exists in literature.

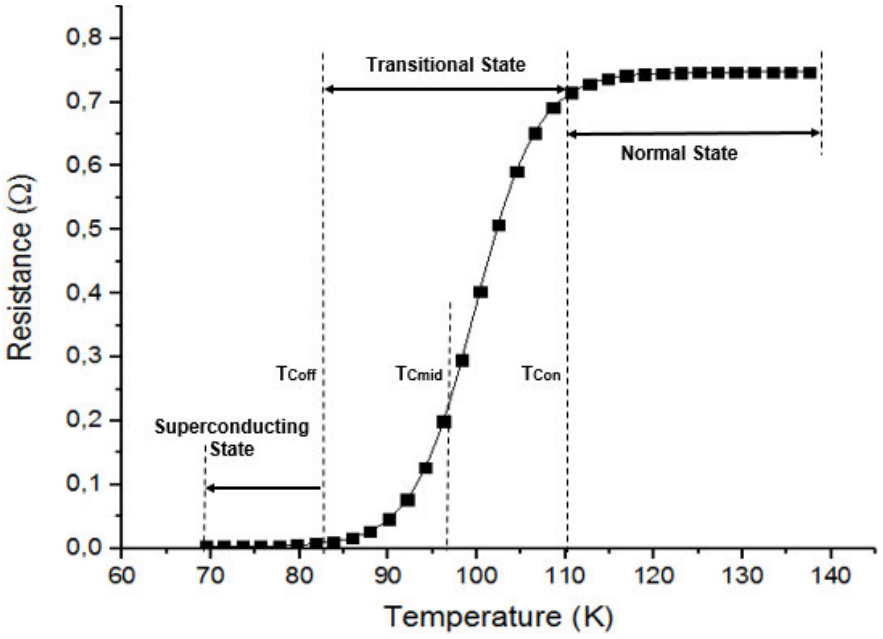

Figure 1:1: Resistance versus temperature curve showing transition from normal state to superconducting state

T_{Con} is the temperature at which the transition from the normal state to the superconducting state begins [16]. T_{Coff} is the temperature at which the superconducting state is reached [16]. T_{Cmid} is defined as the midpoint between the T_{Con} and T_{Coff} [17].

In this research there are two important dopants that have been identified that effects T_C, oxygen and manganese. It is well established that doping YBCO with oxygen increases T_C up to 93 K [4] [18], this is due to an increase in non-stoichiometric oxygen content which is discussed in detail in Section 1.2.

Doping YBCO with Manganese (Mn) has had some controversy, as some studies report an increase in T_C [19] [20] [21] and some report a decrease in T_C [22] [23]. Research has shown an improvement in T_{Coff} up to 94 K and T_{Con} up to 97 K [19] [20] [21].

Reasons offered for this T_C increase are, (i) Mn aiding in the formation of YBCO Y247 phase which is known to have a T_C of 95 K [20] [21], (ii) Mn helping with the achieving of an optimum sintering temperature range between 940˚C to 970˚C [20], and (iii) Mn particles helping the transfer of oxygen into the crystal structure and/or act as a carrier reservoir [19].

The reasoning for Mn doping suppressing the T_C is due to the formation of semiconducting phases [23], Mn ions occupying the Cu (1) atomic site thus reducing the amount of oxygen in the sample and the Mn ions occupying the Cu (2) atomic site in the CuO_2 planes [22]. These Cu (1) and Cu (2) atomic sites can be seen in Figure 1:8 in Section 1.2.

Doping of YBCO with Mn_3O_4 magnetic nano-particle was seen to increase T_C to 112 K [24] [25] [26] at very low doping concentrations in the range of 0 - 0.2 % wt. This increase in T_C above 93 K was attributed to the Mn_3O_4 particles causing the formation of YBCO with high orthorhombicity and superior superconducting properties [24] [25] and these particles assisting in the transfer of oxygen into the YBCO crystal lattice [19]. However, no conclusive reasoning has been offered to date. In published paper 5 (chapter 5), we see an increase in CuO_2 planar area which may be due to an increasing in the CuO_2 plane's bucking angle.

Doping YBCO with GO has been seen to increase T_C [27] [28]. This has been attributed to the oxygen from GO diffusing into the crystal structure thus increasing the non-stoichiometric oxygen content of YBCO [27] [28]. Some studies of GO doping show an improvement in T_C above 93 K, which is the maximum T_C [27] [28] which can be achievable due to an increase in the oxygen content as seen in Section 1.2. Thus, there is another possible mechanism allowing for the increase in T_C above 93 K.

GO doping has also been seen to result in a marginal decrease in T_C [29]. This has been attributed to the decomposition of GO therefore increasing the amount of carbon in the sample which weakens grain connectivity [29].

In this research YBCO is doped with GO and rGO. T_C in both GO and rGO samples have been observed to increase due to diffusion of oxygen into the crystal structure resulting in an increase in the non-stoichiometric oxygen content. The increase in δ was determined by iodometric titration and x-ray diffraction. This mechanism is explained in Section 1.2. T_Cs above 93 K were observed in certain GO doped samples. This was explained as a combined effect of the increase in non-stoichiometric oxygen content and the formation of Mn_3O_4 impurities in the samples, which is a result of the GO production process.

Manganese impurities which are created in GO and rGO materials as a result of the chemical production process has been seen to affect the applications in which the GO or rGO is used

[30]. This was observed when rGO electrodes were used in a reduction reaction application but the electrochemical properties of the rGO was modified due to manganese impurities thus affecting the performance of the rGO electrode in the reaction [30].

1.1.2.2 Critical Current Density (J_C)

The critical current density, J_C, is defined as the maximum current per specific area that a superconductor can carry in the superconducting state and a current density greater than this, will result in the superconductor transitioning back into the normal state [14].

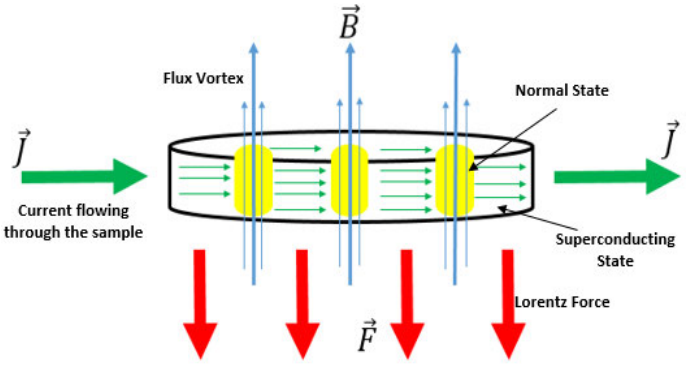

Figure 1:2: Diagram showing interaction between magnetic field and supercurrent.

Doping of bulk HTSs has led to an increase in J_C due to dopants acting as flux pinning sites [27] [31] [32]. Self-magnetic fields, induced by supercurrent, interact with the supercurrent and experiences a Lorentz force [5] [9] [14] [33] which is described by the following equation,

$$\vec{F} = \vec{J} \times \vec{B}, \qquad 1.1$$

were $\vec{F}$ is Lorentz force, $\vec{J}$ is current density and $\vec{B}$ is magnetic flux density. This force, shown in Figure 1:2, results in the motion of the flux vortices, which in turn generates an electric field [5]. This electric field creates the motion of normal electrons which creates a resistance [5]. Therefore if these flux vortices (magnetic field) are pinned it will allow for larger J_C because it will take a larger Lorentz force to cause the motion of the flux vortices. These flux pinning sites are one of the reasons that HTSs are able to carry large currents in an applied magnetic field [14].

Polycrystalline bulk HTS material is made up of a large amount of grains with various different shapes and sizes. This results in both structural and compositional disorder at grain boundaries [10]. Due to HTSs having a short coherence length these structural and compositional disorders act as weak-links [9]. Misaligned grains greater than 10˚result in grain-to-grain reduction of J_C by an order of magnitude [34]. The random arrangement of grains results in the anisotropy of J_C in bulk HTS's [35]. Compositional disorders consist of changes in oxygen stoichiometry and impurities at grain boundaries [10] [34]. This change in oxygen stoichiometry and impurities

will vary the T_C at grain boundaries and create various non-superconducting phases to occur at grain boundaries [10]. This results in a reduced intergranular J_C and a decrease in transport current within the bulk material. The intragranular J_C of HTS's varies from grain to grain due to microcracks on grains and the different oxygenation level of each grain [36] [37]. Thus, resulting in the overall J_C of the material deteriorating. Due to the variation of the intragranular critical currents.

These weak-links manifests themselves in the resistance versus temperature (R vs. T) curve creating a 'foot' structure, which is sensitive to magnetic field and shown in Figure 1:3. In the ideal curve it can be seen that at a specific temperature T_C, the entire superconductor goes into the superconducting state. Compare to the actual R vs. T curve which can be seen to curve out to the left due to the resistance decreasing with a decrease in temperature. Thus showing that parts of the bulk HTS goes into the superconducting state at different temperatures and not the entire sample at one temperature. This is due to varying T_C at grain-boundaries, acting as weak-links [10] [11].

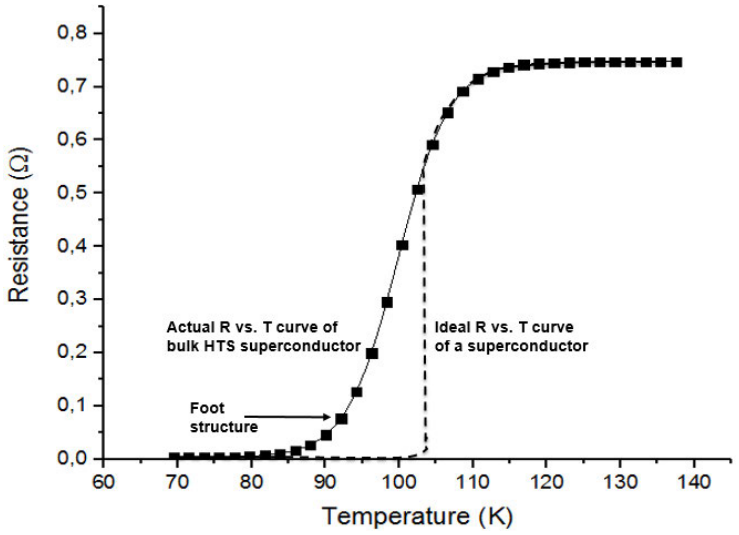

Figure 1:3: Difference in foot structure in an actual and ideal R vs. T curve

Past research has shown that doping YBCO with various magnetic, non-magnetic and ferromagnetic materials results in artificial pinning centers. Doping YBCO with silver (Ag) has seen Ag acting as a 'flux' cleaning grain boundary of impurities, increase the flux pinning force and the number of flux pinning sites at grain boundaries and inside grains. This improved both intergranular and intragranular J_C. Therefore, resulting in an overall improvement in the J_C of the material. [31] [38].

Doping YBCO with carbon nanotubes (CNTs) improves J_C due to the carbon nanoparticles acting as flux pinning centers, improving grain boundary connectivity and increasing pinning energy [32] [39]. CNTs is seen to improve J_C in the low doping concentrations. Further increase

in doping concentrations results in the reduction in J_C due to the samples becoming carbon contaminated and porous because of the release of CO_2 gas from the formation $BaCO_3$ impurities during sintering [32].

Doping YBCO with GO has been seen to increase J_C [27] [40]. This was attributed to improvement in grain boundary connectivity thus reducing the weak-link effect and increase in flux pinning sites due to graphene nano-particles [27] [28] [40]. This improvement in grain boundary connectivity is a result of GO forming rGO at grain boundaries. rGO has a high electrical conductivity therefore improving grain connectivity [27]. In this research a significant reduction has been observed in the weak-link effect in both GO and rGO doped samples.

1.1.2.3 Critical Magnetic Field (H_C)

The critical magnetic field (H_C) of a superconductor is defined as the maximum applied magnetic field which the superconductor can withstand in the superconducting state before transitioning to the normal state [14]. HTSs, are Type-2 superconductors hence they have two critical fields H_{C1} and H_{C2} which can be seen in Figure 1:4.

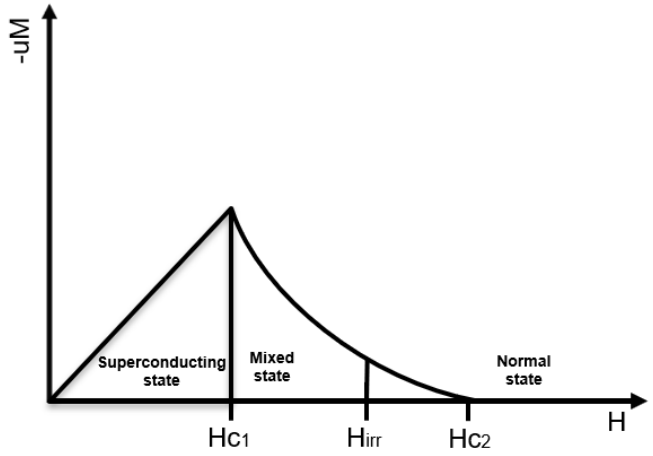

Figure 1:4: Ideal magnetization curve for high temperature superconductors

For applied magnetic fields below H_{C1} the superconductor will remain in a perfect diamagnetic superconducting state [14]. When the applied field, H, is greater than H_{C1} but less than H_{C2} the superconductor transitions into the mixed state [14]. In this state there is some magnetic field penetration of the superconductor in the form of flux vortices, and the superconductor consists of both superconducting and normal regions. In the range between H_{C1} and H_{C2} there is another important magnetic field measurement the irreversibility field (H_{irr}). For applied magnetic fields above H_{C1} and below H_{irr} the flux vortices are pinned and for applied magnetic fields above H_{irr} but below H_{C2} the vortices are not pinned [41]. The movement of these unpinned vortices results in the superconductor not being able to carry current without losses. Thus high field and high current applications are limited by H_{irr} [42]. If the applied magnetic field goes above H_{C2} the

superconductor transitions to the normal state [14].

Due to weak-links being a result of compositional disorders discussed in the previous section, there is a variation of the H_{C1} and H_{C2} of the grain boundaries [43]. This variation in the H_C at grain boundaries can be seen by the increase in the foot structure of the R vs. T curve in field cooling (FC) conditions. That is the grain boundaries result in the superconductor being sensitive to applied field below H_{C1} of the bulk, as shown in Figure 1:5.

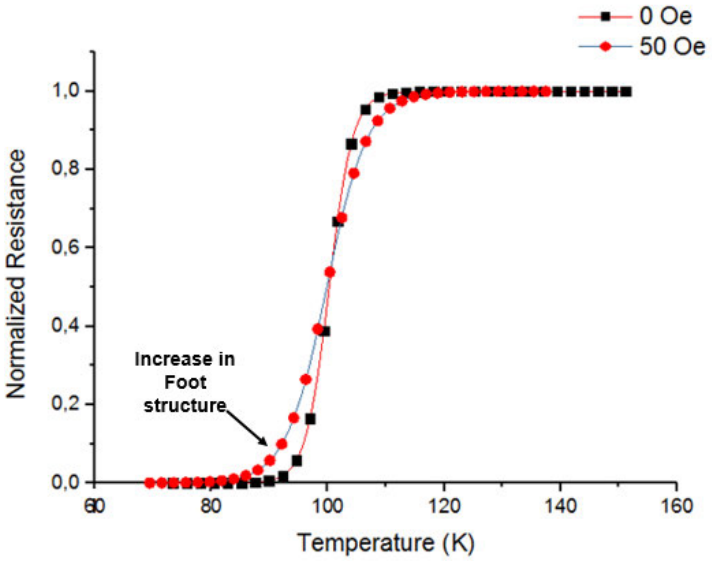

Figure 1:5: Behaviour of foot structure in an applied magnetic field

1.1.2.4 Mechanical Properties

HTSs have various applications such as fault current limiters, ac/dc transmission lines, and machines [5]. One of the major drawbacks for practical applications is mechanical brittleness. This is due to the intrinsic properties of ceramics and the unavoidable pores present in sintered bulk samples [44] [45].

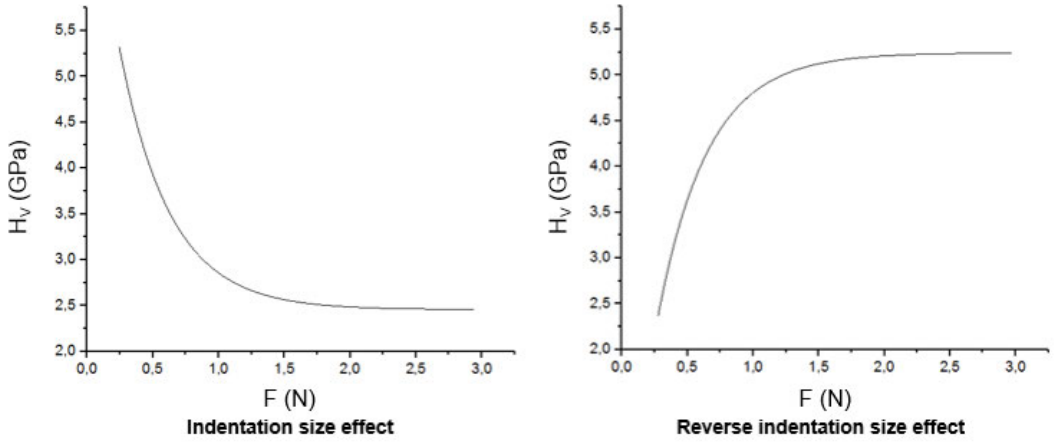

Figure 1:6: Indentation size effect and reverse indentation size effect response of a ceramic due to increasing load force.

Hardness testing of ceramics result in one of two responses. The indentation size effect (ISE) and reverse indentation size effect (RISE) seen in Figure 1:6. ISE response occurs when the hardness of the material decreases with an increase in applied load force. This ISE behaviour can be explained by the elastic-plastic deformation effect [12]. RISE behaviour occurs when the hardness of the material increases with an increase in applied load force. The RISE behaviour is due to the specimen having impurity phases, irregular orientation of grains, and porosity [12].

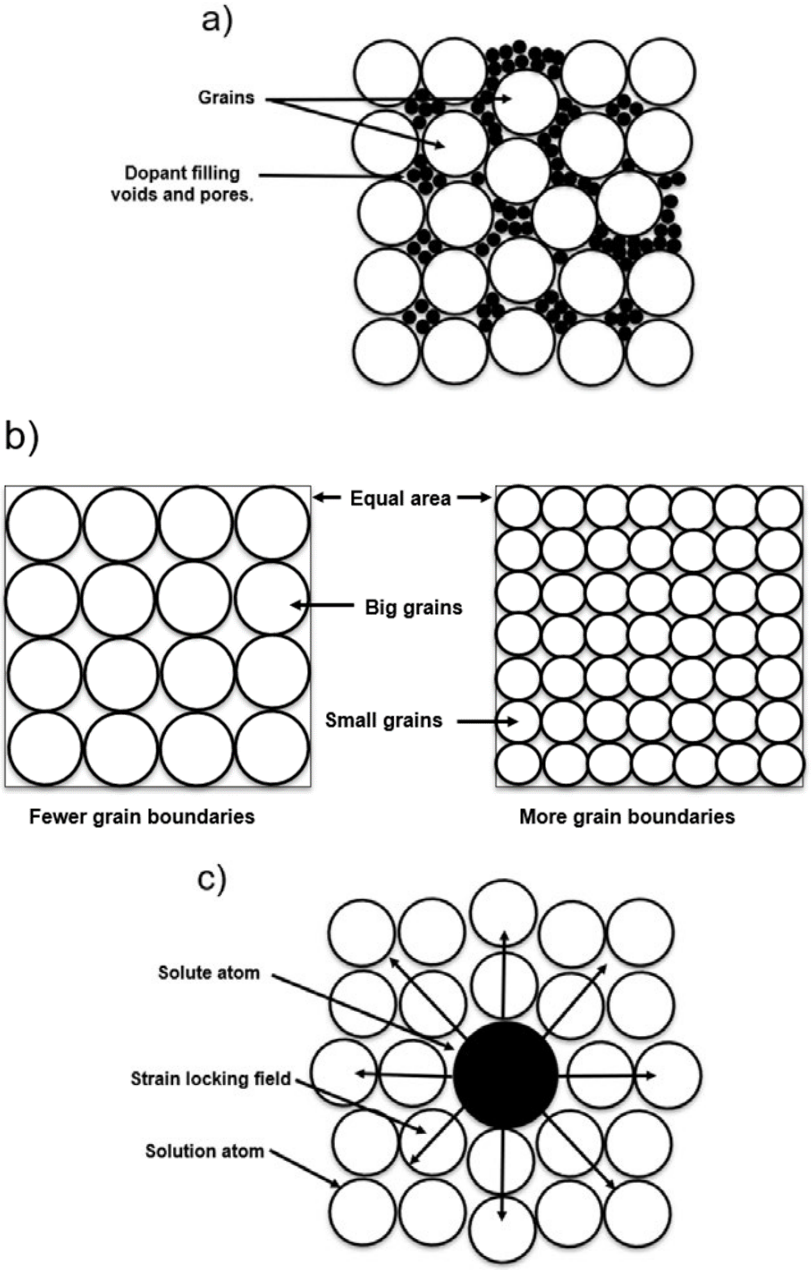

Figure 1:7: a) Dopants filling voids and pores resulting in improved grain connectivity, b) Reduction in grain size resulting in increased number of grain boundaries thus trapping defects and c) Strain locking fields resulting in locking of defects.

Some of the mechanisms which have been responsible for increasing hardness in bulk HTSs are the improvement of weak links at grain boundaries, reduction of grain size and solute solution strengthening [46] [47] [48] [49]. Improvement in grain connectivity is a result of dopants filling the voids and pores at grain boundaries thus reducing porosity of the material [47] [48]. Reduction in grain size increases the number of grain boundaries, therefore more defects will be locked at grain boundaries [49]. Solute solution strengthening is due to dopant particles causing strain fields in the precursor material thus resulting in locking of defects due to these strain fields [46]. These mechanisms can be seen in Figure 1:7.

Doping YBCO with zinc oxide and lithium is seen to increase micro-hardness due to the mechanism called solute solution strengthening [50] [51]. Doping YBCO with lutetium and gold is seen to reduce the micro-hardness due to the enhancement of weak-links at grain boundaries and increase in impurity phases [44] [12]. GO and rGO doping of YBCO has been shown to improve elastic moduli, longitudinal modulus, young's modulus and micro-hardness. These enhancements were due to reduction in porosity and improved grain connectivity [47] [48].

1.2 Yttrium Barium Copper Oxide ($Y_1Ba_2Cu_3O_{7-\delta}$)

YBCO has a defective perovskite structure [5]. It consists of two copper oxide planes which are separated by a Y-layer and thereafter Ba-O and Cu-O layers on either side of the copper oxide planes. The difference between the orthorhombic and tetragonal crystal structure of YBCO seen in Figure 1:8, which results from oxygen vacancies in the one-dimensional Cu-O chains. In the orthorhombic structure oxygen vacancies are found between copper atoms in the Cu-O chains and in the tetragonal structure these oxygen vacancies are full this can be seen in Figure 1:8 [14] [18].

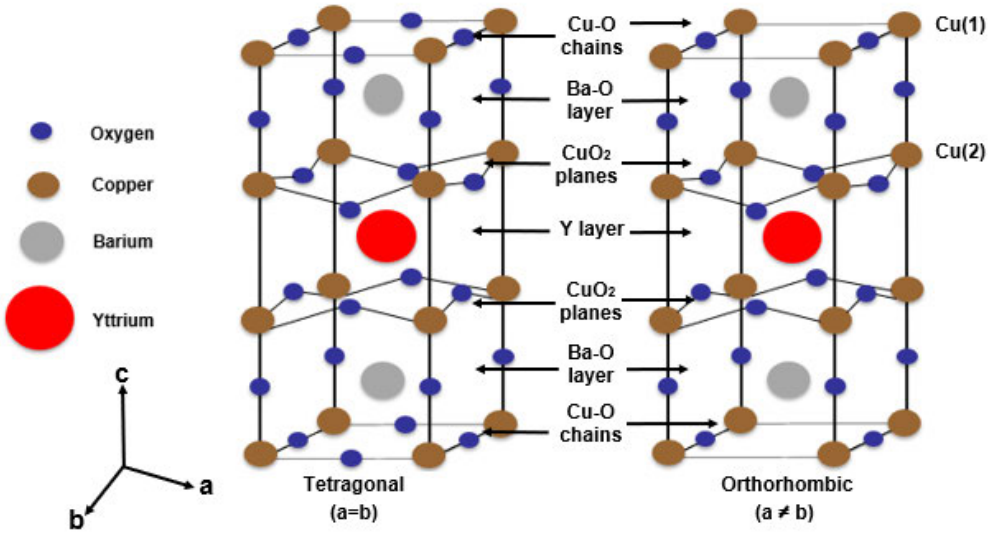

Figure 1:8: Orthorhombic and tetragonal crystal structure of YBCO

This is of vital importance as the tetragonal phase of YBCO has no superconducting properties and is insulating [14] [18]. From this it can be seen that oxygen plays a significant role in the superconducting phase of YBCO. YBCO's chemical formulae is $Y_1Ba_2Cu_3O_{7-\delta}$.

If δ is approximately between $0 < \delta < 0.6$, YBCO will be in the orthorhombic phase and therefore have superconducting properties [14] [18], as shown in Figure 1:9 a). The orthorhombicity of the YBCO material can be calculated to determine the superconducting phase purity of the material. This value varies between 0 and 1. The closer the value is to one the higher the concentration of the orthorhombic phase is in the bulk material [52]. Varying δ in this range will also result in the variation of T_C for YBCO which can be seen in Figure 1:9 b). Increasing oxygen content increases the amount of holes in the CuO_2 planes resulting in an increase in T_C [18]. A maximum T_C of 93 K can be achieved at an optimum δ, [18] shown in Figure 1:9 b). In this research the control sample used was under oxygenated for both GO and rGO dopings. This was intentionally done to observe if doping with GO and rGO increases the oxygen content of YBCO thus improving T_C.

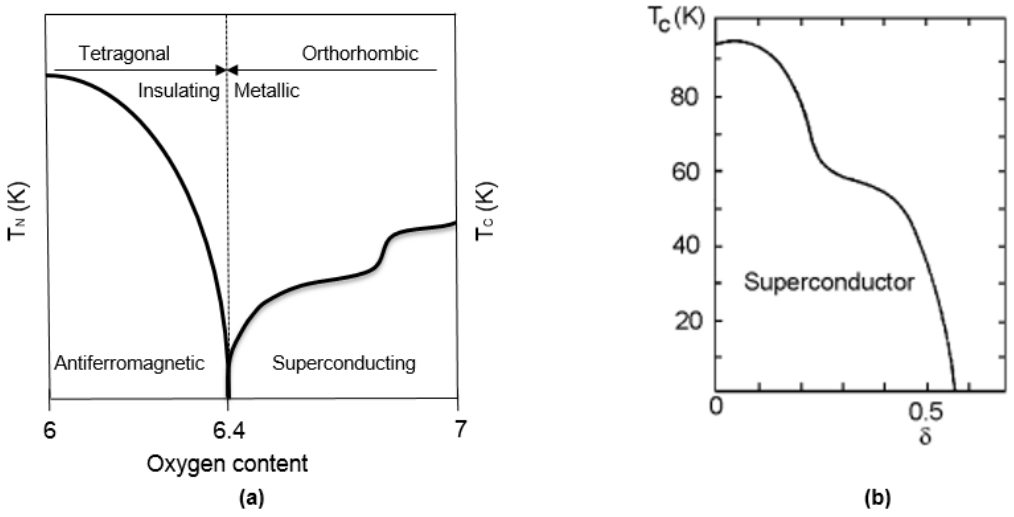

Figure 1:9: a) Change in YBCO crystal structure due to change in non-stoichiometric oxygen content and b) Variation in T_C and Neel Temperature (T_N) with variation in non-stochimetric oxygen content of YBCO [18].

As the oxygen content decreases and δ increases to the range of $0.6 < \delta < 1$ the oxygen atoms occupy the vacant sites between the Cu-O chains thus resulting in a disordered tetragonal structure. The change from orthorhombic to tetragonal structure results in the appearance of antiferromagnetic properties and the disappearance of the superconducting phase seen in Figure 1:9 a) [18]. In the tetragonal state as the oxygen content increases in the range of 6 < oxygen content < 6.4 the Neel temperature (T_N) decreases. T_N of a material is defined as the temperature above which material behaves like a paramagnetic material and below which the material acts as an antiferromagnetic material [53].

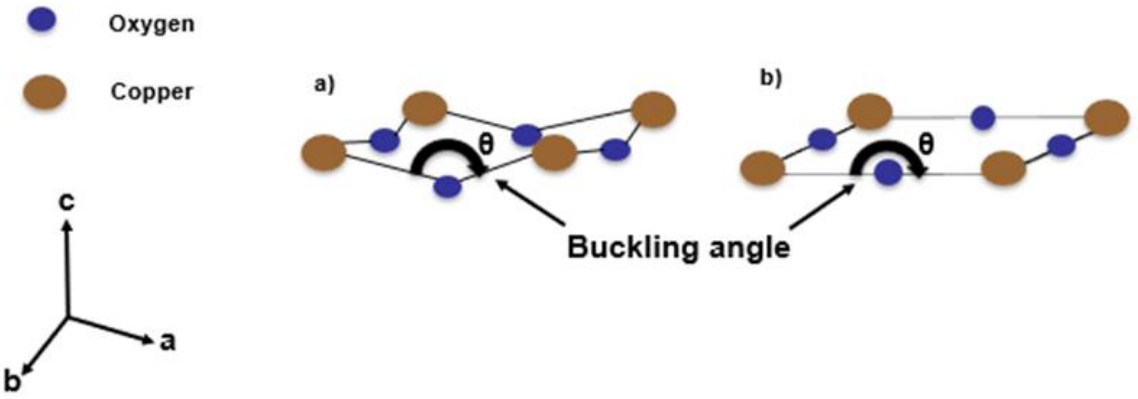

Figure 1:10: Structure of copper oxide plane with a) showing a buckling angle less than 180˚ and b) showing a maximum buckling angle of 180˚.

The CuO_2 planes are the part of the crystal structure in which electrons form Cooper pairs thus allowing for superconductivity to occur [54]. Past research has showed that changing the structure of CuO_2 will either enhance or diminish T_C [54] [55]. The structure of CuO_2 planes can be adjusted by changing the degree by which the planes buckle. This is measured by the buckling angle of the CuO_2 planes showed in Figure 1:10. The buckling angle has a maximum of 180˚ which is almost no buckling [56]. Increasing the buckling angle will allow for flatter planes with a more 2D structure and a larger area [56]. CuO_2 planes with a more 2D structure is known to enhance the T_C of the YBCO family [54]. These changes to the buckling angle of the copper oxide planes can be achieved through application of external pressure [57] and doping [58].

1.3 Graphene and Graphene Oxide

The graphene structure is shown in Figure 1:11 and is a two dimensional single atomic layer thick carbon material [59]. It is hydrophobic and has desirable electrical, mechanical, thermal, and optical properties [59] [60]. GO is also a two-dimensional carbon material which is single atomic layer thick laced with oxygen groups seen in Figure 1:11 [28] [61]. GO is an insulator and is hydrophilic [59] [60]. This insulating property is due to the disruption of the sp^2 bonding network which can be seen in Figure 1:11 [60].

The first single layer graphene sheet was isolated in 2004 using the scotch tape method [62]. This method could not produce a significant quantity of material to be used in applications therefore various others methods for the production of graphene were developed. The reduction of chemically oxidized GO is the most common method of producing graphene to date due to its scalability to produce large quantities [59]. From the various chemical methods Hummers methods is the most commonly used to oxidize graphite to produce GO [60] [63].

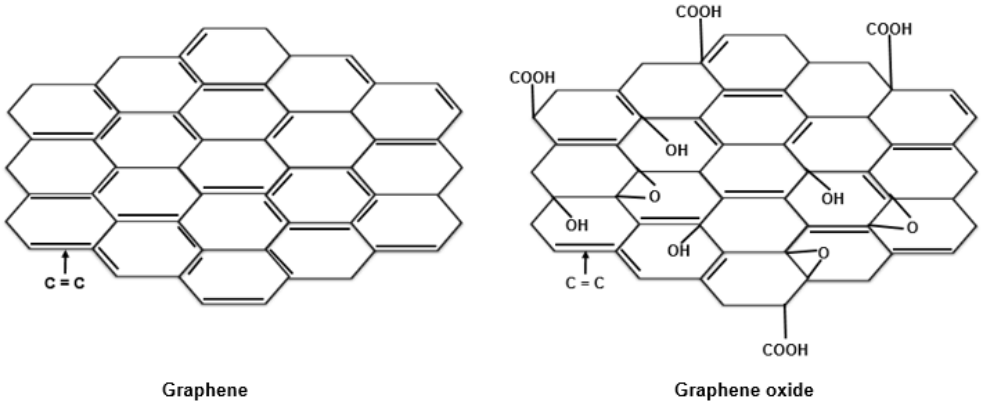

Figure 1:11: Atomic structure of graphene and graphene oxide

Variations of the Hummer method have been developed which are called improved Hummers method and Hummer method with additional potassium permanganate ($KMnO_4$) [64]. Once GO is produced rGO can be formed by many reduction methods the most common being thermal reduction by heating of the GO resulting in the removal of oxygen functional groups and various chemical reduction methods [59]. This thermal reduction of GO can result in an explosive reaction causing the layers of multilayer GO to be pushed apart forming single and bi-layer graphene [65]. The pushing apart of layer is due to violent release of oxidative debris from between GO layers during heating [65]. The explosiveness of this reaction is dependent on the amount of oxide debris in the material [65]. If there is a large amount of oxidative debris between GO layers there will be an explosive reaction due to large amount of gas released. This type of GO is also referred to thermally unstable graphene oxide (TU-GO) which can be seen in Figure 1:12 [65]. If there is a small amount oxidative debris there will be no pushing apart of layers the gas will just be released. This type of GO is referred to as thermally stable graphene oxide (TS-GO) which can be seen in Figure 1:13 [65].

Thermally reducing GO always results in a decrease in mass of the material [66] but the volume of the material may increase or decrease dependent on the amount of oxidative debris. GO with high amount of oxidative debris results in an increase in volume and the opposite applies for GO with a small amount of oxidative debris [65]. The amount of oxidative debris in the GO material can be controlled by the number of washing cycles the material undergoes. More washing cycles results in a decreasing number of oxidative debris[[67].

In this research GO was produced using the Hummer method with additional potassium permanganate and reduced via the chemical method using sodium borohydride ($NaBH_4$) with calcium chloride ($CaCl_2$) as a catalyst. TU-GO was produced by the GO material undergoing one washing cycle and TS-GO was produced by GO undergoing four washing cycles.

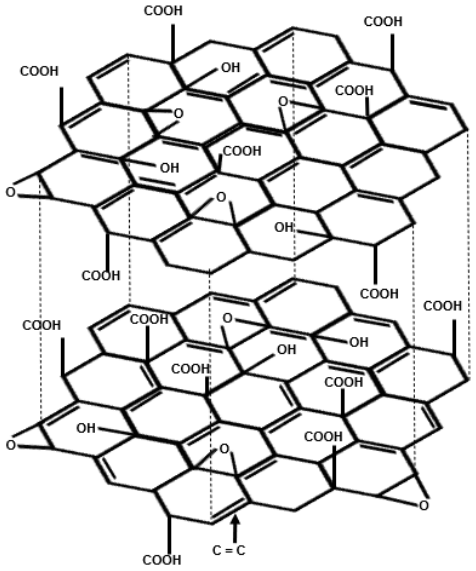

Figure 1:12: Atomic structure of thermally unstable graphene oxide

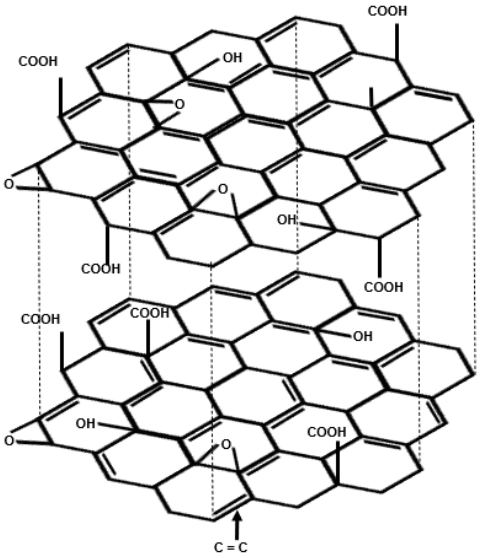

Figure 1:13: Atomic structure of thermally stable graphene oxide

1.4 Manganese Oxides

Manganese is a transitional metal which exist in various oxidation states thus resulting in the formation of manganese oxides [68]. In manganese oxides cations exist in 3 oxidation states Mn^{2+}, Mn^{3+} and Mn^{4+} [69]. These cations exist in the following oxides manganosite (MnO), pyrolusite (MnO_2), bixbyite (Mn_2O_3) and hausmannite (Mn_3O_4) [69]. In Figure 1:14 the cations and the crystal structure of these manganese oxides can be seen.

MnO and Mn_2O_3 have a cubic structure in the la-3 and Fm-3m space group respectively which can be seen in Figure 1:14 a) and c) [68]. In Figure 1:14 b) and d) tetragonal crystal structure of MnO_2 and Mn_3O_4 is shown. MnO_2 crystal structure is in the l4/m space group while Mn_3O_4 crystal structure is in the $l4_1$/amd space group [68].

The magnetic properties of manganese oxides have been studied for decades and used in many applications such as high-density magnetic storage media, supercapacitors, electrical energy storage and electronics [68]. The magnetic ordering of manganese oxides is dependent on the size, shape and internal strain of its particles. Due to these particle properties affecting the materials magnetic ordering, this in turn results in the variation of magnetic properties such as Curie temperature (T_{curie}), Neel temperature (T_N), anisotropic energy and spontaneous magnetization [68]. T_{curie} of a material is defined as temperature above which a magnetic material behaves like a paramagnetic material and below which a magnetic material behaves

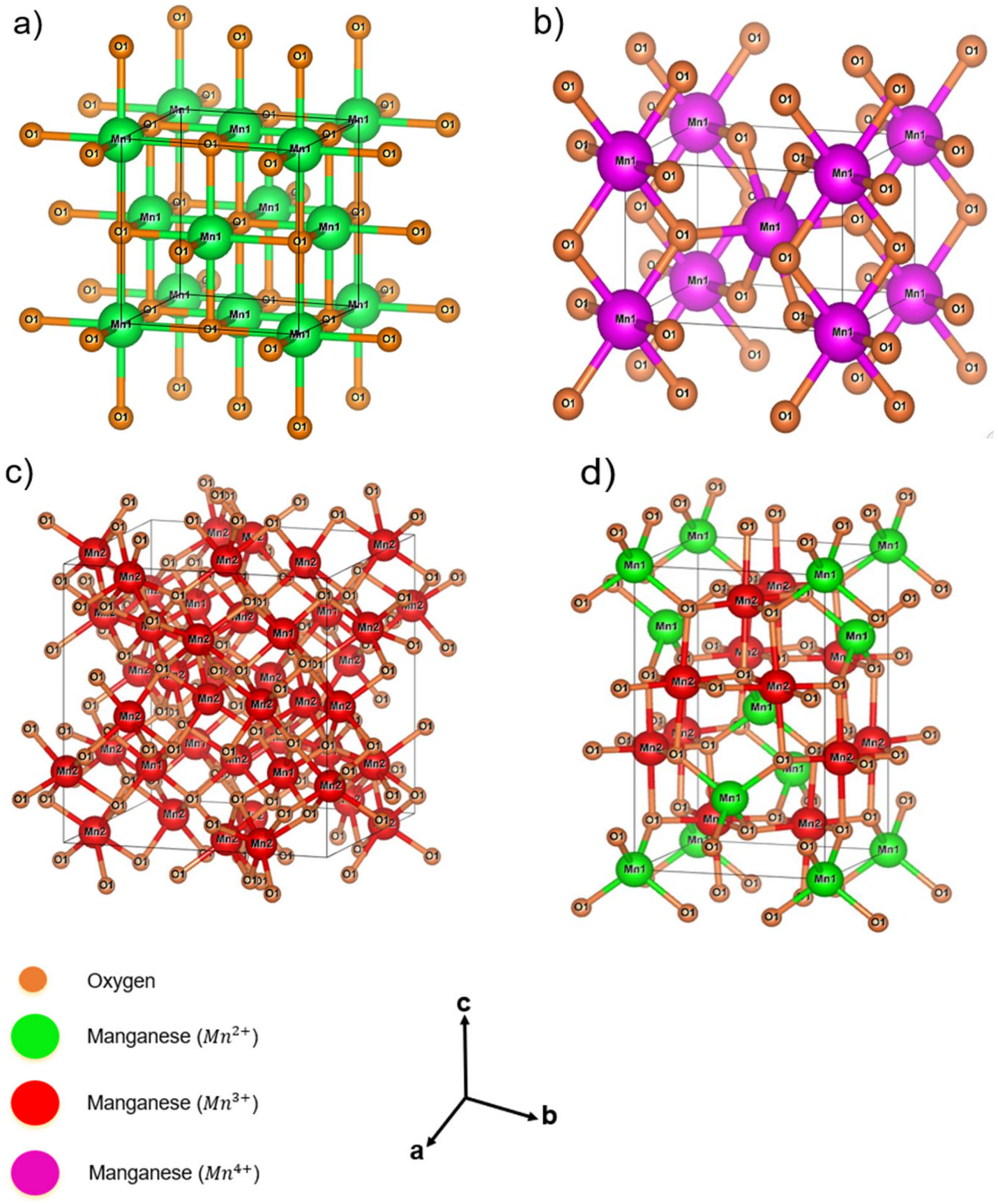

Figure 1:14: a) Atomic structure of MnO, b) Atomic structure of MnO_2, c) Atomic structure of Mn_2O_3 and d) Atomic structure of Mn_3O_4

like a ferromagnetic or ferrimagnetic material [53]. T_N of a material is defined as the temperature above which material behaves like a paramagnetic material and below which the material acts as an antiferromagnetic material [53]. Thus, varying temperature will affect the magnetic ordering of manganese oxides [68].

In ferromagnetic (FM) materials the atomic moments are aligned in the same direction, therefore the material has a net magnetic moment and in ferrimagnetic (FIM) materials the atomic moments are aligned in the opposite direction, but some atomic moments are greater than others which results in the material having a small magnetic moment. In antiferromagnetic (AFM) material the atomic moments are equal and orientated opposite to each other therefore resulting in the material having a zero magnetic moment. In paramagnetic (PM) materials the atomic moments are randomly orientated which results in the material having a magnetic moment [70].

MnO nanoparticles show FM behaviour while MnO bulk shows AFM behaviour with a PM to AFM transition at approximately T_N ~ 118 K [70]. The FM behaviour in MnO nano clusters is due to uncompensated surface spins [68]. β-MnO_2 which is used in this study shows a PM to AFM transition at T_N ~ 92 K [71] . Mn_2O_3 shows a PM to AFM transition at T_N ~ 90 K and an AFM to FM at T_{curie} ~43 K. Mn_3O_4 showed a PM to FIM transition at T_{curie}~43 K. This transition temperature varied with the size of the Mn_3O_4 nanoparticles. The smaller the particles the lower the transition temperature [68].

The following methods can be used to produce manganese oxides: thermal decomposition, exfoliation, permanganates reduction, adsorption oxidation and hydro/solvothermal [72]. In this research the method of thermal decomposition is used. In this process the precursor material (MnO_2) is oxidized during sintering [73]. In this research MnO_2 was sintered at 1000º for 1 hour in air to produce Mn_3O_4

1.5 Research Objectives and Questions

Research by others regarding the doping of YBCO with GO and rGO has seen a remarkable improvement in superconducting properties. Increase in T_C, improved grain connectivity due to a decrease in the weak-link effect, increased J_C and enhanced mechanical properties[26] [39] [40] [47] [48].

The increase in T_C was greater for GO doped samples than rGO doped samples. This is normally attributed to GO having more oxygen than rGO thus resulting in GO doped samples having a greater oxygen content hence higher T_Cs. In certain GO doped YBCO studies an increase in T_C above 93 K was observed [27] [28] and was attributed to an increase in non-stoichiometric

oxygen content.

The main objective of this study is to research YBCO material doped with GO and rGO in the range of 0.1 -1.0 %wt, in order to investigate the effects of these dopants on the following properties: T_C, Vickers hardness, mechanical properties (B, E, Y, K_{IC}) and the weak-link effects of bulk material.

If there are any changes to these properties what is/are the responsible mechanism/s?

[Interestingly, there are no publications that compare GO and rGO doping of YBCO in one investigation.]

1.6 Contributions

1.6.1 Paper Contributions

The research presented in this thesis, consists of five published research articles, three journal and two conference papers. For the sake of repetition, the 'summary' conference paper titled "Effect of Graphene Oxide Doping on Bulk High Temperature Superconductors for Power Applications" presented at South African Universities Power Engineering Conference (SAUPEC) in 2019, is not presented as part of this thesis.

1.6.1.1 Paper 1

Title: Effect of Graphene Oxide Doping on Bulk High Temperature Superconductors for Power Applications

Authors: Mohammed Zaahid Gaffoor, Alan Lawrence Leigh Jarvis and Solan Perumal

Publication Type: Conference Article – peer reviewed

Status: Published in Proceedings of the Southern African Universities Power Engineering Conference (SAUPEC), May 2019

In this paper the samples were limited to three: an YBCO control, and YBCO doped with 0.5 % wt. and 0.7 % wt. GO. The experimental stage, discussed in Appendix A, comprised of Helmholtz coils which were purposely designed in order to conduct measurements in zero field cooling (ZFC) and FC conditions. Sintering profile for YBCO sample preparation and electrical connection to bulk samples are included in this paper. Using this experimental stage measurements were carried out in ZFC and FC conditions. An increase in T_C and a reduction in the weak-link effect was observed. The increase in T_C was attributed to an increase non-stoichiometric oxygen content and the reduction in the weak-link effect was concluded to be due to improved grain connectivity and increase in flux pinning sites.

1.6.1.2 Paper 2 (Chapter 2)

Title: Comparison of the Effect of Graphene and Graphene Oxide Doping on YBCO

Authors: Mohammed Zaahid Gaffoor and Alan Lawrence Leigh Jarvis

Publication Type: Journal Article - peer reviewed

Status: Published in Journal of Physics: Conference series, 2020

This article shows the comparison of YBCO doped with GO and rGO in the following concentrations: 0.1, 0.5, 0.7, 0.9, 1 % wt. . The T_C for both GO and rGO doped samples increased. The increase in GO doped samples was greater than in rGO doped samples. This was attributed to GO having more oxygen that rGO therefore making the non-stoichiometric oxygen content greater in GO than in rGO doped samples. The weak-link effect was reduced in both GO and rGO due to improved grain connectivity. There was an increase in flux pinning sites due to rGO nano-particles forming pinning centers. Micro-hardness in both GO and rGO samples was hypothesized to have increase as a result of strain locking fields caused by GO and rGO nano-particles.

1.6.1.3 Paper 3 (Chapter 3)

Title: Comparison of Graphene Oxide and Reduced Graphene Oxide Doping on YBCO for Power Applications

Authors: Mohammed Zaahid Gaffoor, Alan Lawrence Leigh Jarvis and Solan Perumal

Publication Type: Conference Article - peer reviewed

Status: Published in Proceedings of the Southern African Universities Power Engineering Conference (SAUPEC), 2020

This conference paper is a follow on from Paper 2. Increase in the non-stoichiometric oxygen content of GO and rGO doped samples were confirmed using iodometric titration. TEM images were taken showing graphene sheets at grain boundaries therefore confirming how improved grain connectivity occurs, which reduces the weak-link effect.

1.6.1.4 Paper 4 (Chapter 4)

Title: Mechanical and Structural Properties of Graphene Oxide and Reduced Graphene Oxide doped

Authors: Mohammed Zaahid Gaffoor, Alan Lawrence Leigh Jarvis and Andrew Swanson

Publication Type: Journal Article - peer reviewed

Status: Published by IEEE Transaction on Applied Superconductivity, 2023

This journal article does an in-depth analysis of the mechanical properties of GO and rGO doped YBCO. It is a continuation of the Vickers hardness measurements carried out in paper 2. The micro-hardness measurements were used to calculate elastic modulus, fracture toughness, brittleness index and yield strength. These parameters were enhanced greatly due to rGO and GO doping. The micro-hardness characteristics were modeled using the Hays Kendall, elastic plastic deformation and the proportional sample resistance model in order to determine which model best describes the micro-hardness characteristics. XRD was carried out to confirm Y123 phase of doped samples. Orthorhombicity, lattice strain, lattice parameter and crystallite size were calculated from this diffraction pattern. Orthorhombicity improved and lattice strain decreased for GO and rGO samples. Porosity of the samples were observed to decrease. Iodometric measurements were carried out to determine oxygen content of samples and was validated using XRD.

1.6.1.5 Paper 5 (Chapter 5)

Title: Effects of Graphene Oxide doping on the Critical Transitional Temperature of Bulk YBCO.

Authors: Mohammed Zaahid Gaffoor, Alan Lawrence Leigh Jarvis, and Jonathan Celvin Archer

Publication Type: Journal Article - peer reviewed

Status: Published in Results in Physics, 2023.

This journal article offers a mechanism explaining the increase in T_C above 93 K in certain GO doped samples in paper 1, paper 2, paper 3, paper 4 and previous GO doping research. The hypothesis and proof offered to this increase in T_C is unique, and is the first time were the increase in T_C for YBCO GO-doped experiments [27] [28] is associated with impurities (manganese) found in GO rather than GO itself.

YBCO was doped with TS-GO and TU-GO in the following weight concentrations: 0.1, 0.5 and 0. 7 % wt. XRD analyses showed that the atomic site occupancies varied marginally. Thus confirming that the GO remains at grain boundaries. Lattice strain decreased in both TS-GO and TU-GO doped samples. The increase in T_C in TU-GO doped samples is greater than in TS-GO doped samples a maximum T_{Con} of 100 K was reached. After research was conducted on the cause of this increase above 93 K. It was hypothesized that the formation of magnetic manganese impurities in YBCO resulted from manganese impurities found in GO, more noticeably in TU-GO than TS-GO as TU-GO contained more impurities. Magnetic impurities were collected from YBCO doped GO samples using a magnet and were identified as manganese oxide.

Thereafter to confirm this increase in T_C was associated with manganese oxide impurities, YBCO was doped with manganese oxide impurities. The T_{Con} was seen to increase above 93 K, to as high as 115 K. Initial T_C measurements were determined from R(T) measurements, thereafter confirmed using AC susceptibility experiment, with a detailed apparatus discussion in Appendix A - R vs. T Experimental Procedure and Appendix B – AC Susceptibility Experimental Procedure. Finally, a linked was discovered between improved T_C and the flatness of the copper oxide planes.

1.6.2 Novel Contributions

- A hypothesis and proof offered regarding the increase in T_C for YBCO GO-doped experiments.
- Identifying and characterizing magnetic manganese impurities found in YBCO due to GO doping.
- Micro-hardness measurements of GO and rGO doped YBCO.
- Modelling of micro-hardness measurements using Hays-Kendall, elastic plastic deformation and proportional sample resistance model.
- Calculation of fracture toughness for GO and rGO doped YBCO samples.

This original work is in the form of a thesis by publication. The following chapters are standalone publications that have been peer reviewed and published.

References

[1] J. Bednorz and K. Muller, "Possible High T c Superconductivity in the Ba - La- Cu- 0 System," *Z. Physik B - Condensed Matter ,* pp. 189-193, 1986.

[2] J. Hirsch, "BCS Theory of Superconductivity: It is Time to Question its Validity," *Physica Scripta,* 2009.

[3] C. Chu, P. Hor, R. Meng, L. Gao, Z. Huang and Y. Wang, "Evidence for Superconductivity above 40 K in the La-Ba-Cu-0 Compound System," *Physical Review Letters,* vol. 58, no. 4, 1987.

[4] M. K. Wu, J. R. Asburn, C. J. Torng, P. H. Hor, R. L. Meng, L. Gao, Z. J. Huang, Y. Q. Wang and C. W. Chu, "Superconductivity at 93 K in a New Mixed-Phase Y-Ba-Cu-O Compound System at Ambient Pressure," *Physical Review Letters,* vol. 58, no. 9, pp. 908-910, 1987.

[5] M. Cyrot and D. Pavuna, Introduction to Superconductivity and High Tc Materials, World Scientific Publishing Co.Pty.Ltd, 1992.

[6] R. Hazen, C. Prewitt, R. Angel, N. Ross, L. Finger, C. Hadidiacos, D. Veblen, P. Heaney, P. Hor, R. Meng, Y. Sun, Y. Wang, Y. Xue, Z. Huang, L. Gao, J. Bechtold and C. Chu, "Superconductivity in the High-T, Bi-Ca-Sr-Cu-O System: Phase Identification," *Physical Review Letters*, vol. 60, 1988.

[7] C. Chu, J. Bechtold, L. Gao, P. Hor, Z. Huang, R. Meng, Y. Sun, Y. Wang and Y. Xue, "Superconductivity up to 114K in the Bi-Al-Ca-Sr-Cu-O Compound System without Rare-Earth Elements," *Physical Review Letters,* vol. 60, no. 10, pp. 941-943, 1988.

[8] C. Chu, L. Gao, F. Chen, Z. Huang, R. Meng and Y. Xue, "Superconductivity above 150 K in HgBa2Ca2Cu3O8+x," *Letter to Nature,* vol. 365, pp. 323-325, 1993.

[9] K. Moorjani, F. J. Adrian, J. B. Boris F. Kim, T. E. Phillips, T. J. Kistenmacher, W. J. Green, E. Agostinelli, B. G. Boone and R. M. Soya, "High-Temperature Superconductivity," *Johns Hopkins APL Technical Digest*, pp. 158-159, 1990.

[10] H.Hilgenkamp and J.Mannhart, "Grain Boundaries in High-T_c Superconductors," *Reviews of Modern Physics,* vol. 74, 2002.

[11] K. Taylor, D. Misra, D. Matthews and G. Alvarez, "The Percolation Limit and Weak Link Effects on the Superconducting Phase Transition in High Temperature Superconductors," *Phase Transitions,* vol. 22, pp. 103-119, 1990.

[12] M. B. Turkoz, S. Nezir, O. Ozturk, E. Asikuzun, G. Yildirim, C. Terzioglu and A. Varilci, "Experimental and Theoretical Approaches on Mechanical Evaluation of Y123 System by Lu Addition," *J Mater Sci: Mater Electron,* vol. 24, p. 2414–2421, 2013.

[13] F. M. Costa, N. M. Ferreira, S. Rasekh, A. J. Fernandes, M. A. Torres, M. A. Madre, J. C. Diez and A. Sotelo, "Very Large Superconducting Currents Induced by Growth Tailoring," *Crystal Growth and Design,* vol. 15, no. 5, pp. 2094 - 2101, 2015.

[14] R. Sharma, "Springer Series in Material Science," in *Superconductivity Basics and Applications to Magnets*, pp. 78-80.

[15] J. MacManus-Driscoll and S. Wimbush, "Future Directions for Cuprate Conductors," *IEEE Transactions on Applied Superconductivity,* vol. 21, no. 3, pp. 2495-2500, 2011.

[16] K. Jasima, S. Makki and A. Almohsin, "Comparison Study of Transition Temperature Between the Superconducting Compounds $Tl_{0.9}$ $Pb_{0.1}Ba_2Ca_2Cu_3O_{9-x}$, $Tl_{0.9}Sb_{0.1}Ba_2Ca_2Cu_3O_{9-x}$ and $Tl_{0.9}Cr_{0.1}Ba_2Ca_2Cu_3O_{9-x}$," in *Physics Procedia*, 2014.

[17] F. R. Fickett, "Standards for Measurement of the Critical Fields of Superconductors," *Journal of Rescarch of the National Burwau of Standards,* vol. 90, no. 2, 1985.

[18] Y. Bruynseraede, J. Vanacken, B. Wuyts, C. V. Haesendonck, J. Locquet and I. K. Schuller, "Oxygen Disorder Effects in High T_c Superconductors," *Physica Scripta,* vol. Vol. T29, pp. 100-105, 1989.

[19] S. Regnier, C. Alfred-Duplan, G. Vacquier and J. Marfaing, "Effect of Mn Inclusion in

Superconducting YBCO-Based Composites," *Applied Superconductivity,* vol. 4, no. 112, pp. 41-51, 1996.

[20] J. Marfaing and S. Regnier, "Effect of Sintering on the Transport Properties and Microstruetures of Mn-YBCO Composites," *Physica C,* pp. 1513-1514, 1994.

[21] S. Regnier and J. Marfaing, "Detailed Analysis of the Zero Critical Temperature Improvement in Mn-$YBa_2Cu_3O_{7-x}$ Composites from Electrical and Structural Studies," *Materials Science and Engineering B,* pp. 116-123, 1995.

[22] R. Jardim, S. Gama, O. de Lima and I. Torriani, "Effect of Mn on the Superconductivity of $Y_1Ba_2Cu_3O_{7-x}$," *Physical Review B,* vol. 38, no. 7, 1988.

[23] R. Jardim and S. Gama, "Enhanced Grain Growth in $Y_1Ba_2(Cu_{1-x}Mnx)O_{7-x}$ Compounds," *Physica C,* pp. 306-312, 1989.

[24] A. Salama, M. El-Hofy, Y. Rammah and M. Elkhatib, "Effect of Magnetic and Nonmagnetic Nano Metal Oxides Doping on the Critical Temperature of a YBCO Superconductor," *Advanced Natural Science: Nanoscience and Nanotechnology,* vol. 6, 2015.

[25] A. Salama, M. El-Hofy, Y. Rammah and M. Elkhatib, "The Influence of Magnetic Nano Metal Oxides Doping on Structure and Electrical Properties of YBCO Superconductor," *Advances in Natural Sciences: Nanoscience and Nanotechnology,* vol. 7, 2016.

[26] Y. Rammah, A. Salama and M. Elkhatib, "Magnetic Moment and its Correlation with the Critical Temperature in YBCO," *Interceram,* vol. 68, pp. 34 - 40, 2019.

[27] S. Dadras, S. Dehghani, M. Davoudiniya and S. Falahati, "Improving Superconducting Properties of YBCO High Temperature Superconductor by Graphene Oxide Doping," *Materials Chemistry and Physics,* vol. 193, pp. 496-500, 2017.

[28] S. Dadras, S. Falahati and S. Dehghani, "Effects of Graphene oxide Doping on the Structural and Superconducting Properties of $YBa_2Cu_3O_{7-x}$," *Physica C,* vol. 548, pp. 65-67, 2018.

[29] M. Shoushtari, M. Akbari and Y. Hajati, "Study of $YBa_2Cu_3O_{7-\delta}$ Superconductor/Graphene Oxide Composite," *Journal of Superconductivity and Novel Magnetism,* 2018.

[30] C. Wonga, Z. Soferb, M. Kubešovác, J. cerac, S. ejkovád and M. Pumera, "Synthetic Routes Contaminate Graphene Materials with a Whole Spectrum of Unanticipated Metallic Elements," *Proceedings of the National Academy of Sciences of the United States of America,* vol. 111, no. 38, 2014.

[31] A. L. L. Jarvis and T. B. Doyle, "The Influence of Ag Doping on the Superconducting Properties of Grain-boundary Weak-links in YBCO," *Applied Superconductivity,* vol. 1 and 2, no. 158, pp. 1149-1152, 1997.

[32] K. Inoue, Y. Miyake, M. Miryala and M. Murakami, "Effects of Carbon Nanotube Addition on Superconductivity in Y-Ba-Cu-O Bulk Superconductors," *Journal of Physics: Conference Series,* 2017.

[33] A. Kilic, "Analysis of the Current-Voltage Characteristics and Transport Critical Current Density of Superconducting $YBa_2Cu_3O_{7-x}$ in the Self-field Approximation," *Superconductor Science and Technology,* pp. 497-503, 1995.

[34] S. Graser, P. J. Hirschfeld, T. Kopp, R. Gutser1, B. M. Andersen and J. Mannhart, "How Grain Boundaries Limit Supercurrents in High-Temperature Superconductors," *Nature Physics,* vol. 6, pp. 609-614, 2010.

[35] J. Zheng, X. Liao, H. Jing, Q. Lin, G. Ma, F. Yen, S. Wang and J. Wang, "Anisotropy Effect on Levitation Performance of Bulk High-T_c Superconductors Above a Permanent Magnet Guideway," *Physics Procedia,* vol. 36, 2012.

[36] R. A. Doyle, A. D. Bradley, W. Lo, D. A. Cardwell and A. M. Campbell, "Intragranular and Intergranular Superconducting Properties Bulk Melt-Textured YBCO," *IEE Transactions on Applied Superconductivity,* vol. 9, no. 2, 1999.

[37] J. G. Ossandon, J. R. Thompson, D. K. Christen, B. C. Sales, H. R. Kerchner, J. O. Thomson, Y. R. Sun, K. W. Lay and J. E. Tkaczyk, "Influence of Oxygen Deficiency on the superconductive

properties of grain- aligned $YBa_2Cu_3O_{7-X}$," *Physical Review B,* vol. 45, no. 21, 1992.

[38] B. Malik, M. Malik and K. Asokan, "Enhancement of the Critical Current Density in YBCO/Ag Composites," *Chinese Journal of Physics,* pp. 170-175, 2017.

[39] S. Dadras and M. Ghavamipour, "Investigation of the Properties of Carbon-base Nano Structures Doped $Y_1Ba_2Cu_3O_{7-\delta}$ High Temperature Superconductor," *Physica B,* pp. 13-17, 2016.

[40] S. Falahati, S. Dadras and J. Mosqueira, "Investigation of the Magnetic and Transport Properties of $YBa_2Cu_3O_{7-\delta}$ High Temperature Superconductor Doped with Graphene Oxide," *Journal of Superconductivity and Novel Magnetism,* 2019.

[41] M. J. Qin and S. X. Dou, "Superconductors, High Tc," in *Encyclopedia of Condensed Matter Physics*, ScienceDirect, 2005, pp. 112 -120.

[42] A. Galluzzi, K. Buchkov, E. Nazarova, A. Leo, G. Grimaldi, A. Pace and M. Polichetti, "Silver doping effects on irreversibility field and pinning energy of a FeSe iron based superconductor," in *Journal of Physics: Conference Series*, Rome, 2019.

[43] K. Chen and Y. quan, "Critical Current and Magnetoresistance Hysteresis in Polycrystalline $Y_1Ba_2Cu_3O_{7-X}$," *Physica C* , vol. 159, pp. 131-136, 1989.

[44] R. Terzioglu, S. Altintas, A. Varilci and C. Terzioğlu, "Modeling of Micro-Hardness in the Au-Doped YBCO Bulk Superconductors," *Journal of Superconductivity and Novel Magnetism,* 2019.

[45] T. Oka, F. Ogasawara, Y. Itoh, M. Suganuma and U. Mizutani, "Mechanical and Superconducting Properties of Ag/YBCO Composite Superconductors Reinforced by the Addition Zr," *Japanese Journal of Applied Physics,* vol. 29, pp. 1924-1931, 1990.

[46] W. Smith and J. Hashemi, "Mechanical Properties of Metals |," in *Foundations of Materials Science and Engineering*, McGraw-Hill, pp. 239-272.

[47] B. Sahoo, A. K. Singh and D. Behera, "Graphene oxide modified superconducting and elastic parameters of YBCO superconductor," *Materials Chemistry and Physics* , vol. 240, p. 122252, 2020.

[48] B. Sahoo and D. Behera, "Study of Transport and Elastic Properties of YBCO Superconductors by Inclusions of GnPs," *Physica C : Superconductivity and its Applications,* vol. 578, p. 1353748, 2020.

[49] B. Jung, H. Lee and H. Park, "Effect of grain size on the indentation hardness for polycrystalline materials by the modified strain gradient theory," *International Journal of Solids and Structures,* vol. 50, no. 18, pp. 2719 - 2724, 2013.

[50] U. Kölemen, S. Çelebi, H. Karal, A. Öztürk, U. Çevik and a. O. G. S. Nezir, "Superconducting and Vickers Hardness Properties of ZnO-added YBCO Polycrystalline Superconductors," *physica status solidi (b),* vol. 241, no. 6, pp. 274-283, 2004.

[51] H. Ling and M. Van, "Microhardness Measurements on Dopant Modified Superconducting $Y_1Ba_2Cu_3O_7$ Ceramics," *Journal of Applied Physics,* pp. 1307-1311, 1988.

[52] B. Sahoo, K. L. Routray, D. Samal and D. Behera, "Effects of Artificial Pinning Centers on YBCO High Temperature Superconductors Through Substitution of Graphene Nano-platelets," *Materials Chemistry and Phsyics,* vol. 223, pp. 784 - 788, 2019.

[53] K. Fabian, V. P. Shcherbakov and S. A. McEnroe, "Measuring the Curie temperature," *Geochemistry, Geophysics, Geosystems,* vol. 14, no. 4, pp. 947 - 961, 2013.

[54] A. Tavana and M. Akhavan, "How T_C can go above 100 K in the YBCO family," *The European Physical Journal B,* vol. 73, pp. 79-83, 2010.

[55] O. Chmaissem, J. Jorgensen and S. Short, "Scaling of transition temperature and CuO2 plane buckling in a high-temperature superconductor," *Nature,* vol. 397, pp. 45-48, 1999.

[56] B. Mundet, S. T. Hartman, R. Guzman, J. C. Idrobo, X. Obradors, T. Puig, R. Mishra and J. Gazquez, "Local strain-driven migration of oxygen vacancies to apical sites in YBa2Cu3O7−x," *Nanoscale,* vol. 12, p. 5922–5931, 2010.

[57] X. J. Chen and H. Q. Lin, "Pressure Dependence of Tc in Y-Ba-Cu-O Superconductors," *Physical Review Letter,* vol. 85, no. 10, pp. 2180 - 2183, 2000.

[58] R. Ofer, A. Keren, O. Chmaissem and A. Amato, "Universal doping dependence of the ground state staggered magnetization of cuprate superconductors," *Physical Review B,* vol. 78, p. 140508, 2008.

[59] Z. Yang, Q. Q. Zheng, H. H. Qiu, J. L. LI and J. J. Y. Yang, "A Simple Method for the Reduction of Graphene Oxide by Sodium Borohydride with $CaCl_2$ as a Catalyst," *New Carbon Materials,* vol. 30, no. 1, pp. 41- 47, 2015.

[60] I. Sengupta, S. Chakraborty, M. Talukdar, S. K. Pal and S. Chakrabortya, "Thermal Reduction of Graphene Oxide: How Temperature Influences Purity," *Journal of Materials Research* , vol. 33, no. 23, pp. 4113-4122, 2018.

[61] B. Somnath and R. Kumar, "A Review on the Properties and Applications of Graphene," *Journal of Material Science and Mechanical Engineering,* vol. 2, pp. 70-73, 2015 .

[62] K. S. Novoselov, A. K. Geim, S. V. Morozov, D. Jiang, Y. Zhang, S. V. Dubonos, I. V. Grigorieva and A. A. Firsov, "Electric Field Effect in Atomically Thin Carbon Films," *Science,* pp. 666-669, 2004.

[63] S. Sali, H. Mackey and A. Abdala, "Effect of Graphene Oxide Synthesis Method on Properties an Performance of Polysulfone-Graphene Oxide Mixed Matrix Membranes," *Nanomaterials,* vol. 9, no. 5, 19 May 2019.

[64] D. C. Marcano, D. V. Kosynkin, J. M. Berlin, A. Sinitskii, Z. Sun, A. Slesarev, L. B. Alemany, W. Lu and J. M. Tour, "Improved Synthesis of Graphene Oxide," *ACS NANO,* vol. 4, no. 8, p. 4806–4814, 2010.

[65] Z. Benzait and L. Trabzon, "Graphite Size Effect on Chemical Expansion and Graphene Oxide Properties," *ASC OMEGA,* 2022.

[66] S. Stankovich, D. A. Dirkin, R. D. Piner, K. A. Kohlhaas, A. Kleinhammes, Y. Jia, Y. Wu, S. T. Nguyen and R. S. Ruoff, "Synthesis of graphene-based nanosheets via chemical reduction of exfoliated graphite oxide," *Carbon,* vol. 45, no. 7, pp. 1558 -1565, 2007.

[67] H. R. Thomas, S. P. Day, W. E. Woodruff, C. Valles, R. J. Young, I. A. Kinloch, G. W. Morley, J. V. Hanna, N. R. Wilson and J. P. Rourke, "Deoxygenation of Graphene Oxide: Reduction or Cleaning?," *Chemistry of Materials,* pp. 3580 - 3588, 2013.

[68] S. K. Ghosh, "Diversity in the Family of Manganese Oxides at the Nanoscale: From Fundamentals to Applications," *ACS OMEGA,* vol. 5, pp. 25493 - 25504, 2020.

[69] S. Fritsch and A. Navrotsky, "Thermodynamic Properties of Manganese Oxide," *Journal of the American Ceramic Society,* vol. 7, pp. 1761- 1768, 1996.

[70] S. G. Sanfelix, "Manganese Oxide Nanoparticles: Synthesis and Magnetic Properties," Universitat Marburg, Marburg, 2008.

[71] C. Zhou, J. Wang, X. Liu, F. Chen, Y. Di, S. Gao and Q. Shi, "Magnetic and thermodynamic properties of α, β, γ and δ-MnO_2," *New Journal of Chemistry,* no. 11, 2018.

[72] B. Ding, P. Zheng, P. Ma and J. Lin, "Manganese Oxide Nanomaterials: Synthesis, Properties and Theranostic Applications," *Advanced Materials,* p. 1905823, 2020.

[73] D. M. Tinsley and J. H. Sharp, "THERMAL ANALYSIS OF MANGANESE DIOXIDE IN CONTROLLED ATMOSPHERES," *Journal of Thermal Analysis,* vol. 3, pp. 43-48, 1971.

Chapter One Summary

In this chapter a literature review was conducted on the scientific concepts used in this research and the research that has been conducted thus far on the topic of doping GO and rGO. Thereafter it was discussed how the research presented in this thesis extends the knowledge of this topic.

The start of this research commences in chapter 2. The first step was to dope YBCO with GO and rGO and observe if there were any variations in T_C of YBCO. Microhardness measurements were also conducted to determine if there was any enhancements in the mechanical parameters of the material.

Chapter 2

Peer-Reviewed Journal Article 1

Comparison of the Effect of Graphene and Graphene Oxide Doping on YBCO

Mohammed Zaahid Gaffoor, Alan Leigh Lawrence Jarvis, Edward Young and David Dorrell

Published: *Journal of Physics Conference Series (2020)*

DOI: *http://dx.doi.org/10.1088/1742-6596/1559/1/012028.*

2.1 Abstract

Weak-links in high temperature superconductors (HTS) are a result of an incorrect stoichiometric ratio found in grain boundaries and misaligned planes. These weak-links severely decrease the critical transport current of the bulk HTS material (such as YBCO) and increase resistance in the normal state. Bulk YBCO was doped with graphene oxide (GO) and reduced graphene oxide (rGO) in the following dopant concentrations: 0, 0.1, 0.5, 0.7, 0.9 and 1 % wt. Through mechanical hardness testing, it was observed that the hardness of the samples increased as the GO and rGO concentration increased. The 1 % wt. doped GO and rGO samples were observed to be hardest, with a true hardness of 2.630 GPa and 2.405 GPa respectively, compared to the control sample with a true hardness of 1.499 GPa. Critical transition temperature (T_C) of the GO doped YBCO samples are greater than rGO doped samples and is presumably related to the higher oxygen content found in GO. The 0.7 % wt. doping for GO and rGO samples had the highest critical transition temperature of 98 K and 91 K, respectively. Both GO and rGO samples showed a decrease in normal resistance up to 0.7 % wt. doping, compared to the control sample. The weak-link effect was most improved in the 0.7 % wt. doped samples for GO and rGO.

2.2 Introduction

YBCO was discovered in 1987 with a critical transition temperature of 92 K [1]. This was of importance as 92 K is above the boiling point of liquid nitrogen. There has been constant research in order to improve mechanical and superconducting properties of bulk YBCO material. The poor critical current of bulk YBCO material is attributed to a network of weak-links in bulk material [2]. Magnetic levitation applications, such as flywheels, are also hindered due to the fact that the repulsive force between the permanent magnet and the superconductor will be weak. This is caused by the superconductor being unable to generate large surface currents to produce an opposite and equal magnetic field to allow for magnetic levitation in stronger fields [3].

In levitation applications, an increase in flux pinning sites can help improve magnetic stiffness, thus increasing stability in the lateral axis of levitation [4]. This increase in magnetic stiffness allows for improved damping and a larger region of stability [5]. This improvement in the stability allows for larger angular velocities, thus increasing the amount of energy stored [4] [6].

Past research has shown that doping bulk YBCO material can improve its mechanical and superconducting properties. Doping YBCO with silver decreases its normal resistivity, increases flux pinning sites and its critical current density [2]. Zinc Oxide doping of YBCO improves hardness of the material [7]. Graphene oxide doping of MgB_2 has been reported to improve the grain boundary connectivity, increase critical current and the number of flux pinning sites [8]. Graphene oxide (GO) doping of YBCO has been found to improve flux pinning, grain connectivity, increase T_C and critical current in bulk material [9].

There has been a number of studies on the doping of YBCO with GO [9] [10], but no comparison of GO and reduced GO (rGO). In this research, YBCO bulk material was doped with GO and rGO in order to study the role that oxygen and graphene play in observed improvements in bulk material.

2.3 Experimental

GO was produced using the Hummers method with additional potassium permanganate [11]. GO was reduced to rGO using $NaBH_4$ and $CaCl_2$ as a catalyst [12]. YBCO bulk powder obtained from Superconductor Technologies Inc. was doped with GO and rGO in the following concentrations: 0, 0.1, 0.5, 0.7, 0.9, and 1 % wt. . Thereafter, these powders were pressed into pellets with a diameter of 12 mm and a thickness of 2 mm at pressure of 45 MPa. Pellets were then sintered at 950˚C in an oxygen atmosphere for 6 hours. R vs. T measurements were taken in field cooled (FC) and zero field cooled (ZFC) conditions. Resistance was measured using the four-wire resistance method. In order to measure the foot structure of the R vs. T curves to determine the effect on the weak-links, a variable of ΔT_C was defined as:

$$\Delta T_C = T_{CONSET} - T_{COFF} \tag{2.1}$$

Vickers hardness testing was carried out at a temperature of 297 K. The following load forces were: 25 g, 50 g, 100 g, 200 g and 300 g with a load contact time of 10 s using a pyramid indenter shown in Figure 2:1. Several indentations were made for each load in order to achieve the optimum mean value for Vickers hardness, H_V.

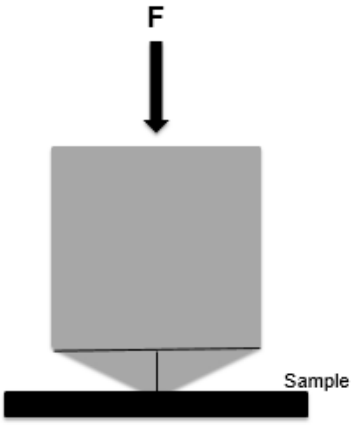

Figure 2:1 : Vickers hardness indenter applying load on sample surface

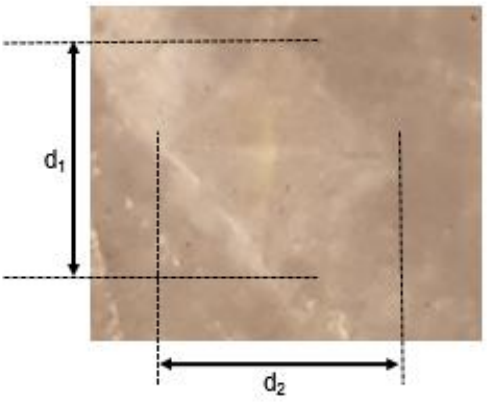

Figure 2:2 : Diamond shaped indentation on sample surface with diagonals d_1 and d_2.

Equation 2.2 was used to determine H_V,were d is the mean value of diagonals d_1 and d_2 measured from the indentation on the sample surface seen in Figure 2:2 and F is the applied load [7].

$$H_V = 1854\frac{F}{d^2} \tag{2.2}$$

There are two types of models to describe load dependent hardness [13]. One model considers energy-dissipative processes and the other model considers elastic processes during indentation. The energy-dissipative processes approach was considered [13]. In order to determine a true load independent hardness, H_O, the following equation was used,

$$H_O = 1854.4\frac{F - F_O}{d^2} \tag{2.3}$$

where F_O is the energy dissipative portion of the load [7] [13]. H_O and F_O was determined from the plot of F vs. d^2.

2.4 Results and Discussion

Figure 2:3 (a) and Figure 2:3 (b) shows transmission electron microscope (TEM) images of 2D GO and rGO sheets, respectively.

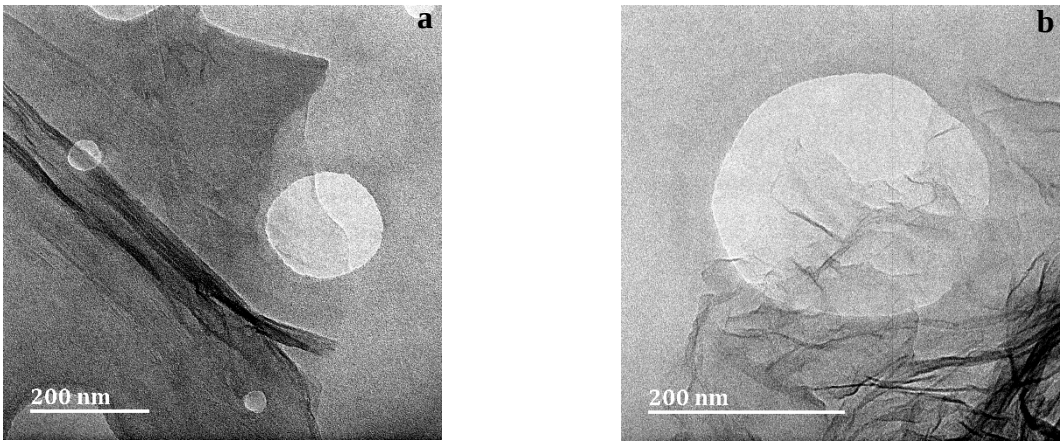

Figure 2:3 : TEM images of a) multilayered (2-3 layers) GO and b) a single sheet of rGO

Fourier transform infrared spectroscopy (FTIR) in Figure 2:4 was used to determine the amount of oxygen groups in the graphite, GO and the rGO material. The O-H group in the graphite sample is due to intercalated water which occurs in natural graphite, the precursor material used for the production of GO [14]. Oxidation of the graphite to produce GO can be seen by the increase in oxygen functional groups and the increase in the size of the O-H peak in the GO sample. In the rGO sample, the oxygen functional groups are reduced which can be seen by the reduction in peak sizes compared to the rGO sample. This can be seen by the reduction in the size of the O-H, C=O and C-O peaks.

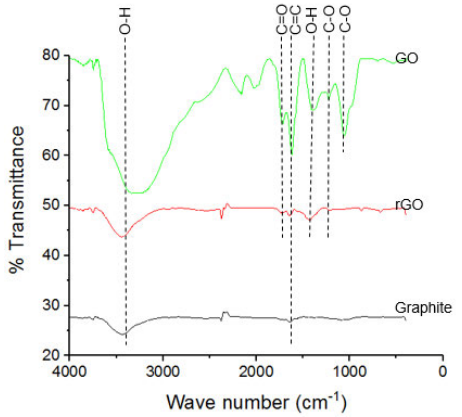

Figure 2:4 : FTIR for graphite, GO and rGO

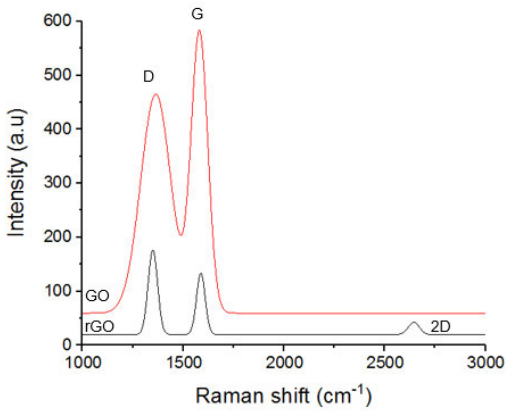

Figure 2:5 : RAMAN spectrum of GO and rGO

The RAMAN spectrum of GO and rGO are shown in Figure 2:5 and are consistent with typical RAMAN spectrum plots to be found in other studies of GO and rGO [15] [16]. The D band is a result of out of plane vibrations which is due to structural defects and the G band is caused by in plane vibrations of sp^2 carbon atoms [15]. The D peaks occur at 1363 cm^{-1} and 1348 cm^{-1} and G peaks at 1589 cm^{-1} and 1579 cm^{-1}, in GO and rGO respectively. The intensity of the

D peak is greater in GO than in rGO which is due to a larger number of defects in GO. This results in the disruption of sp^2 bonds thus creating more sp^3 bonds [15] [16]. The G peak in rGO is shifted to a lower wave number compared to GO which is due to an increase in the number of sp^2 bonds [16].

The full width half maximum (FWHM) of the D peaks for GO and rGO are 177.76 and 54.45 and for the G peaks it is 101.69 and 50.02 respectively. The decrease in the FWHM for the D and G bands from the GO to reduction to rGO signifies a decrease in disorder in the rGO material which is associated with a reduction in oxygen [15] (this reduction of oxygen in the form of bubbles was observed during the reduction step of GO to rGO when the $NaBH_4$ was added to the GO solution) [15]. The 2D band in the rGO occurs at 2644.08 cm^{-1} and is a unique feature of GO approaching true graphene (G) material. The ratio of I_{2D} / I_G for the rGO is 0.32 which means that it is multi layered [17].

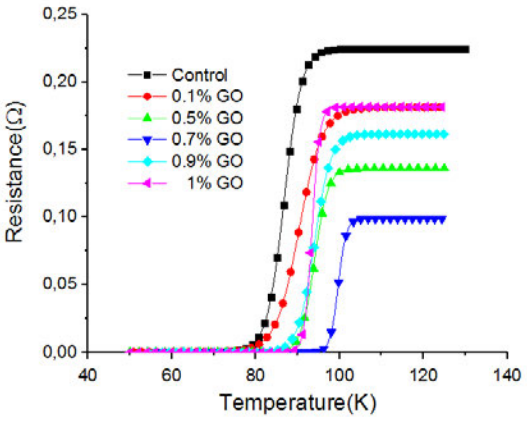

Figure 2:6 : ZFC R (T) curves for all GO doped samples

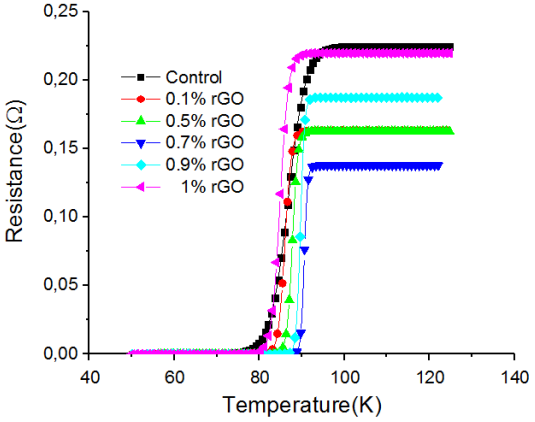

Figure 2:7 : ZFC R (T) curves for all rGO doped samples

The transition from superconducting to a complete normal state occurs over a smaller temperature range in rGO doped samples than in GO doped samples, as shown in Figure 2:6 and Figure 2:7. In Table 2:1, ΔT_C characterizes this transition and is seen to be smaller in rGO doped samples compared to GO doped samples. This decrease in foot structure in rGO doped samples compared to GO doped samples signifies a reduction in weak-links at the grain boundaries in rGO samples than in GO doped samples [18].

The critical transition temperature T_{Cmid} is defined as the mid-point between the T_{Conset} and the T_{Coff} [19]. This is shown for GO and rGO samples in Table 2:1 and are all greater than the control. The transition temperature for GO doped samples are greater than rGO doped samples. This is due to the GO having a higher oxygen content than rGO, resulting in better oxygenation of the grains in GO doped samples than rGO doped samples [9] [10].

Table 2:1 : Analysis of ZFC curves

	Sample										
	Control	GO doped YBCO (% wt.)					rGO doped YBCO (% wt.)				
		0.1	0.5	0.7	0.9	1	0.1	0.5	0.7	0.9	1
T_{Cmid} (K)	84	90	92	98	93	91	86	88	91	89	85
ΔT_C (K)	13	13	11	8	12	10	8	7	4	5	6
Resistance at T = 120 K (Ω)	0.225	0.181	0.136	0.099	0.161	0.182	0.163	0.163	0.138	0.187	0.220

The normal resistivity of GO and rGO doped samples shown in Table 2:1 are smaller in comparison to the control sample. This could be attributed to GO and rGO being reduced to nearly pure graphene during the sintering process at temperatures above 650˚C, that is, thermal reduction. Graphene, being a good conductor, would improve grain boundary connectivity in samples thereby reducing the normal resistance [9].

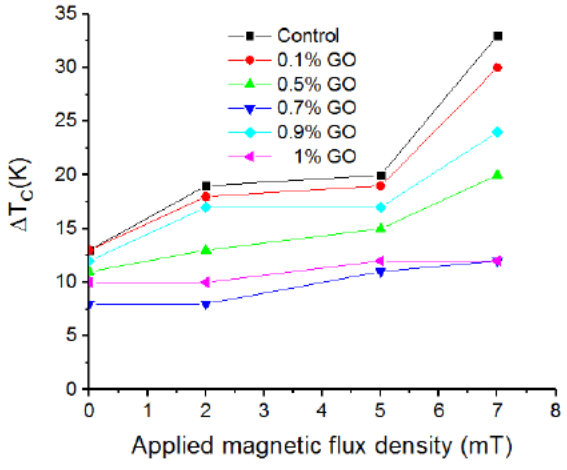

Figure 2:8 : Applied Magnetic Flux density vs. ΔT_C for GO doped samples

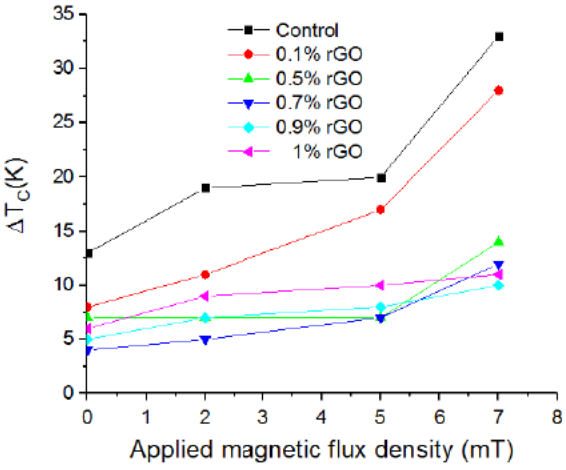

Figure 2:9 : Applied Magnetic Flux density vs. ΔT_C for rGO doped samples

FC measurements of the samples are shown in Figure 2:8 and Figure 2:9. It can be seen that ΔT_C of the samples increase with an increase in the applied magnetic field. This is a manifestation of the grain-boundary weak-link effect. ΔT_C of GO and rGO samples are smaller than that of the control sample thus showing an improvement in grain boundary connectivity. rGO doped samples have a lower ΔT_C than GO doped samples for the same dopant weighting. The 0.7 % wt. doped sample for GO and rGO sample sets exhibit the most improved grain connectivity for applied magnetic fields below 6 mT At applied magnetic fields above 6 mT the ΔT_C for the 0.9 and 1.0 %wt. rGO doped samples is smaller than the 0.7 %wt. rGO doped sample. This trend is also observed when comparing the 0.7 and 1.0 %wt. GO doped samples.

This can be attributed to the higher number of flux pinning sites in the 0.9 and 1.0 %wt. doped samples due to the higher dopant concentrations. Thus allowing those 0.9 and 1.0 %wt. to withstand higher applied magnetic fields.

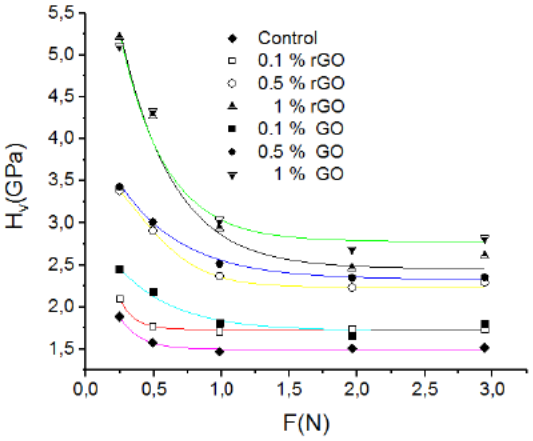

Figure 2:10 : Vickers hardness, H_v vs. applied load, F, for GO and rGO doped samples.

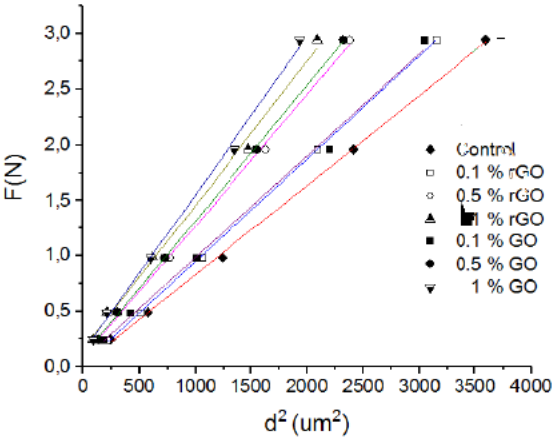

Figure 2:11 : Applied load, F vs. the diagonal of the impression squared, d^2, for GO and rGO doped samples.

The load dependent hardness relationship is shown in Figure 2:10. It is observed that as the applied load force increases, the H_V decreases for all samples and reaches a plateau. This is referred to as the indentation size effect (ISE). This ISE behavior is attributed to grain boundaries and impurity phases in the material [20]. The improvement in hardness in the doped samples, as shown in Figure 2:10, can be attributed to improved locking of grain boundaries due to solute solution strengthening. Solute solution strengthening occurs when the dopant, in this case GO and rGO nano-carbon structures, create localized strain fields. This locks defects in the material, inhibiting their motion and increasing the material's hardness [21].

Table 2:2 : Hardness test results for GO and rGO doped samples

Sample	Control	0.1 % wt.		0.5 % wt.		1 % wt.	
		GO	rGO	GO	rGO	GO	rGO
H_O (GPa)	1.499	1.703	1.721	2.264	2.197	2.630	2.405
F_O (N)	0.021	0.067	0.021	0.013	0.087	0.137	0.161

Table 2:2 shows the true load independent hardness, H_O, and the energy dissipative portion of the load, F_O, which calculated using the graphs (F vs. d^2) was shown in Figure 2:11. F_O increases with an increase in doping concentrations of GO and rGO. The true hardness values of the sample increase with the increase in GO and rGO doping. The hardness of 0.1 % wt. doped GO and rGO samples are approximately equal. As the doping concentration increases, the hardness of the GO doped samples are greater than the rGO doped samples.

The greater increase in the hardness of GO doped samples compared to rGO doped samples can be attributed to the GO dopant creating a larger amount of strain in the sample than the rGO

dopant. This is due to the fact that rGO has a greater thermal stability compared to GO [22] [23]. Heating up GO to temperatures above 650˚C during the sintering process results in the oxygen functional groups being removed, creating thermally reduced GO (T-rGO) [9].This has a greater surface area than chemically reduced GO (C-rGO) [24].This increase in surface area of dopant inside the sample results in an increase in strain, thus allowing for better locking of defects [7] [21].

2.5 Conclusion

The results show that doping of bulk YBCO with GO and rGO increases the samples T_C up until 0.7 % wt. for both dopants. The increase in T_C for GO doped samples are greater than in rGO doped samples. This shows a direct correlation to the influence of oxygen on the T_C of YBCO from GO doping. There is also a notable decrease in the normal resistance with both dopants up to 0.7 % wt.

In GO and rGO doped samples, the weak-link effect has been significantly improved which is attributed to better pinning in the grain boundaries. The weak-link effect in rGO samples has improved more than in GO samples, possibly due to an increase in pinning sites as rGO will contain more nano-carbon than GO for the same weight.
Vickers hardness of both GO and rGO samples have increased with an increase in GO and rGO dopants. This is due to solute solution strengthening. The GO doped samples were harder than the rGO samples, with the hardest sample being the 1 % wt. GO doped sample.

The improvement in weak-links at grain boundaries and the increase in flux pinning sites, which is seen by the decrease in foot structure of the GO and the rGO doped samples, will allow for better performance in high current and magnetic levitation bulk applications.

References

[1] M. K. Wu, J. R. Asburn, C. J. Torng, P. H. Hor, R. L. Meng, L. Gao, Z. J. Huang, Y. Q. Wang and C. W. Chu, "Superconductivity at 93 K in a New Mixed-Phase Y-Ba-Cu-O Compound System at Ambient Pressure," *Physical Review Letters,* vol. 58, no. 9, pp. 908-910, 1987.

[2] A. L. L. Jarvis and T. B. Doyle, "The Influence of Ag Doping on the Superconducting Properties of Grain-boundary Weak-links in YBCO," *Applied Superconductivity,* vol. 1 and 2, no. 158, pp. 1149-1152, 1997.

[3] I.Karaca, "A Comparative Study for the Magnetic Levitaion Force in the Type-II Superconductors," *Sakarya University Journal of Science,* vol. 21, no. 6, pp. 1293-1299, 2012.

[4] S. Basaran and S. Sivrioglu, "Radial Stiffness Improvement of a Flywheel System Using Multi-surface Superconducting Levitation," *Superconductor Science and Technology,* 2017.

[5] J. Abrahamsson and H. Bernhoff, "Magnetic Bearings in Kinetic Energy Storage Systems for Vehicular Applications," *Journal of Electrical Systems,* vol. 7, no. 2, pp. 225-236, 2011.

[6] T. M. Aljohani, "The Flywheel Energy Storage System: A Conceptual Study, Design, and Applications in Modern Power Systems," *International Journal of Electrical Energy,* vol. 2, no. 2, pp. 146-153, 2012.

[7] U. Kölemen, S. Çelebi, H. Karal, A. Öztürk, U. Çevik and a. O. G. S. Nezir, "Superconducting and Vickers Hardness Properties of ZnO-added YBCO Polycrystalline Superconductors," *physica status solidi (b),* vol. 241, no. 6, pp. 274-283, 2004.

[8] Sudesh, N. Kumar, S. Das, C. Bernhard and G. D. Varma, "Effect of Graphene Oxide Doping on Superconducting Properties of Bulk MgB2," *Superconductor Science and Technology,* 2013.

[9] S. Dadras, S. Dehghani, M. Davoudiniya and S. Falahati, "Improving Superconducting Properties of YBCO High Temperature Superconductor by Graphene Oxide Doping," *Materials Chemistry and Physics,* vol. 193, pp. 496-500, 2017.

[10] S. Dadras, S. Falahati and S. Dehghani, "Effects of Graphene oxide Doping on the Structural and Superconducting Properties of $YBa_2Cu_3O_{7-x}$," *Physica C,* vol. 548, pp. 65-67, 2018.

[11] D. C. Marcano, D. V. Kosynkin, J. M. Berlin, A. Sinitskii, Z. Sun, A. Slesarev, L. B. Alemany, W. Lu and J. M. Tour, "Improved Synthesis of Graphene Oxide," *ACS NANO,* vol. 4, no. 8, p. 4806–4814, 2010.

[12] Z. Yang, Q. Q. Zheng, H. H. Qiu, J. L. LI and J. J. Y. Yang, "A Simple Method for the Reduction of Graphene Oxide by Sodium Borohydride with CaCl2 as a Catalyst," *New Carbon Materials,* vol. 30, no. 1, pp. 41- 47, 2015.

[13] A. Leenders, M. Ullrich and H. Freyhardt, "Influence of Thermal Cycling on the Mechanical Properties of VGF Melt-textured YBCO," *Physica C,* vol. 279, pp. 173-180, 1997.

[14] M. S. Eluyemi, M. A. Eleruja, A. V. Adedeji, B. Olofinjana, O. Fasakin, O. O. Akinwunmi, O. O. Ilori, A. T. Famojuro, S. A. Ayinde and E. O. B. Ajayi, "Synthesis and Characterization of Graphene

Oxide and Reduced Graphene Oxide Thin Films Deposited by Spray Pyrolysis Method," *Graphene,* vol. 5, pp. 143-145, 2016.

[15] R. Muzyka, S. Drewniak, T. Pustelny, M. Chrubasik and G. Gryglewicz, "Characterization of Graphite Oxide and Reduced Graphene Oxide Obtained from Different Graphite Precursors and Oxidized by Different Methods Using Raman Spectroscopy," *materials,* vol. 11, no. 7, 2018.

[16] P. Sreekanth, S. Pranitha, P. R. T and a. R. Philip, "White Light Z-scan Measurements of Ultrafast Optical Nonlinearity in Reduced Graphene Oxide Nanosheets in the 400–700nm Region," *Applied Physics Letters,* vol. 107, 2015.

[17] V. T. Nguyen, H. D. Le, V. C. Nguyen, T. T. T. Ngo, D. Q. Le, X. N. Nguyen and N. M. Phan, "Synthesis of Multi-layer Graphene Films on Copper Tape by Atmospheric Pressure Chemical Vapor Deposition Method," *Advances in Natural Sciences: Nanoscience and Nanotechnology,* 2013.

[18] K. Moorjani, F. J. Adrian, J. B. Boris F. Kim, T. E. Phillips, T. J. Kistenmacher, W. J. Green, E. Agostinelli, B. G. Boone and R. M. Soya, "High-Temperature Superconductivity," *Johns Hopkins APL Technical Digest,* pp. 158-159, 1990.

[19] F. R. Fickett, "Standards for Measurement of the Critical Fields of Superconductors," *Journal of Rescarch of the National Burwau of Standards,* vol. 90, no. 2, 1985.

[20] M. B. Turkoz, S. Nezir, O. Ozturk, E. Asikuzun, G. Yildirim, C. Terzioglu and A. Varilci, "Experimental and Theoretical Approaches on Mechanical Evaluation of Y123 System by Lu Addition," *J Mater Sci: Mater Electron,* vol. 24, p. 2414–2421, 2013.

[21] H. C. Ling and M. F. Yan, "Microhardness Measurements on Dopant Modified Superconducting $YBa_2Cu_3O_7$ Ceramics," *Journal of Applied Physics,* vol. 64, no. 3, pp. 1307-1311, 1988.

[22] I. Sengupta, S. Chakraborty, M. Talukdar, S. K. Pal and S. Chakrabortya, "Thermal Reduction of Graphene Oxide: How Temperature Influences Purity," *Journal of Materials Research ,* vol. 33, no. 23, pp. 4113-4122, 2018.

[23] H. Feng, R. Cheng, X. Zhao, X. Duan and J. Li, "A Low-Temperature Method to Produce Highly Reduced Graphene Oxide," *Nature Communications,* 2013.

[24] D. F. Báez, H. Pardo, I. Laborda, J. F. Marco, C. Yáñez and S. Bollo, "Reduced Graphene Oxides: Influence of the Reduction Method on the Electrocatalytic Effect towards Nucleic Acid Oxidation," *Nano materials,* vol. 7, no. 7, 2017 .

Chapter Two Summary

In this chapter we had shown that doping YBCO with GO and rGO results in an increase in T_C. This was hypothesized to be due to an increase in the oxygen content of YBCO as stated in previous studies. The maximum T_C achieved was 98 K. This piqued interest as YBCO will have a maximum T_C of 93 K at optimum oxygenation. The micro-hardness measurements showed an improvement in the hardness of GO and rGO doped samples.

To verify that doping YBCO with GO and rGO increases its oxygen content which results in an increase in T_C. We decided to measure the oxygen content of GO and rGO doped samples using iodometry which is shown in chapter 3. TEM imaging was used to characterize the doped samples.

Chapter 3

Peer-Reviewed Conference Article 1

Comparison of Graphene Oxide and Reduced Graphene Oxide Doping on YBCO for Power Applications

Mohammed Zaahid Gaffoor, Alan Leigh Lawrence Jarvis, and Solan Perumal

Published: *Southern African Universities Power Engineering Conference (2020)*

DOI: *https://doi.org/10.1109/SAUPEC/RobMech/PRASA48453.2020.9041088*

3.1 Abstract

In this research High Temperature Superconductor material (YBCO) was doped with graphene oxide (GO) and reduced graphene oxide (rGO) in 0.5 % wt. and 0.7 % wt. concentrations. Resistance versus Temperature (R vs. T) measurements were carried out in field cooling (FC) and zero field cooling (ZFC) conditions. In order to determine the critical transition temperature (T_C) and observe the effect of doping on the weak-links. The increase in T_C was greater in GO doped samples compared to rGO doped samples, this is due to the increase in oxygen content in the doped samples which was confirmed by iodometric titration. The weak-link effect was improved in both GO and rGO doped samples. The reduction of the weak-link effect infers YBCO material with a higher critical current density (J_C).

3.2 Introduction

This research is the continuation from past research titled “Effect of Graphene Oxide Doping on Bulk High Temperature Superconductors for Power Applications” which was presented at SAUPEC 2019 [1].

In previous research doping bulk high temperature superconductor (HTS) YBCO, with graphene oxide (GO) was seen to increase the critical transition temperature (T_C). This was attributed to GO doping increasing the oxygen content of YBCO. The weak-link effect was also reduced. This was attributed to improved grain connectivity and an increase in flux pinning sites [1]. The causes of weak-links and how they hinder the current carrying capability of bulk superconductors was discussed previously. Therefore reducing the weak-link effect would result in an improved J_C for bulk HTS [1]. It was also stated that an increase in T_C would allow for reduction in cost of cryogenic systems thus reducing the cost for applications and increase current carrying capability of the superconductor [1] [2].

In this research YBCO bulk HTS was doped with GO and rGO in order to compare the effects on the weak-links due to each dopant and how the reduction in oxygen content of rGO compared to GO affects the non-stoichiometric oxygen content of doped samples.

3.3 Background

In YBCO's chemical formulae ($Y_1Ba_2Cu_3O_{7-\delta}$), '7-δ' represents the oxygen coefficient of the compound [3] [4]. The delta (δ) represents the variable non-stoichiometric oxygen content. The oxygen content of YBCO determines the hole density of the material [3] [4]. Increase in oxygen content increases the hole density of the material. This is the parameter upon which superconductivity depends [3] [4]. In order for the superconducting phase to occur delta must be in the range of $0 < \delta < 0.6$ shown in Figure 3:1. During this phase YBCO has an orthorhombic crystal structure shown in Figure 3:2 [3].

This orthorhombic structure consists of two CuO_2 planes separated by an yttrium layer which contains no oxygen. Thereafter there is a Ba-O layer and a Cu-O layer on the top and bottom of the unit cell. The most important part of this structure is the one-dimensional Cu-O chains in the Cu-O layer and the ordered oxygen vacancies between them [3] [4].

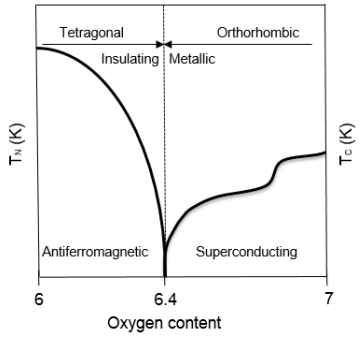

Figure 3:1 : Change in YBCO phase due to variation in oxygen content.

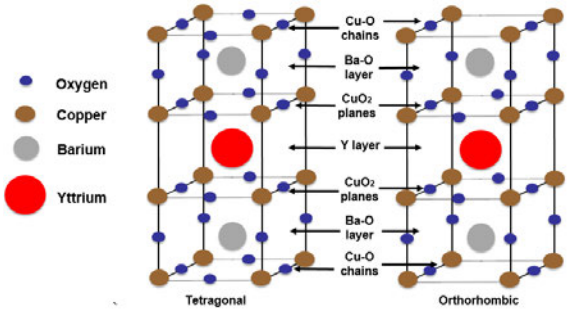

Figure 3:2 : Orthorhombic and tetragonal structure of YBCO

In the orthrhombic structure the diffusion of oxygen into the oxygen sites on the Cu-O chains allows for the variation of delta in the range of $0 < \delta < 0.6$. This variation of delta results in the variation of T_C. Increase in delta decreases the T_C and decrease in delta increases T_C seen in Figure 3:3. Further increase in delta to the region of $0.6 < \delta < 1$ results in YBCO changing to an antiferromagnetic phase in which its T_C decreases to 0 K shown in Figure 3:1. In this phase the remaining oxygen atoms occupy the sites between the Cu-O chains thus resulting in a disordered tetragonal structure shown in Figure 3:2 [3].

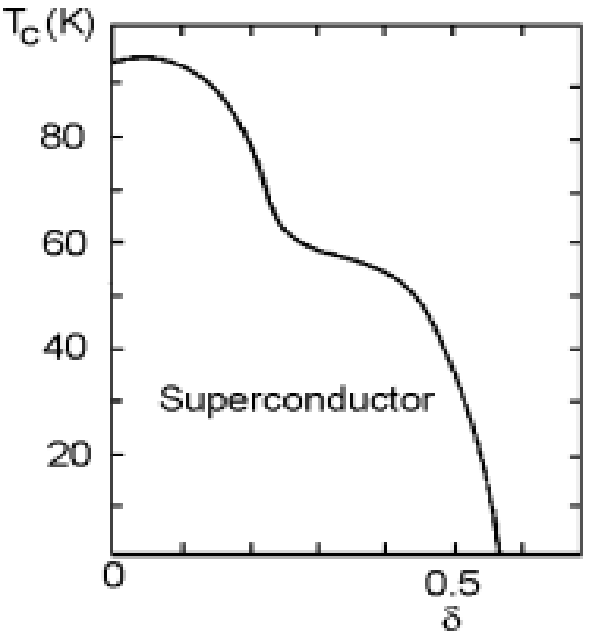

Figure 3:3 : Curve demonstrating change in T_C as a function of oxygen content [3]

Due to the relationship between the oxygen content and T_C of YBCO the determination of this parameter is important. There are both destructive and non-destructive methods to determine the oxygen content [5]

Non-destructive methods include X-ray diffraction, Auger spectroscopy, photoelectron spectroscopy, RAMAN spectrometry and electron microanalysis. Destructive methods include thermo-gravimetric methods, gas volumetric methods, voltamperometry, iodometric titration, spectrophotometric methods and coulometric methods [5]

The method of iodometric titration is part of the wet methods to determine the oxygen content. It can be carried out in a one step method which involves two consecutive titrations of one sample or two step method which involves titration of two individual samples. The two step iodometric titration is more accurate that the single step process [5].

3.4 Experimental

GO was produced using the improved Hummers method with additional potassium permanganate [6]. Thereafter, GO was reduced to form rGO using sodium borohydride ($NaBH_4$) and calcium chloride ($CaCl_2$) as a catalyst [7]. YBCO powder was doped with GO and rGO in 0.5 % wt. and 0.7 % wt. concentrations. These doped powders were pressed into pellets at a pressure of 45 MPa and sintered at 950˚C in an oxygen atmosphere for 6 hours. Four wire resistance measurements were thereafter carried out in ZFC conditions and FC conditions [1].

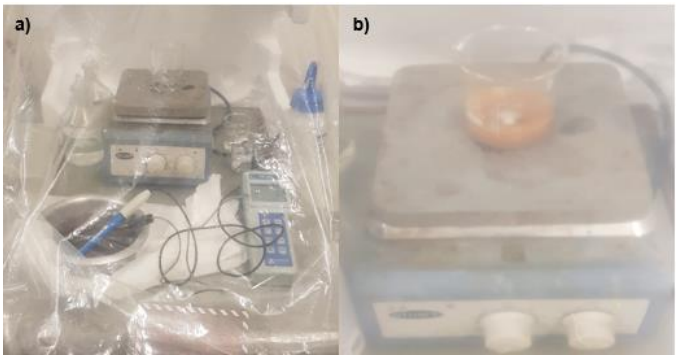

Figure 3:4 : a) Experimental setup inside glove bag and **b)** dissolving of sample inside glove bag with magnetic stirrer

Oxygen content of the GO and rGO doped samples were determined by the process of iodometry using the two step method [5]. In the first titration a nitrogen atmosphere was created using a glove bag, Figure 3:4 a), in order to prepare the solution for titration. 50 mg of YBCO sample was dissolved in 10 ml of 3 molar (M) hydrochloric acid (HCl) solution. Were molar denotes the concentration of the solution. Thereafter 1g of potassium iodide (KI) was added to the solution. This solution was then stirred with a magnetic stirrer until the sample is dissolved shown in Figure 3:4 b). The pH of the solution was adjusted to approximately 3.5 using a buffer solution which contains 3 M sodium acetate (NH_4Ac) and 3 M acetic acid (HAc) solutions. A hand held pH meter was used to take pH readings. This can be seen in Figure 3:5.

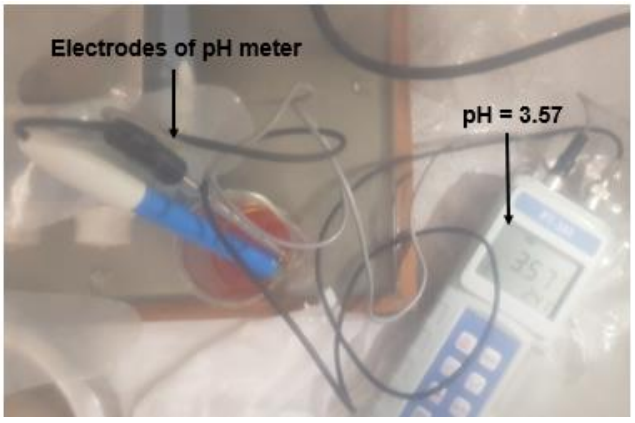

Figure 3:5 : Testing pH level of the YBCO, KI and HCl solution in a nitrogen atmosphere using a pH meter.

The resulting solution was then removed from the nitrogen atmosphere and titrated with 0.01 M sodium thiosulfate ($Na_2S_2O_3$) titrant. The colour changes of the solution during titration can be seen in Figure 3:6. Figure 3:6 a) shows the solution colour at the beginning before the titrant is added. As the titrant is added the colour changes to pail orange which can be seen in Figure 3:6 b). At this point 2 ml of 1 % starch solution was added to the solution to use as an indicator to indicate endpoint of the titration. The addition of this indicator turns the solution black which can be seen in Figure 3:6 c). Further titration of the solution turns the solution dark purple which thereafter turns to a pail purple, Figure 3:6 d) and Figure 3:6 e).

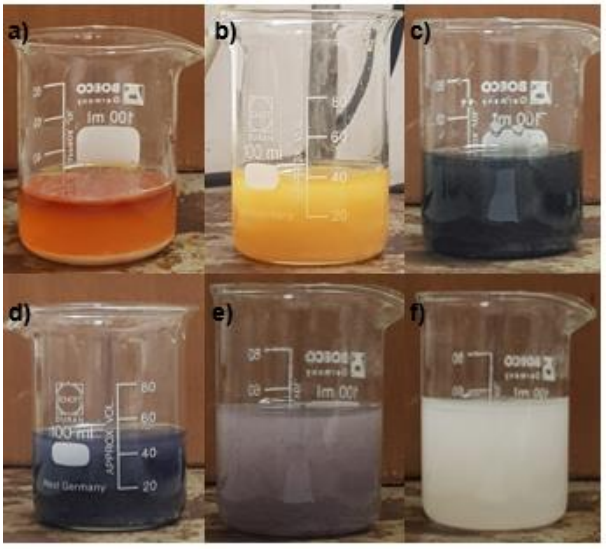

Figure 3:6 : Colour changes which occur during titration

At this point 5 ml of 20 % potassium thiocyanate (KSCN) solution was added and the solution was the titrated to starch and KSCN endpoints, which is a colourless solution shown in Figure 3:6 f). The total volume of $Na_2S_2O_3$ added is equal to V_1^{eq} in ml in equation 3.1.

$$\delta = 1.5\frac{V_2^{eq} - V_1^{eq}}{V_1^{eq}} \tag{3.1}$$

In the second titration 50 mg of the sample was dissolved in 10 ml of 3 M HCl solution using a hot water bath shown in Figure 3:7 a). This solution was then heated up for 10 minutes and stirred using a magnetic stirrer and then left to cool to room temperature, Figure 3:7 b).

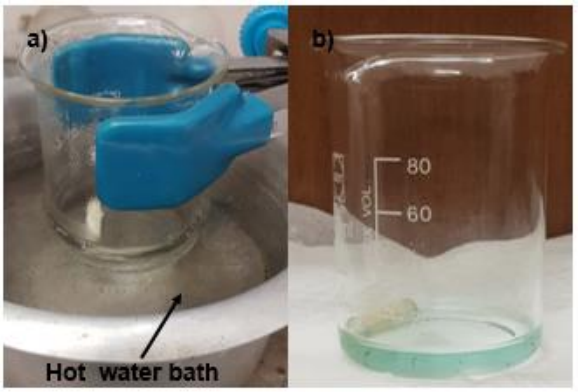

Figure 3:7 : a) dissolving of YBCO sample in HCl solution and **b)** solution after dissolving of YBCO sample

The solution was then placed into a nitrogen atmosphere and the pH was adjusted to approximately 3.5, using the appropriate amount of buffer solution. 1g of KI was thereafter added and the solution was stirred using a magnetic stirrer for 20 minutes. The resulting solution was removed from the nitrogen atmosphere and titrated with 0.01 M $Na_2S_2O_3$ solution to starch and KSCN endpoints as explained in the first titration. The total volume of $Na_2S_2O_3$ added is equal to V_1^{eq} in ml in equation 1.1.

3.5 Results and Discussion

The elemental composition of GO and rGO in Figure 3:8, which was obtained using Electron dispersive x-ray (EDX) analysis. The C/O ratio is 1.56 and 5.95 in GO and rGO respectively. This increase of the C/O ratio in the rGO sample shows that reduction has occurred [8]. This can also be seen in Figure 3:8 by the decrease in oxygen content in rGO. Trace elements Na, S, Cl, and K are impurities which occur due to chemical processes of synthesizing GO and reduction of GO to rGO they can be seen to be negligible.

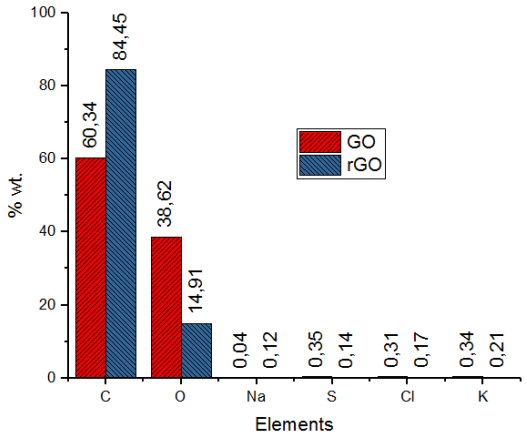

Figure 3:8 : Data from EDX showing elemental content of GO and rGO

Transmission electron microscope (TEM) images of GO and rGO can be seen in Figure 3:9 a) and Figure 3:9 b). Folded sheet structure can be seen in both images.

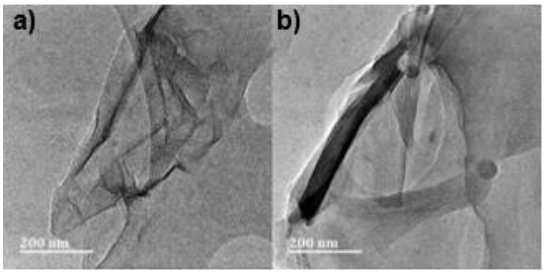

Figure 3:9 : a) TEM image of GO and **b)** TEM image of rGO

Figure 3:10 shows TEM image of the control sample after sintering. The YBCO grain structure can be seen in comparison. Figure 3:11 which shows the TEM image of a doped sample after sintering. In the doped sample the graphene sheet structures can be seen with YBCO grains spread on to them.

This could suggest that the weak-link effect is reduced due to improved grain connectivity and increase in flux pinning sites due to graphene nano-particles. This improved grain connectivity is due to graphene having a high conductivity therefore allowing for better conduction between grains which can be seen in Figure 3:12.Which shows TEM image of graphene nano-particles between YBCO grains of the sintered bulk samples.

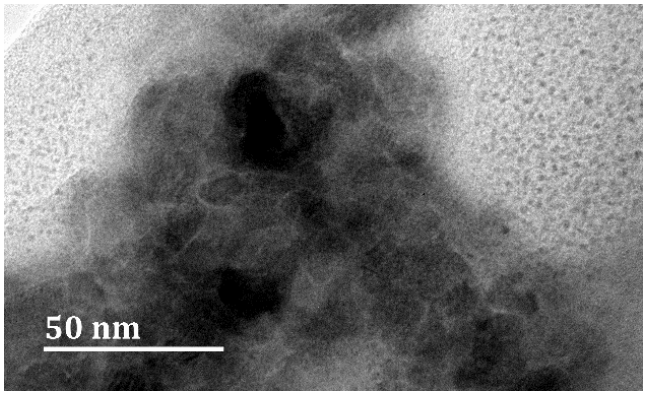

Figure 3:10 : TEM image of YBCO grains

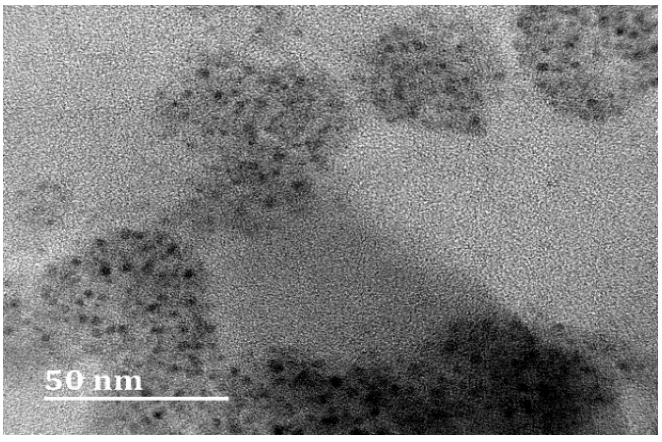

Figure 3:11 : rGO sheets with YBCO particles in doped samples

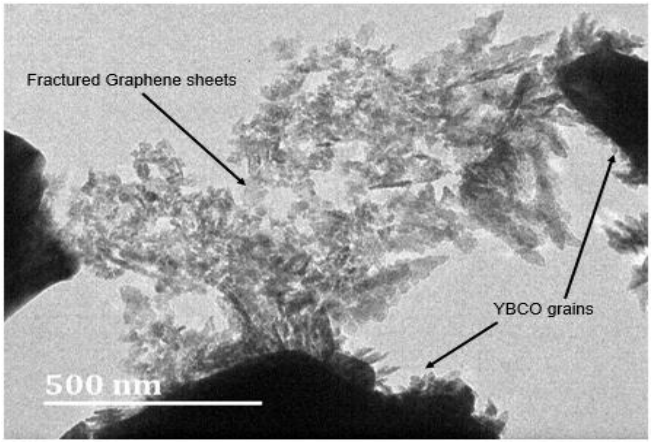

Figure 3:12 : Graphene sheets at YBCO grain boundary in doped samples

The R (T) measurements in ZFC conditions are shown in Figure 3:13. The normal resistance in GO and rGO samples have decreased. This decrease in normal resistance also confirms improved grain connectivity [1] [9]. This is due to rGO being highly conductive and GO being thermally reduced to rGO during the sintering process [1] [9].The T_C of both GO and rGO doped samples have increased, this is attributed to the GO and rGO dopant increasing the oxygen content of the superconductor [1] [4] [9]. The increase in the oxygen content in the GO doped samples is greater than in the rGO doped samples thus resulting in a greater increase in T_C in GO doped samples.

This is due to GO comprising of more oxygen than rGO which can be seen in Figure 3:8. This greater increase in oxygen content in GO doped samples than in rGO doped samples was confirmed via titration shown in Table 3:1.

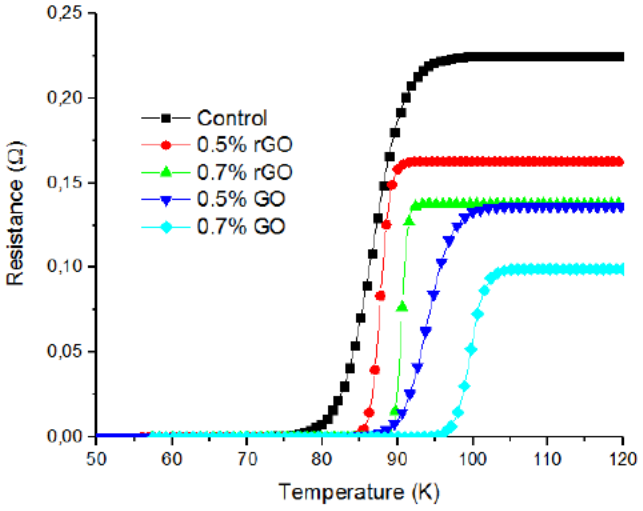

Figure 3:13 : R vs. T curves in ZFC conditions

R vs. T measurements were taken in FC conditions in a 5 mT field in order to determine the effect of doping on the weak-links at grain boundaries. The control sample can be seen to have a network of weak-links due to the increase in the foot structure which was observed in prior research [1].

Table 3:1 : Analysis of ZFC curves

	Control	**GO doped YBCO (wt.)**		**rGO doped YBCO (wt.)**	
		0.5	**0.7**	**0.5**	**0.7**
Tc_{mid}(K)	84	92	98	88	91
Resistance at T=120 K (Ω)	0.255	0.136	0.099	0.163	0.138
Oxygen content	6.67	6.75	6.91	6.69	6.72

Comparing GO and rGO doped samples in Figure 3:14, it can be seen that as rGO and GO doping concentration increases, the weak-link effect reduces. This is observed by the reduction in the foot structure of the FC curves. This improvement is attributed to improved grain boundary connectivity due to graphene sheets at the grain boundaries and an increase in flux pining sites due to graphene nano- particles which can be seen in Figure 3:11 and Figure 3:12 [1].

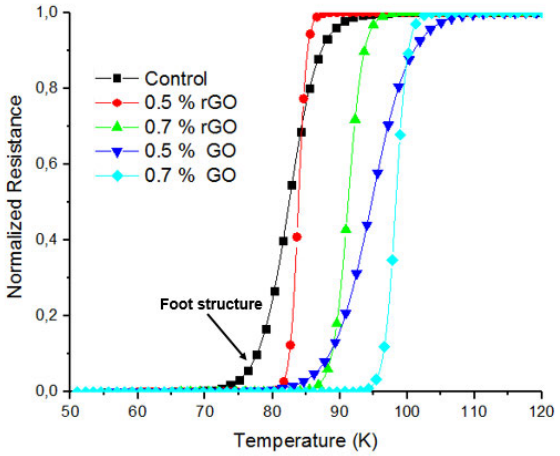

Figure 3:14 : R vs. T curves in FC (5 mT) conditions

3.6 Conclusion

The increase in T_C of GO doped samples is greater than in rGO doped samples and is attributed to GO having a greater oxygen content than rGO therefore allowing for the stoichiometric oxygen content of GO doped samples to be higher than rGO samples.

The weak-link effect in GO and rGO samples has improved and is explained due to improved grain connectivity because of the high conductivity of graphene, and increase in flux pinning sites due to graphene nano- graphene particles. This will allow for larger transport currents in YBCO based superconducting conductors.

References

[1] M. Z. Gaffoor, A. L. L. Jarvis, J. C. Archer and S. Perumal, "Effect of Graphene Oxide Doping on Bulk High Temperature Superconductors For Power Applications," in *Southern African Universities Power Engineering Conference*, Bloemfontein, 2019.

[2] J. MacManus-Driscoll and S. Wimbush, "Future Directions for Cuprate Conductors," *IEEE Transactions on Applied Superconductivity*, vol. 21, no. 3, pp. 2495-2500, 2011.

[3] Y. Bruynseraede, J. Vanacken, B. Wuyts, C. V. Haesendonck, J. Locquet and I. K. Schuller, "Oxygen Disorder Effects in High Tc Superconductors," *Physica Scripta*, vol. Vol. T29, pp. 100-105, 1989.

[4] R. Sharma, "Springer series in material Science," in *Superconductivity Basics and Applications to Magnets*, pp. 78-80.

[5] S. Georgieva, T. Nedeltcheva and A. Stoyanova-Ivanova, "Development of the Titrimetric and Spectrophotometric Methods for Determination of the Oxygen Content in Superconducting Cuprates," *American Chemical Science Journal*, vol. 13, no. 1, 2016.

[6] D. C. Marcano, D. V. Kosynkin, J. M. Berlin, A. Sinitskii, Z. Sun, A. Slesarev, L. B. Alemany, W. Lu and J. M. Tour, "Improved Synthesis of Graphene Oxide," *ACS Nano*, vol. 4, no. 8, p. 4806–4814, 2010.

[7] Z. Yang, Q. Q. Zheng, H. H. Qiu, J. L. LI and J. J. Y. Yang, "A Simple Method for the Reduction of Graphene Oxide by Sodium Borohydride with $CaCl_2$ as a Catalyst," *New Carbon Materials*, vol. 30, no. 1, pp. 41- 47, 2015.

[8] J. G. S. Moo, B. Khezri, R. D. Webster and M. Pumera, "Graphene Oxides Prepared by Hummers', Hofmann's, and Staudenmaier's Methods: Dramatic Influences on Heavy-Metal-Ion Adsorption," *CHEMPHYSCHEM*, pp. 2922-2929, 2014.

[9] S. Dadras, S. Falahati and S. Dehghani, "Effects of Graphene oxide Doping on the Structural and Superconducting Properties of $Y_1Ba_2Cu_3O_{7-x}$," *Physica C*, vol. 548, pp. 65-67, 2018.

Chapter Three Summary

In this chapter it was confirmed that the increase in T_C for YBCO doped GO and rGO samples is a result of the dopants increasing the oxygen content of YBCO. It also showed that the increase in the oxygen content can only explain the increase in T_C up to 93 K. Therefore, the explanation provided by previous studies were not accurate. Thus, a new explanation for this increase in T_C above 93 K was researched in chapter 5.

In chapter 4 the mechanical and structural parameters of the YBCO doped GO and rGO samples were studied. This was researched as the poor mechanical parameters of bulk material prevents its use in numerous applications.

Chapter 4

Peer-Reviewed Journal Article 2

Mechanical and Structural Properties of Graphene Oxide and Reduced Graphene Oxide doped YBCO

Mohammed Zaahid Gaffoor, Alan Lawrence Leigh Jarvis and Andrew Swanson

Published: *IEEE Transactions on Applied Superconductivity (2023)*

DOI: *http://dx.doi.org/10.1109/TASC.2023.3253464*

4.1 Abstract

YBCO ($Y_1Ba_2Cu_3O_{7-\delta}$) was doped with graphene oxide (GO) and reduced graphene oxide (rGO) in the following percentage weight concentrations: 0.1, 0.5 and 1 % wt. . Lattice parameters, crystallite size, orthorhombicity and lattice strain were calculated using XRD analysis. The porosity of samples decreased by a maximum of 29 % and 17 % for GO and rGO doped samples respectively. Microhardness measurements were conducted using the Vickers hardness method at loads in the range of 0.245 - 2.940 N. These micro hardness measurements were used to calculate the Vickers hardness (H_V), elastic modulus (E), yield strength (Y), fracture toughness (K_{IC}) and brittleness index (B) of the material. H_V was greater in GO doped samples than in rGO doped samples. E increased by 63.94 % for rGO and 85.52 % for GO doped samples. Y increased by 63.80 % for rGO and 85.40 % for GO doped samples. B decreased by 48.11 % for rGO and 43.78 % for GO doped samples. There was an increase in K_{IC} for both GO and rGO samples. The indentation size effect (ISE) was observed during micro-hardness measurements. This ISE behaviour was analyzed using Meyers Law, PSR model, elastic/plastic deformation model and Hays Kendall model. The results showed that the Hay Kendall approach best described the ISE behaviour of the samples.

4.2 Introduction

YBCO is a high temperature superconductor (HTS) which was discovered in 1987 with a critical transition (T_C) of 93 K [1]. This was of importance as it was the first HTS with a T_C above the boiling point of liquid nitrogen (77 K) [2] [3]. Therefore, making it more cost effective to use in applications as liquid nitrogen is cheaper than liquid helium.

This cost effectiveness in combination with its remarkable properties such as high current carrying capacity, ability to trap large magnetic fields [4] [5], less toxic compared to Tl and Hg based HTSs, simplicity to produce in large quantities and easily available precursor materials [3] [6], make YBCO an attractive candidate for a range of industrial applications. Examples of these applications are AC/DC transmission lines, high field magnets, motors and generators and magnetic levitation devices [2].

Nevertheless, one of the greatest downfalls of YBCO in bulk form, is its poor mechanical properties which reduces the range of applications in which it can be used [7] [8]. A considerable amount of research has been carried out to improve YBCO's mechanical and structural properties. Methods used to improve these properties are doping and alloying [5] [6] [8] [9].

Research conducted in doping YBCO with graphene oxide (GO) and reduced graphene oxide (rGO) has shown improvement in the superconducting properties of the material, including an increase in T_C [10-14]. This increase is hypothesized to be due to an increase in non-stochiometric oxygen [14] or possible Mn impurities found in GO [10]. The critical current density (J_C) improved with GO and rGO doping [12] [15]. This was attributed to the improvement in grain connectivity [12] and an increase in flux pinning centers [15].

There is limited research to be found regarding the mechanical properties of GO and rGO doped YBCO [9] [12]. These studies found the elastic moduli such as rigidity modulus, longitudinal modulus, Youngs Modulus and Poisson's ratio im-proved as well as the microhardness was enhanced [12]. These parameters improved with an increase in GO and rGO doping concentration. The improvement of these mechanical parameters has been attributed to a decrease in the porosity of the sample which results in improved grain connectivity [9] [12].

Doping of YBCO with GO and rGO has shown improvements of the superconducting and mechanical properties of doped samples. Therefore, in this research we compare the effect that these GO and rGO dopants have on the mechanical and structural properties of YBCO superconductor. In our previously published research microhardness measurements were conducted and the Vickers hardness was calculated [13]. In this extension, these microhardness measurements are used to calculate the elastic modulus (E), yield strength (Y), fracture

toughness (K_{IC}) and brittleness index (B). Thereafter these measurements were modeled using Meyers law, proportional sample resistance (PSR) model, elastic/plastic deformation (EPD) model and the Hays-Kendall (HK) model to determine which model best describes the H_V property of the doped GO and rGO samples.

4.3 Experimental

GO was produced using the Hummers method with additional potassium permanganate [16]. The reagents used during the GO production process are natural flake graphite (CY3222) which was purchased from RMC minerals, sulphuric acid (purity : 98 %) and potassium permanganate (purity : 99 %) which are purchased from Radchem Pty Ltd and sodium nitrate (purity: 98.5 %) which was purchased from Unilab.

rGO was produced via chemical reduction of GO using sodium borohydride (purity: 99.8 %) and calcium chloride (purity: 99.5 %) as a catalyst [17] which was purchased from Radchem Pty Ltd.

In previous research GO and rGO were characterized using FTIR, RAMAN and TEM [13]. YBCO used in this research was purchased from Superconductor Inc. and has a purity of 99.9 %. YBCO pellets were doped with the following GO and rGO % wt. concentrations: 0.1, 0.5 and 1.0. These doping concentrations were chosen as it has been observed from past research that the optimum T_C of GO and rGO doped YBCO occurs in the range of 0 – 1 %wt. GO or rGO doping concentration [9] [11] [12] [14]. Microhardness measurements were conducted at a temperature of 297 K using the HM-210 manual main unit, single indenter shaft Vickers hardness testing machine. The following load forces (F) were applied with a load contact time of 10 s: 0.245 N, 0.491 N, 0.981 N, 1.962 N, 2.943 N [13]. To improve the accuracy of the Vickers hard-ness measurement, seven measurements were conducted at each load and thereafter averaged to obtain a single data point.

In the present research microhardness data was used to calculate H_V, E, Y, K_{IC} and B. These mechanical properties are important for industrial applications of superconductors. E is the affinity of the material to deform elastically under a force. [18]. Y is known as a transition point between elastic and plastic deformation occurring [18]. K_{IC} is the ability of the material to resist fracture and crack propagation. K_{IC} is one of the most important factors used when selecting materials for industrial applications [18]. B is the ratio of Vickers hardness and fracture toughness. Thereafter the microhardness measurements were analyzed using Meyer's Law, EPD, PSR and HK models to determine which model best describes the microhardness of the GO and rGO doped samples. The goodness of fit parameter, which is the linear regression coefficient (LRC) was determined for all model fitting. The closer to unity the LRC is the better the fit. Thus, more accurate fitting parameters [19].

X-ray Diffraction (XRD) was carried out for phase confirmation and to perform structural analysis of the doped samples. The samples were analyzed using a PANalytical X'Pert Pro powder diffractometer in θ-θ configuration with an X'Celerator detector, variable divergence and fixed receiving slits with Fe filtered Co-Kα radiation. The wavelength (λ) of radiation used

is 1.789 Å. The x-ray diffractograms in con-junction with XRD analysis software Material Analysis Using Diffraction (MAUD) [20] were used to calculate structural parameters such as cell parameters (a, b, c), orthorhombicity, crystallite size, average oxygen content, Cu(1) (Cu^{2+}) and Cu(2)(Cu^{3+}) atomic site occupancy and lattice strain obtained using the Williamson-Hall method [11].

The average oxygen content of the samples was also calculated by the process of iodometry [21] [22]. This procedure has been published in detail previously [22] [23]. In order to improve accuracy each sample was titrated three times and the results were averaged. This method is reliable in range of $0 \leq \delta \leq 0.5$ [21]. The error of the experimental evaluation of the oxygen content is below 2 % [22] and measurements have a resolution of 0.02. This resolution is due to experimental apparatus used. The following reagents were used during this iodometric process: sodium thiosulphate (purity: 99.9 %) and starch soluble (extra pure) purchased from Thomas baker, potassium thiocyanate (purity: 98.5 %) purchased from Merch Life Science, acetic acid (purity: 60.05 %) which was purchased from Associated Chemical Enterprises, ammonium acetate (purity: 97 %) which was purchased from Unilab, potassium iodide (purity: 99.5 %) which was purchased from Radchem Pty Ltd..

The percentage porosity (P) of samples were calculated using equation 4.1 [9]:

$$P = (1 - \frac{Bulk\ Density\ (\rho)}{Xray - Density\ (\rho_x)}) \times 100 \tag{4.1}$$

Xray-density (ρ_x) is calculated using equation 4.2 [9],

$$\rho_x = \frac{nM}{NV_{cell}}, \tag{4.2}$$

with n being the number of molecules per unit cell, M is the molecular mass of sample in grams, V_{cel}l is the volume of the unit cell and N is Avogadro's number [9]. V_{cell} can be calculated using the equation 4.3:

$$V_{cell} = a \times b \times c, \tag{4.3}$$

were a, b and c are the lattice parameters calculated using the XRD spectrum. The bulk density (ρ) of the material is obtained using equation 4.4:

$$\rho = \frac{M}{V_{bulk}}, \tag{4.4}$$

M is defined as the mass of the sample and V_{bulk} is defined as the bulk volume of the sample [12].

4.4 Results and Discussion

4.4.1 X-ray Diffraction Analysis

Diffraction spectrums for control, GO and rGO doped samples are seen in Figure 4:1. They display the following peaks: (003), (103), (104), (113), (200), (123) and (220) which are characteristic of the Y123 phase with perovskite structure [11] [24].

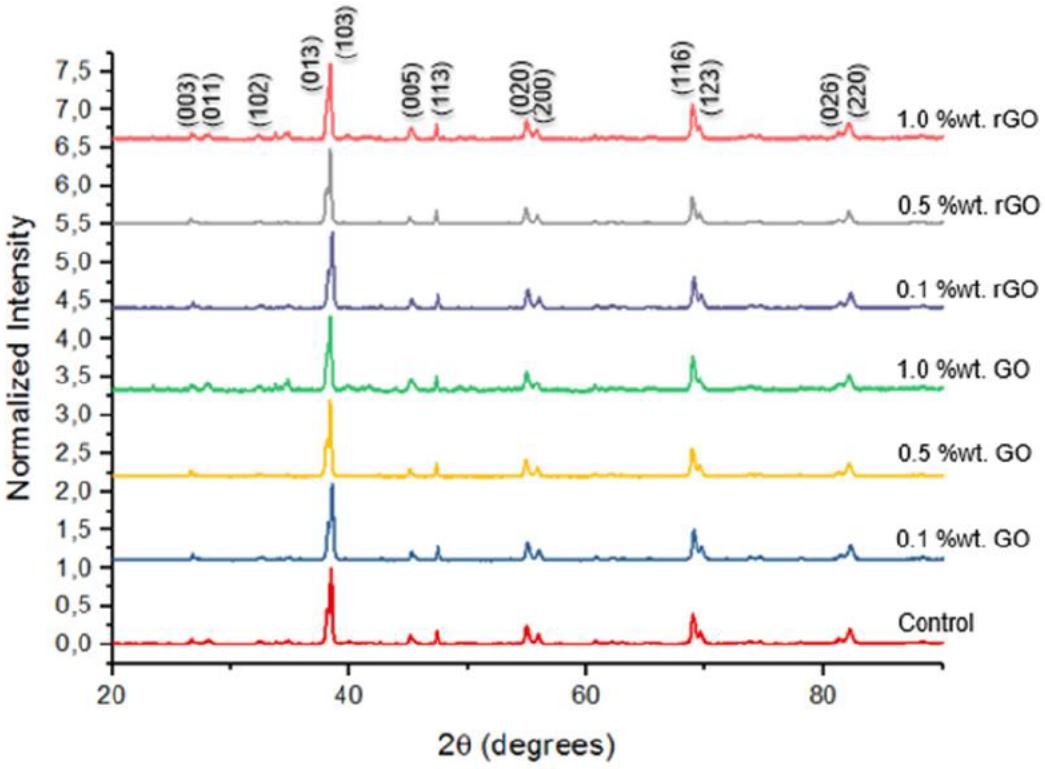

Figure 4:1: XRD spectrum of GO and rGO doped samples.

Table 4:1: Lattice strain, oxygen content, crystallite size, lattice parameters and orthorhombicity of GO and rGO samples.

Sample		Lattice Strain	a(Å)	b(Å)	c(Å)	Orthorhombicity	Crystallite size(nm)
Control		0.00175± 6.2E-5	3.82563±1.16E-5	3.88709±1.81E-5	11.67142±7.00E-5	0.00797±5.18E-6	65.187±2.91
	0.1	0.00127± 5.5E-5	3.82396±8.43E-4	3.88724±1.32E-5	11.66997±5.09E-5	0.00820±1.05E-5	46.401±2.62
GO	0.5	0.00112± 3.7E-5	3.82331±7.54E-5	3.88777±1.16E-5	11.66400±4.43E-5	0.00836±1.20E-5	44.725±1.01
	1.0	0.00054± 7.6E-5	3.82295±1.00E-5	3.88859±1.69E-5	11.66614±6.65E-5	0.00851±1.56E-6	27.476±2.35
	0.1	0.00134± 1.1E-5	3.82246±5.22E-5	3.88711±8.17E-5	11.67416±2.78E-3	0.00839±2.16E-5	40.970±2.24
rGO	0.5	0.00125± 8.2E-5	3.82247±8.23E-5	3.88753±1.25E-5	11.67075±4.77E-5	0.00844±1.39E-5	39.367±1.97
	1.0	0.00073± 1.0E-5	3.82203±2.23E-5	3.88820±3.19E-5	11.66860±1.06E-3	0.00858±4.91E-6	30.610±1.12

Rietfield refinement was carried out using crystallography analysis software called, MAUD [20] to determine the lattice parameters a, b and c which can be seen in Table 4:1. In GO and rGO doped samples an increase in the b-axis is observed with an increase in GO and rGO

doping. This increment can be related to an increase in the non-stochiometric oxygen content in the copper oxide chain [24] shown in Table 4:2.

The oxygen content was calculated using XRD and iodometry. In the iodometry procedure the oxidation state of the Cu ions is important. A change in the oxidation state of Cu ions will induce error into the iodometric procedure. Therefore, the atomic site occupancy of the Cu (1)

Table 4:2: Average oxygen content, Cu(1) and Cu(2) atomic site occupancies of control, GO and rGO samples

Sample	Oxygen content (7-δ)		Site occupancy	
	(XRD)	(Iodometry)	Cu (1)	Cu (2)
Control	6.67 ± 0.02	6.71 ± (≤ 0.13)	1.00	1.00
0.1 GO	6.79 ± 0.03	6.76 ± (≤ 0.14)	1.00	1.00
0.5 GO	6.85 ± 0.02	6.81 ± (≤ 0.14)	1.00	1.00
1.0 GO	6.95 ± 0.03	6.98 ± (≤ 0.14)	1.00	1.00
0.1 rGO	6.74 ± 0.03	6.71 ± (≤ 0.13)	1.00	1.00
0.5 rGO	6.80 ± 0.01	6.78 ± (≤ 0.14)	1.00	1.00
1.0 rGO	6.91 ± 0.03	6.88 ± (≤ 0.14)	1.00	1.00

and Cu (2) sites are calculated and shown in Table 4:2. There are no changes in the site occupancies. Therefore, GO and rGO does not affect the oxidation state of the Cu ions or enter the Cu atomic sites [11]. This allows for accurate iodometric measurement. The oxygen content results from the XRD and iodometry validate each other. The largest variance between the measurement methods is 0.4 %. This increase is greater in GO doped samples than in rGO doped samples. Since GO contains more oxygen functional groups than rGO which in turn results in GO samples having a higher oxygen content which can be seen in Table 4:2. Due to this increase in oxygen content we can assume that we have a larger volume fraction of the sample in the superconducting phase [12]. To verify this the orthorhombicity of the sample was calculated using equation 4.5,

$$Orthorhombicity = \frac{b - a}{b + a}, \tag{4.5}$$

which can be seen in Table 4:1. Orthorhombicity increases in both GO and rGO doped samples. This is a result of an increase in non-stochiometric oxygen content as well as enhancement in phase purity [24]. J_C can be enhanced by increasing the orthorhombicity of bulk YBCO [24]. Thus, increasing orthorhombicity will result in an increase in J_C.

$$\beta_{hkl}\cos\theta = \frac{K\lambda}{D} + 4\varepsilon\sin\theta, \tag{4.6}$$

Lattice strain (ε) was calculated by the Williamson-Hall method, using equation 4.6, where β_{hkl} is the full width half maximum (FWHM) of diffraction peaks, K is the dimensionless shape factor, which is ap-proximately 0.9, D is the crystallite size, θ is the angle of the diffraction

peak and λ is the x-ray wavelength. The graph of $\beta_{hkl}\cos\theta$ vs. $4\varepsilon\sin\theta$ was plotted and fitted with a linear best fit line. The slope and the y-int of these best fit lines are equivalent to the ε and D of the sample [11].

ε decreased in both GO and rGO samples. This can be attributed to reduction in the dislocation movement between superconducting grains [12]. Due to graphene sheets occupying intergranular spaces. These graphene sheets between grains will also improve grain boundary connectivity and reduce the porosity between grains [12]. The crystallite size is seen to decrease in both GO and rGO samples. These values can be seen in Table 4:1. This reduction in crystallite size is a large contributing factor in improving the hardness of the doped samples seen in Figure 4:2. The decrease in the crystallite size means that there are more grain boundaries [5]. These grain boundaries hinder the motion of dislocations, therefore trapping the defects in a localized area of the material which results in an improvement in hardness [25].

4.4.2 Microhardness and Modeling

H_V was calculated using equation 4.7. F is the applied load force and d is the length of the diagonals of the diamond shape indentation on the surface of the sample [6] [7] [13].

$$H_V = 1854.4\frac{F}{d^2} \tag{4.7}$$

The values for H_V can be seen in Table 4:3 and Figure 4:2 shows the plot of F vs. H_V. The error bars in Figure 4:2 represent the multiple measurements taken at each point. The values for H_V decrease with an increasing applied load force until a plateau region is reached. In this plateau region an increase in F results in a constant H_V. This behaviour is known as indentation size effect (ISE) [7] [24]. The ISE behaviour is a result of the penetration depth of the indenter. At smaller loads the indenter penetrates the surface layers therefore the surface characteristics are dominant. At larger loads the characteristics of the inner layers are dominant as the indenter penetrates the inner layers thus a saturation is reached which can be seen in the form of the plateau region [24]. The hardness values are seen to increase with an increase in GO and rGO doping. This improvement in H_V can be attributed to an enhancement in grain connectivity [24], reduction in porosity between the grains [18] [24] and hindering the motion of crack propagation between grains [26]. These enhancements are due to GO and rGO sheets located at grain boundaries [24]. The increase in H_V is greater in GO doped samples than in rGO doped samples. This could be attributed to higher oxygen levels in GO samples than in rGO samples, seen in Table 4:2. This increased amount of oxygen allows for enhanced grain boundary connectivity [24].

Table 4:3 : Calculated load dependent H_V, E, Y and K_{IC} for control, GO and rGO doped samples.

Sample	Load (N)	H_v (GPa)	B ($m^{\frac{1}{2}}$)	E (GPa)	Y (GPa)	K_{ic} ($Pa/m^{\frac{1}{2}}$)
Control	0.2	1.89 ± 7.00E-2	0.00207 ± 3.51E-4	154.48 ± 5.73	0.63 ± 2.33E-2	909.94 ± 174.22
	0.5	1.58 ± 8.00E-2	0.00189 ± 4.26E-4	129.11 ± 6.55	0.53 ± 2.67E-2	831.90 ± 187.04
	1.0	1.50 ± 3.00E-2	0.00185 ± 2.56E-4	123.13 ± 2.46	0.50 ± 1.00E-2	812.38 ± 112.58
	2.0	1.50 ± 2.00E-2	0.00185 ± 2.13E-4	122.89 ± 1.64	0.50 ± 6.67E-3	811.58 ± 93.73
	2.9	1.5 ± 1.00E-2	0.00185 ± 1.32E-4	122.88 ± 0.82	0.50 ± 3.33E-3	811.58 ± 57.82
0.1 rGO	0.2	2.10 ± 8.88E-2	0.00231±4.47E-4	172.29 ± 7.28	0.70 ± 2.96E-2	911.29 ± 198.64
	0.5	1.77 ± 8.37E-2	0.00212±4.33E-4	144.94 ± 6.86	0.59 ± 2.79E-2	835.84 ± 192.28
	1.0	1.73 ± 4.32E-2	0.00209±2.85E-4	141.90 ± 3.54	0.58 ± 1.44E-2	827.01 ± 126.40
	2.0	1.73 ± 1.32E-2	0.00209±1.72E-4	141.87 ± 1.08	0.58 ± 4.38E-3	826.92 ± 76.21
	2.9	1.73 ± 2.04E-2	0.00209±2.11E-4	141.87 ± 1.67	0.58 ± 6.78E-3	826.92 ± 93.84
0.5 rGO	0.2	3.38 ± 14.06E-2	0.00154 ± 3.12E-4	277.35 ± 11.52	1.13 ± 4.69E-2	2204.34 ± 448.62
	0.5	2.91 ± 18.15E-2	0.00142 ± 3.40E-4	238.66 ± 14.88	0.97 ± 6.05E-2	2044.82 ± 488.15
	1.0	2.36 ± 9.85E-2	0.00128 ± 2.30E-4	193.47 ± 8.07	0.79 ± 3.28E-2	1841.09 ± 330.93
	2.0	2.24 ± 9.84E-2	0.00125 ± 2.62E-4	183.38 ± 8.07	0.75 ± 3.28E-2	1792.45 ± 375.53
	2.9	2.24 ± 7.15E-2	0.00125 ± 2.17E-4	183.21 ± 5.86	0.75 ± 2.38E-2	1791.60 ± 311.34
1.0 rGO	0.2	5.32 ± 9.08E-2	0.00142±1.82E-4	436.39 ± 7.44	1.78 ± 3.03E-2	3754.40 ± 481.36
	0.5	3.97 ± 7.57E-2	0.00122±1.63E-4	325.29 ± 6.20	1.32 ± 2.52E-2	3241.41 ± 432.58
	1.0	2.88 ± 5.38E-2	0.00104±1.43E-4	235.76 ± 4.41	0.96 ± 1.79E-2	2759.56 ± 377.41
	2.0	2.49 ± 7.07E-2	0.00097±1.45E-4	203.92 ± 5.79	0.83 ± 2.36E-2	2566.46 ± 384.98
	2.9	2.46 ± 7.40E-2	0.00096±1.59E-4	201.46 ± 6.07	0.82 ± 2.47E-2	2550.91 ± 420.36
0.1 GO	0.2	2.47 ± 8.00E-2	0.00151±2.72E-4	202.48 ± 6.56	0.82 ± 2.67E-2	1634.87 ± 294.15
	0.5	2.13 ± 6.00E-2	0.00140±2.30E-4	174.72 ± 4.92	0.71 ± 2.00E-2	1518.64 ± 249.35
	1.0	1.84 ± 11.50E-2	0.00130±3.09E-4	151.00 ± 9.43	0.61 ± 3.83E-2	1411.78 ± 334.80
	2.0	1.73 ± 2.00E-2	0.00126±1.33E-4	141.61 ± 1.64	0.58 ± 6.67E-3	1367.22 ± 143.80
	2.9	1.72 ± 1.50E-2	0.00126±1.18E-4	140.75 ± 1.23	0.57 ± 5.00E-3	1363.04 ± 127.33
0.5 GO	0.2	3.47 ± 6.45E-2	0.00154±2.05E-4	284.56 ± 5.29	1.16 ± 2.15E-2	2253.12 ± 299.38
	0.5	3.01 ± 5.50E-2	0.00143±1.94E-4	246.28 ± 4.51	1.00 ± 1.83E-2	2096.11 ± 283.54
	1.0	2.56 ± 3.55E-2	0.00132±1.49E-4	210.19 ± 2.91	0.86 ± 1.18E-2	1936.43 ± 217.79
	2.0	2.36 ± 4.97E-2	0.00126±1.83E-4	193.09 ± 4.07	0.79 ± 1.66E-2	1856.01 ± 267.83
	2.9	2.33 ± 6.75E-2	0.00126±1.93E-4	190.99 ± 5.53	0.78 ± 2.25E-2	1845.87 ± 282.44
1.0 GO	0.2	5.28 ± 4.40E-2	0.00145±1.19E-4	433.11 ± 3.61	1.76 ± 1.47E-2	3674.84 ± 323.44
	0.5	3.97 ±11.65E-2	0.00125±2.07E-4	325.44 ± 9.55	1.32 ± 3.88E-2	3185.45 ± 562.64
	1.0	3.05 ±9.17E-2	0.00109±1.84E-4	249.92 ± 7.52	1.02 ± 3.06E-2	2791.51 ± 499.37
	2.0	2.79 ±5.65E-2	0.00105±1.43E-4	229.00 ± 4.63	0.93 ± 1.88E-2	2672.14 ± 388.06
	2.9	2.78 ±6.01E-2	0.00104±1.48E-4	227.94 ± 4.93	0.93 ± 2.00E-3	2665.90 ± 402.13

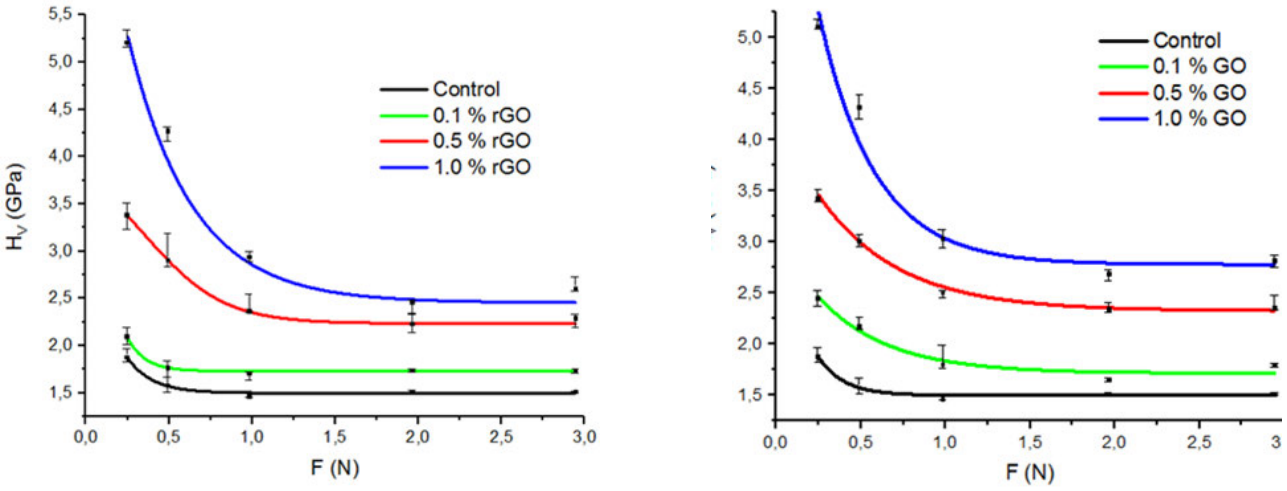

Figure 4:2: F vs. H_V for rGO doped samples

The parameters E, Y, K_{IC} and B, are calculated using equation 4.8 - equation 4.11. These values are load dependent [27] and are shown in Table 4:3.

$$E = 81.9635H_V \tag{4.8}$$

$$Y \approx \frac{H_V}{3} \tag{4.9}$$

$$K_{IC} = \sqrt{2E\gamma} \tag{4.10}$$

$$B = \frac{H_V}{K_{IC}} \tag{4.11}$$

The mechanical properties observed in Table 4:3 were most enhanced in the 1.0 %wt. doped GO and rGO samples. E increased by 63.94 ± 5 % for rGO and 85.52 ± 4 % for GO doped samples. Y increased by 63.80 ± 5 % for rGO and 85.40 ± 4 % for GO doped samples. This is due to GO and rGO dopants filling the voids and pores in the material. Thus, hindering the dislocation motion between grains, which results in the reduction in strain in the superconducting matrix. Therefore, enhancing elastic parameters [9]. This reduction in strain can be seen by the decrease in ε shown Table 4:1. K_{IC} increased by 214.32 ± 50 % for rGO and 228.49 ± 49 % for GO samples. There is a significant increment in fracture toughness of more than double the control samples original value for both GO and rGO doped samples. This improves the materials resistance to fracture or crack propagation. This improvement in facture toughness makes the doped YBCO material very desirable for industrial applications [18] [28]. B decreased by 48.11 ± 9 % for rGO and 43.78 ± 8 % for GO doped samples. The reduction in B is of significance as one of the biggest problems for polycrystalline superconductors is brittleness [6] [18]. This enhancement in B and K_{IC} can also be attributed to reduction in porosity and enhancement in grain connectivity [5].

Table 4:4: X-ray density, bulk density and percentage porosity.

Sample	Bulk Density (g/cm^3)	X-ray density (g/cm^3)	Porosity (*P*) (%)
Control	3.181	6.382	50.145
0.1 rGO	3.505	6.386	45.095
0.5 rGO	5.057	6.397	20.945
1.0 rGO	5.452	6.415	14.997
0.1 GO	4.031	6.393	36.951
0.5 GO	4.792	6.404	25.184
1.0 GO	5.881	6.430	8.531

The evaluation of the mechanical parameters B, K_{IC}, Y and E has lead to the deduction that the porosity of the GO and rGO doped samples have decreased for these enhancements to occur. This deduction is validated with the P which can be seen in Table 4:4. An increase in GO or rGO doping results in a decrease in porosity. The porosity of GO doped samples decreased by 29 % and rGO doped samples decreased by 17 %.

4.4.3 Analysis According to Meyers Law

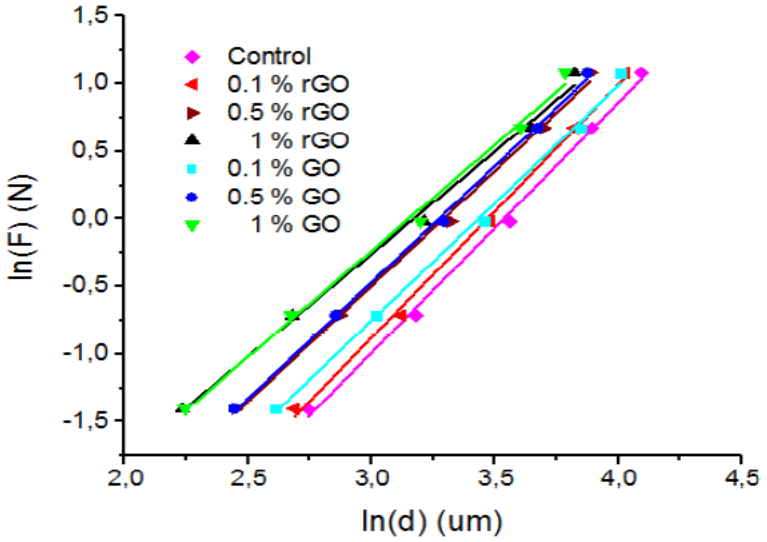

Figure 4:3: Ln F vs. Ln d for GO and rGO doped samples according to Meyers law.

Equation 4.12 shows the relationship between F and the indentation size d according to Meyers Law [29]. Were A_1 is the proportionality constant that represents the load needed for indentation to occur [29] and n which is known as Meyers number describes the extent of the ISE behavior of the sample [7]. When $n < 2$ the material obeys the ISE behaviour, if $n > 2$ the material obeys the reverse indentation size effect (RISE) behaviour and if $n = 2$ then kicks law is valid which means that the hardness is independent of the applied load force [7].

$$F = A_1 d^n \tag{4.12}$$

Figure 4:3 shows the graph of ln (F) vs. ln (d) for all samples. The slope of the graph gives the n, and the y-intercept gives A_1 [7]. These values can be seen in Table 4:5 along with the goodness of fit parameter LRC. It is observed that n for all samples is less than 2 therefore showing

Table 4:5: Best fit experimental data according to meyer's law

Sample	n	$\ln A_1$ (GPa)	LRC
Control	1.85 ± 6.04E-2	-6.54 ± 0.02	0.99575
0.1 rGO	1.87 ± 5.52E-2	-6.50 ± 0.09	0.99654
0.5 rGO	1.71 ± 4.98E-2	-5.62 ± 0.06	0.99826
1.0 rGO	1.52 ± 6.02E-2	-4.81 ± 0.19	0.99373
0.1 GO	1.74 ± 5.56E-2	-5.97 ± 0.19	0.99593
0.5 GO	1.72 ± 3.59E-2	-5.63 ± 0.12	0.99826
1.0 GO	1.57 ± 6.24E-2	-4.94 ± 0.09	0.99370

that all samples obey the ISE behaviour which agrees with the experimental results. n can also be used to describe the hardness of the material. If the value of n is between 1 and 1.6, the material is hard and if n is greater than 1.6, the material is soft [18]. The value of n in Table 4:5 decreases with both GO and rGO doping. This results in n in the range of 1 - 1.6 for both 1 % wt. GO and rGO samples. Thus, showing that GO and rGO improves the hardness of YBCO.

4.4.4 Analysis According to PSR Model

$$\frac{F}{d} = \alpha + \beta d \tag{4.13}$$

The PSR model is a method to analyze the ISE behaviour of a material. This model assumes that the external work done by the indenter is split into two components. These are the surface energy component which is proportional to the area of the indentation and the strain energy component which is proportional to the volume of the resultant indentation [29]. The PSR model is shown in equation 4.13. α is the surface energy and its variation is associated with the energy dispersion of surface cracks [30] and β which is independent of the applied load is used to calculate the load independent hardness H_{PSR} as seen in equation 4:14 [30].

$$H_{PSR} = 1854.4\beta \tag{4.14}$$

The value of α and β are determined from a plot of d vs. F/d shown in Figure 4:4, were α is the y-intercept and β is the slope of the curve [27]. The values for α, β and LRC are listed in Table 4:6. The positive values of α confirm the ISE behaviour of the samples [30] as well as that there are both plastic and elastic deformations [7] occurring in both GO and rGO doped samples. The

increase in α suggests a reduction in cracks at grain interfaces [27]. Grain connectivity is also enhanced due to GO and rGO sheets filling voids and pores [9] [24]. Thus, this improved grain connectivity results in a reduction of cracks at grain interfaces.

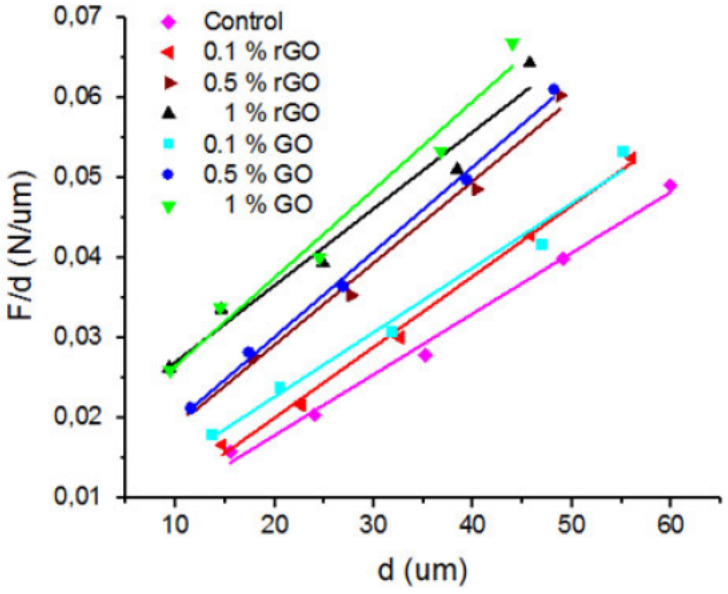

Figure 4:4: F/d vs. d for GO and rGO doped samples according to PSR model

The load independent hardness values calculated using the PSR model (H_{PSR}) increase with an increase in GO and rGO doping concentration seen in Table 4:6. Although H_{PSR} increases, it is still lower than H_V values of the plateau region shown in Figure 4:7 and Figure 4:8. Therefore, the PSR model is not sufficient to describe the micro-hardness of the GO and rGO doped samples.

Table 4:6: Best fit parameters for GO and rGO doped samples according to the PSR model.

Sample	$\alpha \times 10^{-2}$ (N/um)	$\beta \times 10^{-3}$ (N/um^2)	H_{PSR} (GPa)	LRC
Control	0.27 ± 0.01	0.76 ± 0.03	1.41 ± 0.06	0.99112
0.1 rGO	0.27 ± 0.01	0.88 ± 0.03	1.64 ± 0.06	0.99423
0.5 rGO	0.88 ± 0.02	1.02 ± 0.06	1.89 ± 0.11	0.98800
1.0 rGO	1.62 ± 0.03	1.08 ± 0.10	2.00 ± 0.19	0.96661
0.1 GO	0.66 ± 0.02	0.81 ± 0.06	1.50 ± 0.11	0.97628
0.5 GO	0.89 ± 0.01	1.06 ± 0.03	1.97 ± 0.06	0.99538
1.0 GO	1.66 ± 0.08	1.10 ± 0.10	2.04 ± 0.19	0.96557

4.4.5 Analysis according to EPD Model

$$F = A_2(d_e + d_p)^2 \tag{4.15}$$

EPD model, equation 4.15, is the second method which is used to characterize the ISE behaviour of materials. The EPD model assumes that there is a small amount elastic deformation which could not be measured. Due to it being recovered after F is removed [27]. A_2 represents the load independent micro-hardness constant [18], and d_e and d_p represent the elastic and plastic deformation components [6]. A_2 and de are calculated from the plot of $F^{0.5}$ vs. d_p which is shown in Figure 4:5. The hardness value calculated from the EPD model (H_{EPD}) is done by using equation 4.16. The results obtained for A_2, d_e, LRC and H_{EPD} are shown in Table 4:7.

$$H_{EPD} = 1854.4A_3 \tag{4.16}$$

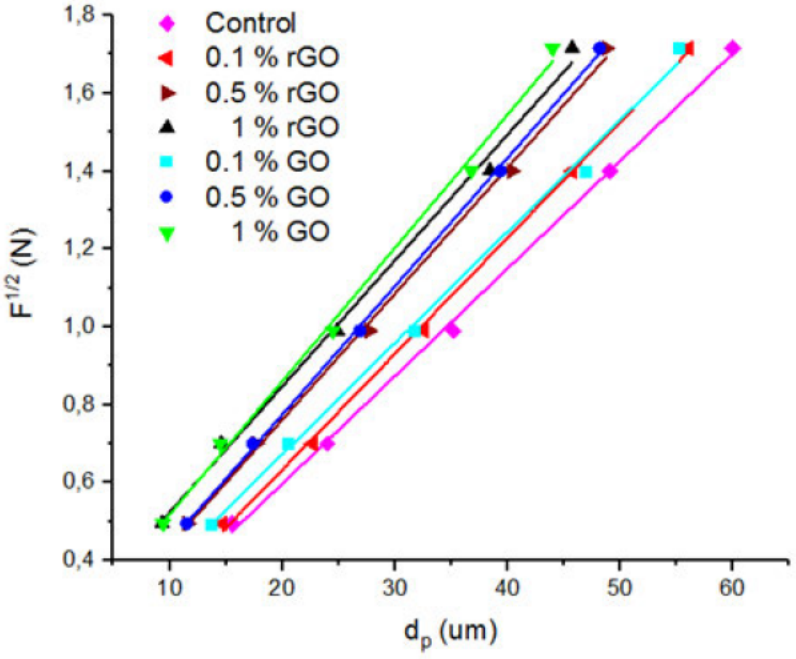

Figure 4:5: $F^{0.5}$ vs. dp for GO and rGO doped samples according to EPD model

Table 4:7: Best fit parameters for GO and rGO doped samples according to the EPD model.

Sample	$(A_2)^{\frac{1}{2}}$ (N/um^2)	d_e (um)	H_{EPD} (GPa)	LRC
Control	0.03 ± 6.04E-4	0.04 ± 0.02	1.45 ± 6.77E-4	0.99809
0.1 rGO	0.03 ± 5.25E-4	0.05 ± 0.02	1.67 ± 5.11E-4	0.99876
0.5 rGO	0.03 ± 7.45E-4	0.12 ± 0.02	1.90 ± 1.03E-4	0.99788
1.0 rGO	0.03 ± 1.21E-4	0.20 ± 0.03	2.02 ± 2.72E-4	0.99444
0.1 GO	0.03 ± 9.94E-4	0.10 ± 0.03	1.56 ± 1.83E-3	0.99519
0.5 GO	0.03 ± 4.61E-4	0.12 ± 0.01	2.02 ± 3.94E-4	0.99922
1.0 GO	0.03 ± 12.00E-4	0.18 ± 0.03	2.14 ± 2.67E-3	0.99508

The positive values for d_e implies that for this range of applied loads both elastic and plastic deformations are observed in the presence of elastic relaxation [31]. The presence of both elastic and plastic deformations explains the ISE behaviour of the samples which are being observed [18]. The increase in d_e for both GO and rGO doped samples demonstrates an increase in resistance to the applied load. This is attributed to GO and rGO sheets filling the voids and pores in the bulk material thus enhancing the elastic parameters [9].

The values calculated for H_{EPD} are low compared to the measured H_V plateau region. This can be seen in Figure 4:7 and Figure 4:8. Therefore, the EPD model cannot be used to describe the micro-hardness measurements.

4.4.6 Analysis according to HK Model

In 1973 Hays-Kendall found that in a material elastic deformation would occur below a certain applied load force and applying a force greater than this load force would result in plastic deformations. This value is known as the critical applied load force, W_{HK} [7] [27], this means that the indentation size will increase for applied load forces, F, greater than W_{HK}. This increase in indentation size is directly proportional to an effective load ($F_{eff} = F - W_{HK}$) and not the applied load [7], seen in equation 4.17.

$$F - W_{HK} = A_{1HK} d^2 \tag{4.17}$$

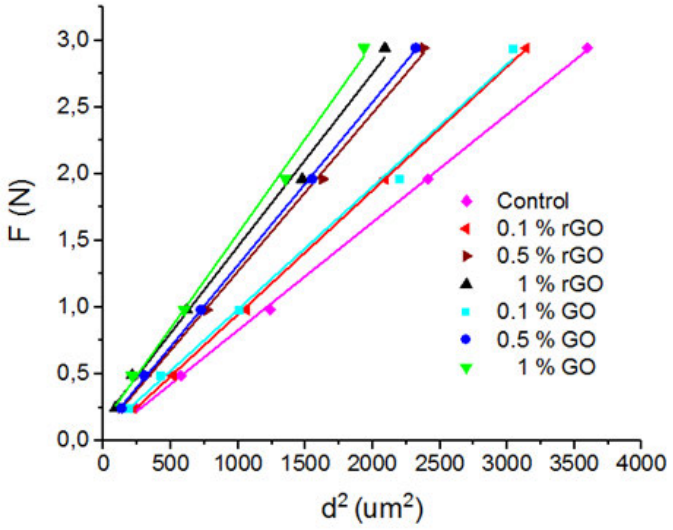

Figure 4:6: F vs. d^2 for GO and rGO doped samples according to HK model.

In equation 4.17 A_{1HK} is the hardness constant which is independent of the applied load force and d is the diagonal of the indentation [7]. Plotting the curve of F vs. d^2 seen in Figure 4:6 The W_{HK} can be obtained from the y intercept and A_{1HK} is equivalent to the slope of the curve [7]. These values can be seen in Table 4:8 along with the goodness of fit parameter LRC.

Table 4:8: Best fit parameters for GO and rGO doped samples according to HK model

Sample	$A_{1HK} \times 10^{-5}$ (N/um²)	W_{HK} (N)	H_{HK} (GPa)	LRC
Control	80.83 ± 1.12	0.021 ± 1.10E-3	1.50 ± 0.02	0.99923
0.1 rGO	92.82 ± 0.87	0.021 ± 1.20E-3	1.72 ± 0.02	0.99965
0.5 rGO	118.00 ± 2.35	0.087 ± 3.10E-3	2.19 ± 0.04	0.99843
1.0 rGO	130.00 ± 4.97	0.161 ± 5.80E-2	2.41 ± 0.09	0.99416
0.1 GO	91.84 ± 3.64	0.067 ± 2.00E-2	1.70 ± 0.07	0.99376
0.5 GO	122.00 ± 1.31	0.097 ± 1.60E-2	2.26 ± 0.02	0.99954
1.0 GO	142.00 ± 4.62	0.137 ± 2.50E-2	2.63 ± 0.09	0.99577

The values for W_{HK} are positive indicating typical ISE behaviour [7] [18]. The positive value of W_{HK} can be interpreted as both plastic (irreversible) and elastic (reversable) deformations occurring in the sample [7] [18]. This in agreement with α obtain in the PSR model as αd term in the PSR model is equivalent to W_{HK} in the HK model [32]. This increase in W_{HK} can be attributed to the enhancement in the elastic parameters of the material. This is due to GO and rGO sheets filling the voids and pores in the material [9]. The load independent micro-hardness according to the HK model can be calculated using equation 4.18 [6],

$$H_{HK} = 1854.4A_{1HK}. \tag{4.18}$$

The values of the load independent hardness shown in Table 4:8. The HK model best describes the micro-hardness measurements. As the calculated H_{HK} values are the nearest to the H_V measured in the plateau region this is observed in Figure 4:7 and Figure 4:8 and the LRC is closest to unity for the HK model in comparison to the EPD and PSR model. This result is realized due to GO and rGO filling the voids and pores in the YBCO material. This can be seen by a reduction in porosity in Table 4:4. Filling voids at grain boundaries results in the hindering of dislocation motion. This hindering of dislocation motion between grains, reduces the strain in the superconducting matrix. This reduction in strain enhances the elastic parameters of the material.

Table 4:9: Load independent mechanical parameters according to HK model.

Sample		H_{HK} (GPa)	E_{HK} (GPa)	Y_{HK} (GPa)	B_{HK} ($m^{\frac{1}{2}}$)	$K_{IC\text{-}HK}$ (Pa/$m^{\frac{1}{2}}$)
Control		1.50 ± 0.02	122.863 ± 1.639	0.500 ± 0.007	0.00185 ± 0.00021	811.509 ± 93.736
%wt. GO	0.1	1.70 ± 0.07	139.584 ± 5.737	0.568 ± 0.023	0.00196 ± 0.00040	869.796 ± 176.343
	0.5	2.26 ± 0.02	185.401 ± 1.639	0.754 ± 0.007	0.00126 ± 0.00012	1802.286 ± 169.470
	1.0	2.63 ± 0.09	215.810 ± 7.377	0.878 ± 0.030	0.00099 ± 0.00018	2640.201 ± 488.127
%wt. rGO	0.1	1.72 ± 0.02	141.059 ± 1.639	0.574 ± 0.007	0.00126 ± 0.00041	1364.544 ± 147.100
	0.5	2.19 ± 0.04	179.336 ± 3.278	0.729 ± 0.013	0.00122 ± 0.00017	1788.675 ± 241.845
	1.0	2.41 ± 0.09	197.613 ± 7.377	0.804 ± 0.030	0.00094 ± 0.00018	2560.631 ± 494.731

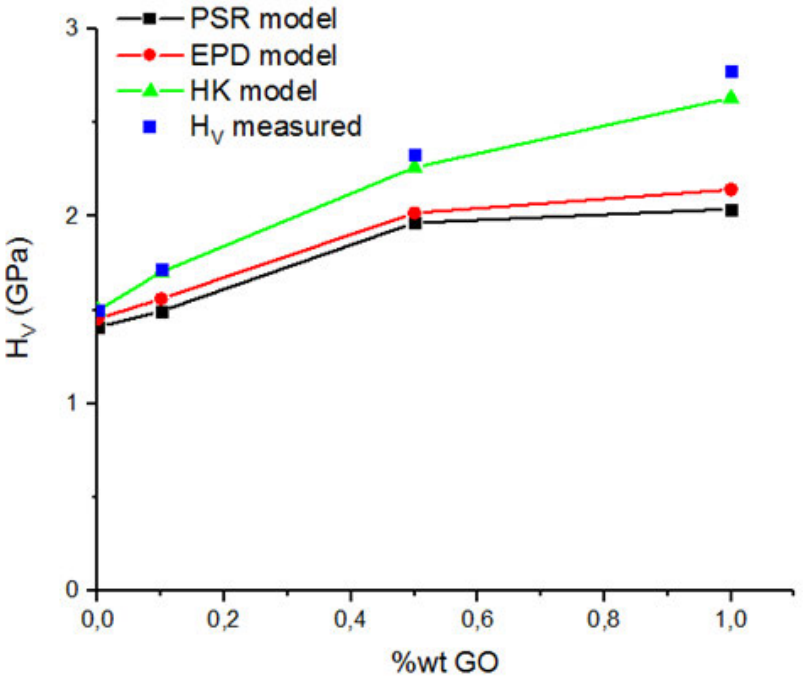

Figure 4:7: Comparison between measured (H_V is measured at the plateau of F vs. H_V curve) and calculated H_V for rGO doped samples according to different models.

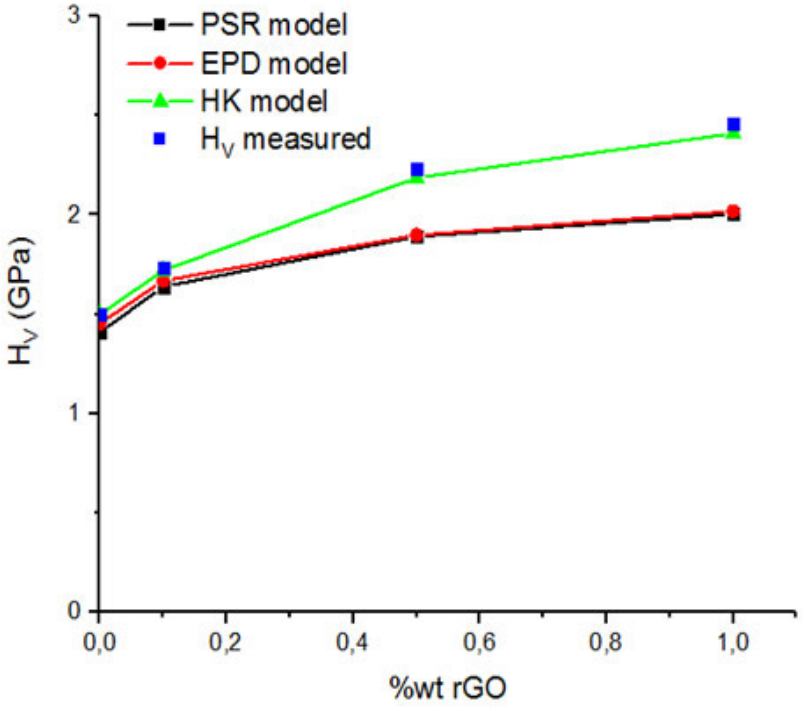

Figure 4:8: Comparison between measured (H_V is measured at the plateau of F vs. H_V curve) and calculated H_V for rGO doped samples according to different models.

This enhancement in elastic parameters explains the enhancement of W_{HK} in HK model. Enhancement in W_{HK} means that the force required to create plastic deformation on the surface

of the sample has increased.

H_{HK} has been used to calculate the load independent parameters E_{HK}, Y_{HK}, B_{HK} and $K_{IC\text{-}HK}$ seen Table 4:9. E_{HK} increased by 75 ± 6 % and 61± 6 %, Y_{HK} increased by 75 ± 6 % and 61± 6%, BHK increased by 75 ± 6 % and 61± 6 %, $K_{IC\text{-}HK}$ increased by 75 ± 6 % and 61± 6 % in GO and rGO doped samples respectively.

4.5 Conclusion

The orthorhombicity of the samples improved. This was at-tributed to the increase in oxygen content. Improvements in grain connectivity and reduction in porosity was observed, with an increase in GO and rGO doping concentration. This resulted in the enhancement of H_V, B, Y, E and K_{IC}.

Improvement of H_V is due to 2 factors: The reduction in grain size which results in an increased number of grain boundaries which hinders the motion of defects and secondly enhanced grain boundary connectivity due to GO and rGO filling voids and pores between grains. Analyses of the H_V measurements show that the HK model best describes the micro-hardness measurements. Doping of YBCO with GO and rGO improves the mechanical properties of YBCO.

References

[1] M. K. Wu, J. R. Asburn, C. J. Torng, P. H. Hor, R. L. Meng, L. Gao, Z. J. Huang, Y. Q. Wang and C. W. Chu, "Superconductivity at 93 K in a New Mixed-Phase Y-Ba-Cu-O Compound System at Ambient Pressure," *Physical Review Letters,* vol. 58, no. 9, pp. 908-910, 1987.

[2] M. Cryot and D. Pavuna, Introduction to Superconductivity and high Tc Materials, World Scientific Publishing Co.Pte.Ltd, 1992.

[3] D. E. Ford, S. S. Scott, A. S.S and W. D. Brown, "Comparison of High-Temperature Superconductor in Multi-Chip Applications," *Journal of the Arkansas Academy of Science,* vol. 48, pp. 45 - 49, 1994.

[4] M. Ainslie and H. Fujishiro, "Fundamentals of bulk superconductingmaterials," in *Numerical Modelling of Bulk Superconductor Magnetisation,* IOP Publishing, 2019, pp. 1-21.

[5] B. Sahoo, K. L. Routray, G. C. Mirdha, S. Karmakar, A. K. Singh and B. D. Samal, "Investigation of microhardness and superconducting parameters of CNTs blended YBCO superconductor," *Ceramics International,* vol. 45, no. 17, pp. 22055-22066, 2019.

[6] M. Dogruer, O. Gorur, F. Karaboga, G. Yildirium and C. Terzioglu, "Zr diffusion coefficient and activation energy calculations based on EDXRF measurement and evaluation of mechanical characteristics of $YBa_2Cu_3O_{7-x}$ bulk superconducting ceramics diffused with Zr nanoparticles," *Powder Technologvy,* vol. 246, pp. 553-560, 2013.

[7] M. B. Turkoz, S. Nezir, O. Ozturk, E. Asikuzum, G. Yildrium, C. Terzioglu and A. Varilci, "Experimental and theoretical approaches on mechanical evaluation of Y123 system by Lu addition," *Journal of Materials Science: Materials in Electronics,* vol. 24, no. 7, pp. 2414-2421, 2013.

[8] R. Terzioglu, S. P. Altintas, A. Varilci and C. Terzioglu, "Modeling of Micro-Hardness in the Au-Doped YBCO Bulk Superconductors," *Journal of Superconductivity and Novel Magnetism,* vol. 32, pp. 3377 - 3383, 2019.

[9] B. Sahoo and D. Behera, "Study of Transport and Elastic Properties of YBCO Superconductors by Inclusions of GnPs," *Physica C : Superconductivity and its Applications,* vol. 578, p. 1353748, 2020.

[10] M. Z. Gaffoor, J. A. L. L and J. C. Archer, "Investigating the critical transitional temperature increase in graphene oxide doped bulk YBCO," *Results in Physics,* vol. 44, 2023.

[11] S. Dadras, S. Falahati and S. Dehghani, "Effects of graphene oxide doping on the structural and superconducting properties of $YBa_2Cu_3O_{7-x}$," *Physica C,* vol. 548, pp. 65-67, 2018.

[12] B. Sahoo, A. K. Singh and D. Behera, "Graphene Oxide Modified Superconducting and Elastic Parameters of YBCO Superconductor," *Material Chemistry and Physics,* vol. 240, p. 122252, 2020.

[13] M. Z. Gaffoor and A. L. L. Jarvis, "Comparison of the Effect of Graphene and Graphene Oxide Doping on YBCO," *Journal of Physics:Conference Series,* vol. 1559, pp. 20-28, 2020.

[14] S. Dadras, S. Dehghani, M. Davoudiniya and S. Falahati, "Improving Superconducting Properties

of YBCO High Temperature Superconductor by Graphene Oxide Doping," *Materials Chemistry and Physics,* vol. 193, pp. 496-500, 2017.

[15] S. Falahati, S. Dadras and J. Mosqueira, "Investigation of the Magnetic and Transport Properties of $YBa_2Cu_3O_{7-\delta}$ High Temperature Superconductor Doped with Graphene Oxide," *Journal of Superconductivity and Novel Magnetism* , vol. 32, pp. 3755 - 3760, 2019.

[16] D. C. Marcano, D. V. Kosynkin, J. M. Berlin, A. Sinitskii, Z. Sun, A. Slesarev, L. B. Alemany, W. Lu and J. M. Tour, "Improved Synthesis of Graphene Oxide," *ACS NANO,* vol. 4, no. 8, p. 4806–4814, 2010.

[17] Z. Yang, Q. Q. Zheng, H. H. Qiu, J. L. Li and J. J. Y. Yang, "A Simple Method for the Reduction of Graphene Oxide by Sodium Borohydride with $CaC1_2$ as a Catalyst," *New Carbon Materials,* vol. 30, no. 1, pp. 41-47, 2015.

[18] N. E. Ghouch, R. Al-Oweni, K. Habanjar and R. Awad, "Comparative study on the effect of adding two transition-metal-substituted polyoxometalates on the mechanical properties of the (Bi,Pb)-2223 superconducting phase," *Journal of Physics and Chemistry of Solids* , vol. 151, 2021.

[19] S. Nakagawa and H. Schielzeth, "A general and simple method for obtaining R2 from generalized linear mixed-effects models," *Methods in Ecology and Evolution,* vol. 4, no. 2, pp. 133 - 142, 2013.

[20] "Crystallographic Resources," International Union of Crystallography, 15 October 2021. [Online]. Available: https://www.iucr.org/resources/other-directories/software/maud. [Accessed 8 July 2022].

[21] S. Georgieva, T. Nedeltcheva and A. StoyanovaIvanova, "Development of the Titrimetric and Spectrophotometric Methods for Determination of the Oxygen Content in Superconducting Cuprates," *American Chemical Science Journal,* vol. 13, no. 1, 2016.

[22] W. M. Chen, C. C. Lam, J. F. Geng, L. Y. Li, K. C. Hung and X. Jin, "A new calculating formula of iodometric titration for high Tc superconductors," *Physica C,* no. 270, pp. 155 - 158, 1996.

[23] M. Z. Gaffoor, A. L. L. Jarvis and S. Perumal, "Comparison of Graphene Oxide and Reduced Graphene Oxide Doping on YBCO For Power Applications," in *Southern African Universities Power Engineering Conference/Robotics and Mechatronics/Pattern Recognition Association of South Africa (SAUPEC/RobMech/PRASA),* Bloemfontein,South Africa, 2020.

[24] B. Sahoo, K. L. Routray, D. Samal and D. Behera, "Effects of Artificial Pinning Centers on YBCO High Temperature Superconductors Through Substitution of Graphene Nano-platelets," *Materials Chemistry and Phsyics,* vol. 223, pp. 784-788, 2019.

[25] B. B. Jung, H. K. Lee and H. C. Park, "Effect of grain size on the indentation hardness for polycrystalline materials by the modified strain gradient theory," *International Journal of Solids and Structures,* vol. 50, pp. 2719 - 2724, 2013.

[26] M. E. Barakat, "Influence of $Co_{0.5}Zn_{0.5}Fe_2O_4$ Nanoparticles Addition on Vickers Microhardness for Cu0.5Tl0.5-1223 Phase," *Journal of Superconductivity and Novel Magnetism,* vol. 30, no. 10, pp. 2945-2955, 2017.

[27] M. Anas, S. Ebrahim, I. G. Eldeen, R. Awad and A. I. Abou-Aly, "Effect of single and multi-wall carbon nanotubes on the mechanical properties of Gd-123 superconducting phase," *Chemical Physics Letters,* vol. 686, pp. 34-43, 2017.

[28] N. H. Mohammed, A. I. Abou-Aly, I. H. Ibrahim, R. Awad and M. Rekaby, "Effect of Nano-Oxides Addition on the Mechanical Properties of ($Cu_{0.5}Tl_{0.5}$)-1223 Phase," *Journal of Superconductivity and Novel Magnetism,* vol. 24, no. 5, pp. 1463-1472, 2011.

[29] R. Awad, A. I. Abou-Aly and M. M. H. Abdel Gawad, "The Influence of SnO_2 Nano-Particles Addition on the Vickers Microhardness of (Bi, Pb)-2223 Superconducting Phase," *Journal of Superconductivity and Novel Magnetism,* vol. 25, pp. 739-745 , 2012.

[30] M. Dogruer, F. Karaboga, G. Yildirim, C. Terzioglu and O. Ozturk, "A comprehensive study on mechanical properties of $Bi_{1.8}Pb_{0.4}Sr_2Mn_xCa_{2.2}Cu_{3.0}O_y$ superconductors," *Journal of Materials Science: Materials in Electronics,* vol. 24, no. 8, pp. 2459-2666, 2013.

[31] N. El Ghouch, R. Al-Oweini, K. Habanjar and R. Awad, "Comparative study on the effect of adding two transition-metal-substituted polyoxometalates on the mechanical properties of the (Bi,Pb)-2223 superconducting phase," *Journal of Physics and Chemistry of Solids,* vol. 151, p. 109807, 2021.

[32] R. Awad, A. I. Abou Aly, N. H. Mohammed, H. A. Motaweh and D. El-Said Bakeer, "Physical and Mechanical Properties of $GdBa_2Cu_3O_{7-\delta}$ Added with Nanosized $CoFe_2O_4$," *Journal of Superconductivity and Novel Magnetism,* vol. 27, no. 7, pp. 1757-1767, 2014.

Chapter Four Summary

In this chapter GO and rGO doping of YBCO was shown to enhance its mechanical parameters. Reasonings for the improvement of these mechanical parameters were investigated using structural analysis namely XRD.

Chapter 5 offers an explanation with proof for the increase in T_C above 93 K for GO doped YBCO samples. Previous research states that this increase in T_C above 93K is due to oxygen but this was shown to not be true in chapter 3.

Chapter 5

Peer-Reviewed Journal Article 3

Explanation of the Effects of Graphene Oxide doping on the Critical Transitional Temperature of Bulk YBCO

Mohammed Zaahid Gaffoor, Alan Lawrence Leigh Jarvis and Jonathan Celvin Archer

Published: *Results in Physics (2023)*

DOI*: http://dx.doi.org/10.1016/j.rinp.2022.106140*

5.1 Abstract

$Y_1Ba_2Cu_3O_{7-\delta}$ (YBCO) was doped with thermally stable graphene oxide (TS-GO) and thermally unstable graphene oxide (TU-GO) in the following %wt. concentrations: 0.1, 0.5 and 0.7. TS-GO and TU-GO was characterized using RAMAN, Fourier transform infrared spectroscopy (FTIR) and energy-dispersive x-ray spectroscopy (EDX). The critical transition temperature (T_{Cmid}) increased in all TU-GO and TS-GO doped samples. The highest T_{Cmid} of 101 K was that of the 0.7 %wt. TU-GO doped sample. The increase in T_{Cmid} was greater for the samples doped with TU-GO. Non-stoichiometric oxygen content was seen to increase with an increase in doping concentration of both TS-GO and TU-GO. X-ray diffraction (XRD) analysis was carried out to determine the lattice parameters and phase characterization of the TU-GO and TS-GO doped samples. Lattice parameters show an increase in the copper oxide (CuO_2) planar area with T_{Cmid} for TS-GO and TU-GO doping. To determine strain effects, the Williamson Hall method was used to determine the lattice strain (ε). The ε was seen to decrease for both TS-GO and TU-GO doped samples. The formation of magnetic manganese oxide nanoparticles in TS-GO and TU-GO doped samples was observed and resulted from impurities found in the graphene oxide (GO) dopant material. The magnetic particles were extracted magnetically and characterized using EDX. YBCO was doped with trimanganese tetraoxide (Mn_3O_4) and manganese dioxide (MnO_2) in a 0.1 and 0.2 %wt. concentration. The T_{Cmid} is seen to increase to 94 K and 104 K respectively for 0.1 %wt. MnO_2 and Mn_3O_4 doped samples. The 0.2 %wt. doped Mn_3O4 sample resulted in a decrease in T_{Cmid}. Magnetic susceptibility measurements confirmed a superconducting phase change. The increase in T_{Cmid} above YBCO's Tc = 93 K, correlates to the presence of manganese nano-impurities. This increase is hypothesized to be related to an increase in surface area of YBCO's 2D copper oxide (CuO_2) plane structure with GO doping.

5.2 Introduction

The high temperature superconductor, $Y_1Ba_2Cu_3O_{7-\delta}$ (YBCO), has a critical transition temperature (T_C) which is sensitive to oxygen content, reaching a maximum of 93 K [1]. Research is constantly being done to discover superconductors with higher $T_{C's}$ and attempting various methods to improve $T_{C's}$ of existing known superconductors. An improvement in T_C typically implies an improved critical current density (J_C), which allows for cheaper cooling systems enabling a wider range of applications [2]. A common method used to improve T_C is doping. In the past YBCO has been doped with various nanoparticles, carbon sources, metallic and non-metallic elements [3].

Doping YBCO with tungsten oxide (WO_3) resulted in an unchanged T_C [4]. Nickel (Ni), Iron (Fe) and cobalt (Co) dopants have been observed to increase T_C of YBCO to an optimum of 92 K. This optimum T_C was observed at 0.008 %wt. for Co and 0.004 %wt. for Ni and Fe [5]. Calcium (Ca) and strontium (Sr) doping results in the degradation of TC [5]. Ca, Ni and WO3 doping result in an enhancement in J_C. This increase in J_C is due to an increase in flux pinning sites [4] [6] [7].

Doping with carbon nanotubes (CNTs) has shown an enhancement in J_C [3] [8 - 10]. This improvement in J_C is due to enhanced grain boundary connectivity and an increase in flux pinning sites [3] [8 - 10]. T_C is seen to decrease or remained unchanged with an increase in CNT's concentration [3] [9] [10]. This decrease in T_C is attributed to separation of superconducting grains due to impurities located at grain boundaries induced by CNT doping [10] [3]. The same trend of a decreasing T_C and an increasing J_C was observed for doping YBCO with carbon nanofibers [11].
Doping YBCO with graphene (G) or graphene oxide (GO) has been observed to im-prove superconducting properties such as an increase in T_C [12 - 19], increase in J_C and an increase in critical magnetic field (H_C) [12].

Most studies define T_C, more specifically as T_{Cmid} from resistance measurements. T_{Cmid} is temperature at the midpoint of the transition between superconducting and normal state. Optimum doping concentrations, to yield maximum T_C values, vary between 0.7 to 1 %wt. GO for majority of studies [13] [15 -17], and one study shows an optimal T_C at 0.3 %wt. GO [14]. The maximum T_C values reached in these GO studies were: 101 K [13], 100 K [14], 95.46 K [15], 98 K [16], and 97 K [17]. In G doping YBCO studies maximum T_C was reached at 0.9 [18], 1.0 [12] and 3.0 [19] %wt. concentration. The maximum T_C values reached in these G studies were: 97.10 K [18], 92.6 K [12] and 100.6 K [19]. This increase in T_C in both G and GO doping experiments has been attributed to the increase in oxygen content due to the G and GO doping [13 - 19]. On the otherhand there are studies in which G and GO doping has resulted in no change in T_C as well as some studies in which T_C has decreased [20 - 23]. The decrease in

Tc was attributed to the decomposition of GO in samples at high temperatures during the annealing process [22]. Hence, there is contradictory evidence of the affect G and GO doping has on YBCO's Tc.

We question the 'increase in oxygen' explanation as it contradicts the well-known result that at optimum oxygenation YBCO has a maximum T_C = 93 K [1] [24] [25]. Furthermore, G contains much smaller amounts of oxygen compared to GO therefore the ex-planation does not seem plausible that oxygen from G would increase the T_C above 93 K. It is hypothesized the impurities produced during the GO (and G) production process, in particular manganese, affect T_C.

In this research the popular Hummers' method is used to produce GO [26]. An investigation of impurities found in GO was undertaken. The predominant impurities found in the produced GO were Mn-based salts such as MnO_2 and Mn^{2+} ions, which is sourced from the use of potassium permanganate ($KMnO_4$) in the Hummers' method [27] [28]. These Mn impurities will also be present in G, which requires a subsequent step after the production of GO when using the Hummers method. Oxygen level and impurities levels in G will be much lower than in GO. This is due to GO being chemically reduced to liberate O_2 and thereafter washed to produce G. This research is a focus on the affect of GO doping on YBCO.

It has been found when YBCO is doped with Mn_3O_4 in the range of 0.1 - 0.2 %wt., this results in an increase in TC above 93 K [29 -32]. Therefore, a manganese impurity investigation in our doped samples was conducted. The formation of Mn_3O_4 magnetic nanoparticles were identified in sintered GO doped YBCO samples, the sintering temperatures and oxygen atmosphere are the correct conditions for the formation of these nanoparticles. In these conditions the MnO_2 and Mn^{2+} impurities result in the formation of magnetic nanoparticles Mn_3O_4/Mn_2O_3 [33], which is easily collected when crushing GO doped YBCO samples.

This research suggests that there could be a combination of mechanisms attributing to an increase in T_C of GO doped $Y_1Ba_2Cu_3O_{7-\delta}$. Namely an increase in non-stochiometric oxygen, of under oxygenated YBCO samples, and (more importantly) the influence of Mn impurities found in GO dopants. Past research suggests that Mn^{2+} ions are most likely bonded to the GO sheets [28] hence, they would be highly mobile at sintering temperatures. It is further postulated that GO, with its large surface area greater than 5000 m^2/g, could help distribute small quantities of Mn evenly throughout the YBCO samples, resulting in a homogeneously doped material.

5.3 Experimental

GO was produced using the Hummers' method with additional $KMnO_4$ [34]. The resultant GO only underwent 'one washing cycle' to produce thermally unstable graphene oxide (TU-GO).

A single washing cycle consists of centrifuging the resultant GO for 15 min at 5000 rpm. The resultant supernatant was discarded, and the precipitate was mixed with water. This GO and water solution was passed through a metal sieve with a nominal opening of 300 µm, to remove any large particles and unreacted precursor material. Thereafter the solution was centrifuged again for 15 min at 5000 rpm. This process was carried out three more times using hydrochloric acid and twice with ethanol. Thus, resulting in one washing cycle.

Thermally stable graphene oxide (TS-GO) was produced by GO undergoing four washing cycles. TU-GO has a larger number of impurities compared to TS-GO hence making it thermally unstable [35] [36]. TS-GO and TU-GO were characterized using FTIR, RAMAN and EDX.

Bulk YBCO (Y123 phase) powder with a purity of 99.9 % was purchased from Super-conductors Inc.. Each YBCO sample was prepared by doping 2.0 g of YBCO powder with 0.1 (0.002), 0.5 (0.01) and 0.7 (0.014) %wt. (g) TS-GO and TU-GO. YBCO pellets with a weight of 0.73 g, radius of 12 mm and thickness of 2 mm, where then pressed with a mechanical die at an applied pressure of 45 MPa for a period of 15 minutes. The highest doping concentration that was attainable to compare TS-GO versus TU-GO samples was 0.7 %wt. Any TU-GO samples with a concentration greater than 0.7 %wt. resulted in samples exploding during the sintering process. This explosion is due to the escape of trapped impurities found between GO planes [37]. It is possible to dope YBCO with TS-GO concentrations greater than 0.7 %wt. [16]. Pellets were sintered at 950˚C for 6 hours in an oxygen atmosphere. The control sample produced using this sintering curve is referred to as control A.

Resistivity vs. Temperature (ρ vs. T) measurements were conducted using the four-wire resistance measurement method to compare the T_{Cmid} of TU-GO and TS-GO doped samples [13]. The δ of YBCO samples was determined through the process of iodometry [38].

XRD measurements were carried out to determine phase characterization and lattice parameters of TU-GO and TS-GO doped samples. This was done using the Rietveld refinement method on Material Analysis Using Diffraction (MAUD) software. MAUD is a software used for general diffraction analysis. Its program is mainly based on Rietveld refinement analysis [39].

Williamson hall method was used to calculate the lattice strain(ε), for each sample using the following equation 5.1:

$$\beta_{hkl}\cos\theta = \frac{K\lambda}{D} + 4\varepsilon\sin\theta, \quad (5.1)$$

where β_{hkl} is the full width half maximum (FWHM) of diffraction peaks, K is the dimensionless shape factor, which is approximately 0.9, D is the crystallite size, θ is the angle of the diffraction peak and λ is the x-ray wavelength. To determine the ε, $\beta_{hkl}\cos\theta$ vs. $4\sin\theta$ is plotted for the main diffraction peaks of each sample and a linear best fit line is used. The gradient of this line is equivalent to ε [14].

To confirm the formation of Mn magnetic nanoparticles in our samples, YBCO control and 0.7 %wt. TU-GO doped samples were crushed. A rare earth metal magnet was placed over each crushed sample and collected small quantities of magnetic particles. The particles were assumed to be impurities from the GO as no particles were magnetically collected from the control. Due to the small amount collected several EDX points were taken to determine the chemical composition of particles.

It was observed that the magnetic nanoparticles consisted mostly of Mn and O. Considering the sintering profile, it could be assumed that these magnetic particles are Mn_2O_3 or Mn_3O_4 [33]. To determine the structure of these magnetic impurities, MnO_2 powder (non-magnetic) was sintered using the same sintering profile as that used for the TS-GO and TU-GO doped YBCO samples. The MnO_2 powder and the product after sintering were characterized using XRD and FTIR. The powder after sintering was found to be magnetic Mn_3O_4.

Thereafter 2 g of YBCO was doped with MnO_2 and Mn_3O_4 with 0.1 (0.002) and 0.2 (0.004) %wt. (g) concentrations, to determine if these dopants can indeed increase the T_C of YBCO above 93 K. YBCO doped MnO_2 and Mn_3O_4 pellets have the same weight, size and shape as TS-GO and TU-GO doped samples. The sintering profile of these samples were adjusted to get the control B sample as close as possible to optimum oxygenation for the maximum Tc = 93 K. This was achieved by adding a dwell period of 3 hours at 350˚C. TC of MnO_2 and Mn_3O_4 doped samples were determined using ρ vs. T curves.

To confirm ρ(T) superconductivity T_C measurements, AC susceptibility magnetic measurements were conducted using a DSP enhanced AC susceptometer [40]. The frequency of the AC signal used was 1 kHz and the applied magnetic field was 3 Oe.

5.4 Results

5.4.1 Characterization of TS-GO and TU-GO

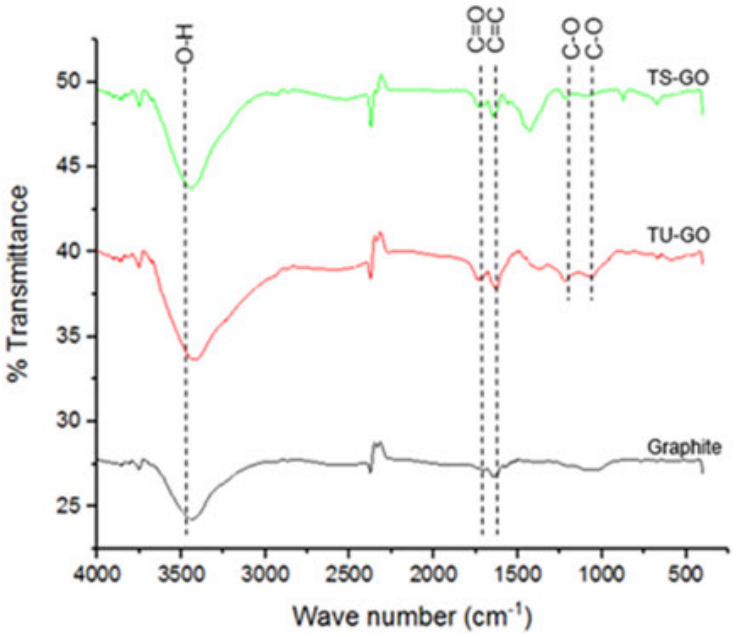

Figure 5:1: FTIR spectrum of graphite, TS-GO and TU-GO.

In Figure 5:1, FTIR shows the increase in oxygen groups in TS-GO and TU-GO com-pared to graphite, thus showing the oxidation of the graphite precursor material. The O-H peak in graphite is due to intercalated water found in natural graphite [41], which was used to produce TS-GO and TU-GO. There are more oxygen groups in TU-GO than TS-GO, which can be seen by the larger O-H, C=O and C-O peaks in TU-GO than in TS-GO. The reason for the greater amount of oxygen in TU-GO is a result of the three extra washing cycles which were carried out to produce TS-GO. During these extra washing cycles oxygenated impurities are removed, thus resulting in a reduction in oxygen in TS-GO compared to TU-GO [42].

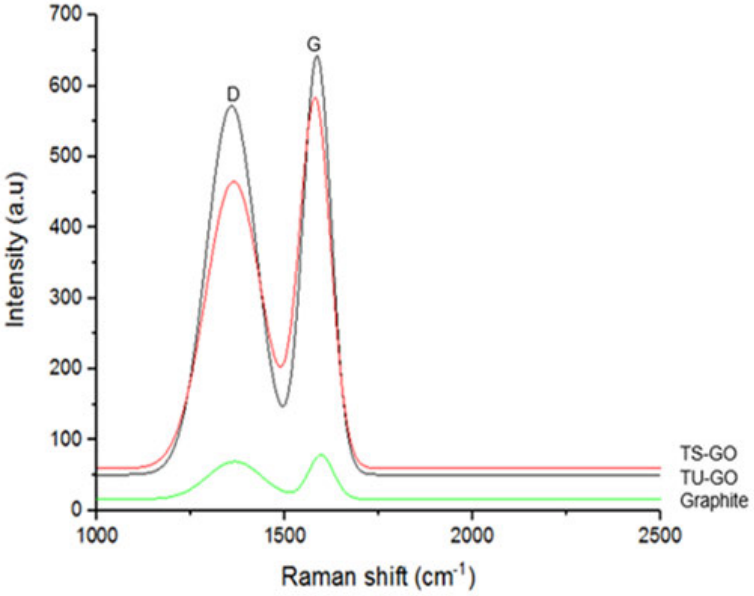

Figure 5:2: RAMAN spectrum of graphite, TS-GO and TU-GO.

The characteristic D and G peaks of GO and graphite can be seen in the RAMAN spectrum of TS-GO, TU-GO and graphite in Figure 5:2 [43] [44]. The D peak is a result of out of plane vibrations which is due to structural defects and the G peak is a result of in plane vibrations from sp2 carbon atoms [43]. The D peaks for TS-GO, TU-GO and graphite occur at 1363 cm^{-1}, 1356 cm^{-1} and 1365 cm^{-1}, and the G peaks occur at 1589 cm^{-1}, 1583 cm^{-1} and 1592 cm^{-1} respectively. The ratio of I_D /I_G for TU-GO and TS-GO is 0.891 and 0.798 respectively. The smaller ratio for TS-GO indicates a reduction in defects in TS-GO material [45]. This reduction of defects can be attributed to the decrease of impurities in TS-GO compared to TU-GO, which is due to TS-GO undergoing three extra washing cycles removing more impurities.

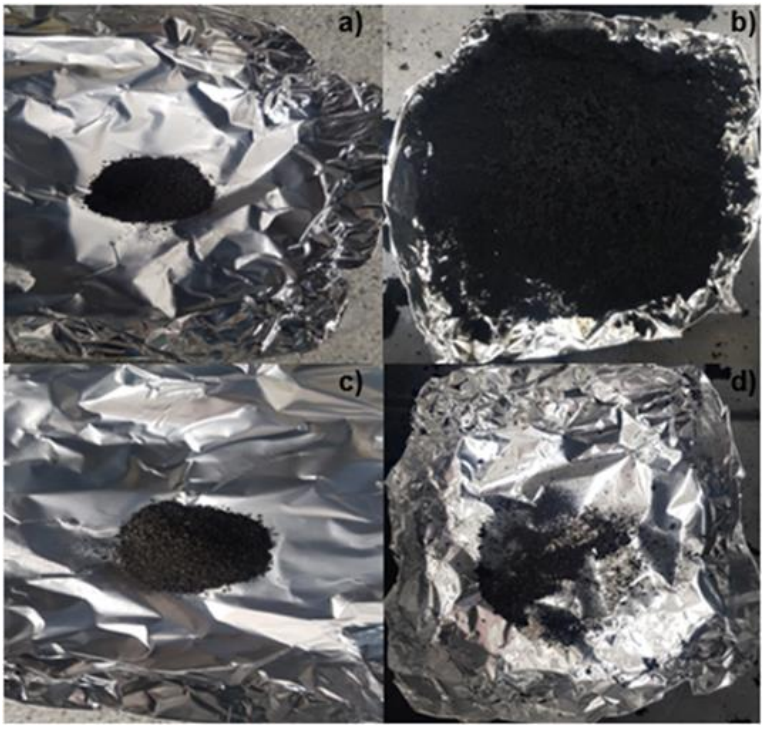

Figure 5:3: (a) TU-GO at 25 ◦C, (b) TU-GO at 200 ◦C, (c) TS-GO at 25 ◦C, (d) TS-GO

It has been observed that TU-GO powder will expand due to its impurity content at an elevated temperature. To test the expandability of TU-GO compared to TS-GO, 0.5 g of TU-GO and TS-GO were each placed into aluminum foil boats shown in Figure 5:3(a) and Figure 5:3(c). These samples were then placed in an oven and heated up to 200˚C. The product of this heating process is reduced graphene oxide (rGO). Figure 5:3(b) shows the result of rapid expansion in the volume of TU-GO and a reduction in the volume of TS-GO seen in Figure 5:3(d). This increase in volume is due to the release of highly energized gas forcefully from between GO layers, thus pushing the layers apart hence increasing the volume [37]. Since TS-GO has fewer impurities, less gas is released. Therefore, the release is not as forceful thus layers of TS-GO are not pushed apart, resulting in a shrinkage of its volume [37]. The mass of both samples decreased [37]. This decrease in mass of both TS-GO and TU-GO and expansion in volume of TU-GO is due to the release of gases such as CO, CO_2 and water vapor [37] [46] and has also been attributed to potassium impurities [35] [36].

Table 5:1: Average of several EDX points of TU-GO and TS-GO.

Element Composition (%wt.)	TU-GO (Expandable)	TS-GO (Non-expandable)
Carbon (C)	60.34	67.52
Oxygen (O)	38.62	32.01
Sodium (Na)	0.04	0.02
Sulphur (S)	0.22	0.15
Manganese (Mn)	0.44	0.28
Potassium (K)	0.34	0.02

The EDX in Table 5:1 shows the reduction in the amount of impurities in TS-GO compared to TU-GO and most importantly the presence of the manganese impurities in the material. Sodium (Na), sulphur (S) and potassium (K) are also impurities resulting from the Hummers' method [27].

5.4.2 Xray Diffraction Analysis

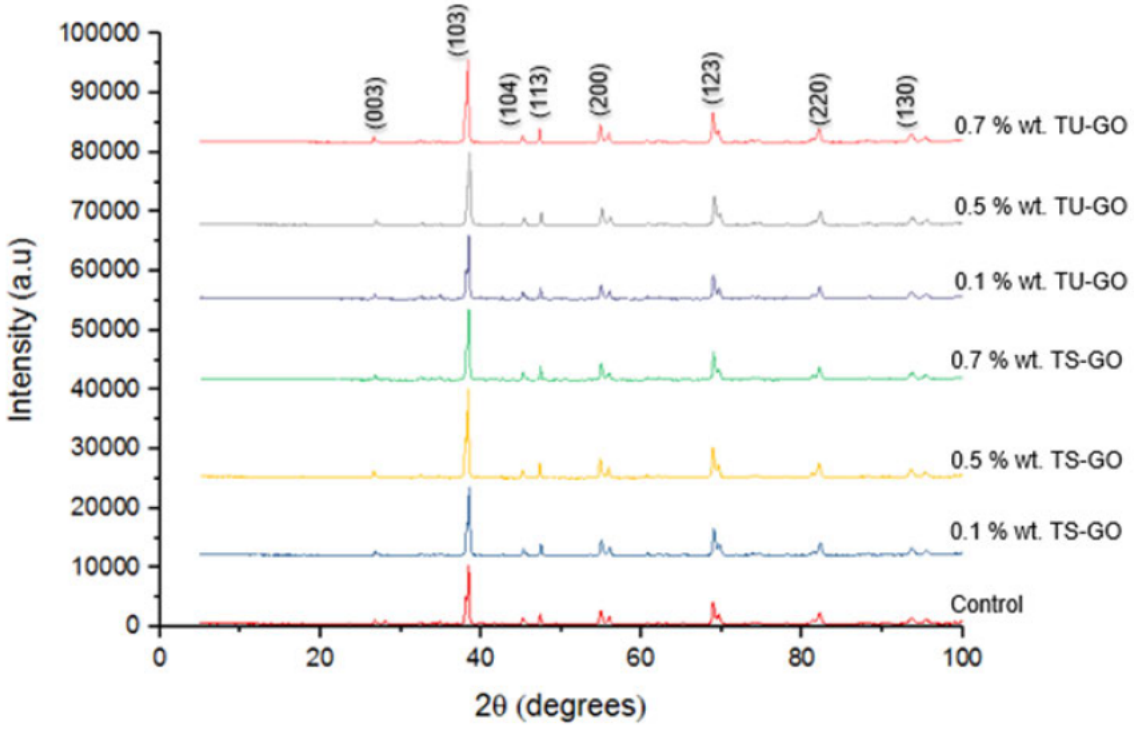

Figure 5:4: XRD pattern for control, TS-GO doped and TU-GO doped samples

XRD was carried out to conduct structural phase analysis of doped samples shown in Figure 5:4. XRD confirms the samples have single phase orthorhombic structure showing the following planes (003), (103), (104), (113) (200) (123) (220) and (130). These planes are characteristic of the Y123 phase [14] [19]. MAUD revealed the presence of no other YBCO phases such as Y211, Y247 and Y124, after the sintering process.

The b-axis parameter seen in Table 5:2, increases in both TS-GO and TU-GO doped samples due to the increasing oxygen content in the copper oxide (CuO) chains [19]. This increase in the b-axis results in a decrease in the c-axis. The reduction in the c-axis is due to the increasing pressure on the apical oxygen bond length which is caused by the increasing oxygen content seen in Table 5:2 [18]. This trend of the b and c lattice parameters are not followed by the TS-GO 0.5 %wt. doped sample. This could be attributed to an increased amount of im-purities in the sample resulting in lattice defects which will in turn affect the lattice parameters.

Table 5:2: Oxygen content, lattice strain, T_C and lattice parameters of control, TS-GO and TU-GO doped samples.

Sample	Control A	0.1 % wt.		0.5 % wt.		0.7 % wt.	
		TU-GO	TS-GO	TU-GO	TS-GO	TU-GO	TS-GO
$Tc_{mid}(K)$	82	94	90	97	93	101	99
Resistivity (Ω-mm) at 120 K	0.4494	0.3603	0.3624	0.3595	0.2724	0.3446	0.1975
Oxygen Content	6.71	6.76	6.74	6.84	6.82	6.91	6.89
Lattice Strain	0.00175	0.00106	0.00127	0.00021	0.00118	0.00107	0.00020
a(Å)	3.82563	3.82596	3.82396	3.82731	3.82747	3.82990	3.82918
b(Å)	3.88709	3.88769	3.88724	3.88777	3.88603	3.88859	3.88777
c(Å)	11.67142	11.67039	11.66997	11.66875	11.67416	11.66347	11.66878

The Williamson Hall plots of $\beta_{hkl}\cos\theta$ vs. $4\sin\varepsilon$ is used to calculate ε seen in Figure 5:5 and ε values are shown in Table 5:2. ε is found to be positive, which indicates tensile strain [14]. The

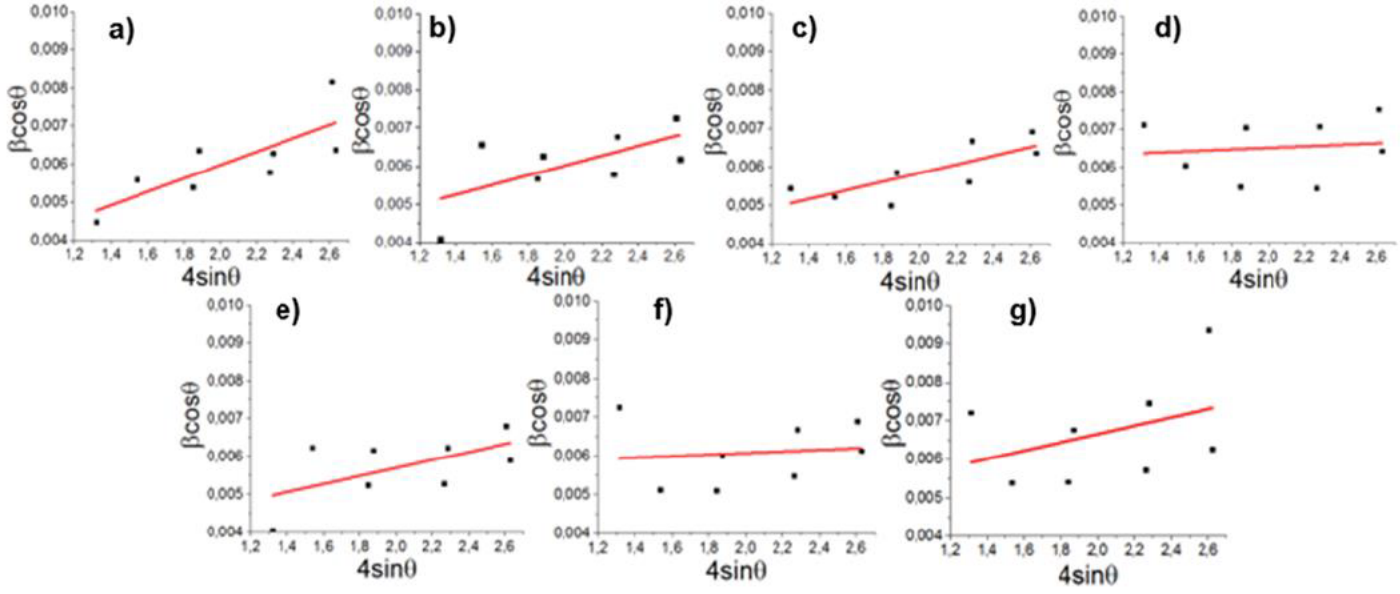

Figure 5:5 : Williamson Hall plots of (a) control (b) 0.1 %wt. TS-GO (c) 0.5 %wt. TS-GO (d) 0.7 %wt. TS-GO (e) 0.1 %wt. TU-GO (f) 0.5 %wt. TU-GO (g) 0.7 %wt. TU-GO.

strain values are seen to decrease with an increasing amount of TS-GO and TU-GO doping concentration. This could be attributed to graphene sheets at the intergranular spaces between grains, which results in the hindrance of the dislocation motion between grains and improvement in grain connectivity. This reduction in dislocation movement and improved grain connectivity results in a decrease in lattice strain [15].

5.4.3 Nano-Magnetic Impurity Analysis

EDX spectrum of magnetic nanoparticles can be seen in Figure 5:6. The presence of carbon (C) is expected as the material is doped with GO. Yttrium (Y), barium (Ba) and copper (Cu) is from the YBCO superconductor. Oxygen is present because it is found in both GO and YBCO. The elements which cannot be accounted for are the impurities found in the material which are: S (sulphur), europium (Eu), molybdenum (Mo), aluminium (Al) and Mn. All impurities accept Eu can be attributed to the Hummer's' method of production [27]. Eu can be accounted for as an impurity from the YBCO powder. It is observed that Mn and O have the greatest presence in the magnetically retrieved magnetic nanoparticles. Since these particles are magnetic, and it is known that Mn^{2+} impurities occur in GO [27], considering that the sintering temperature is 950˚C this would allow for MnO_2 to oxidize to form Mn_3O_4 [33]. It is postulated that these magnetic particles are Mn_3O_4.

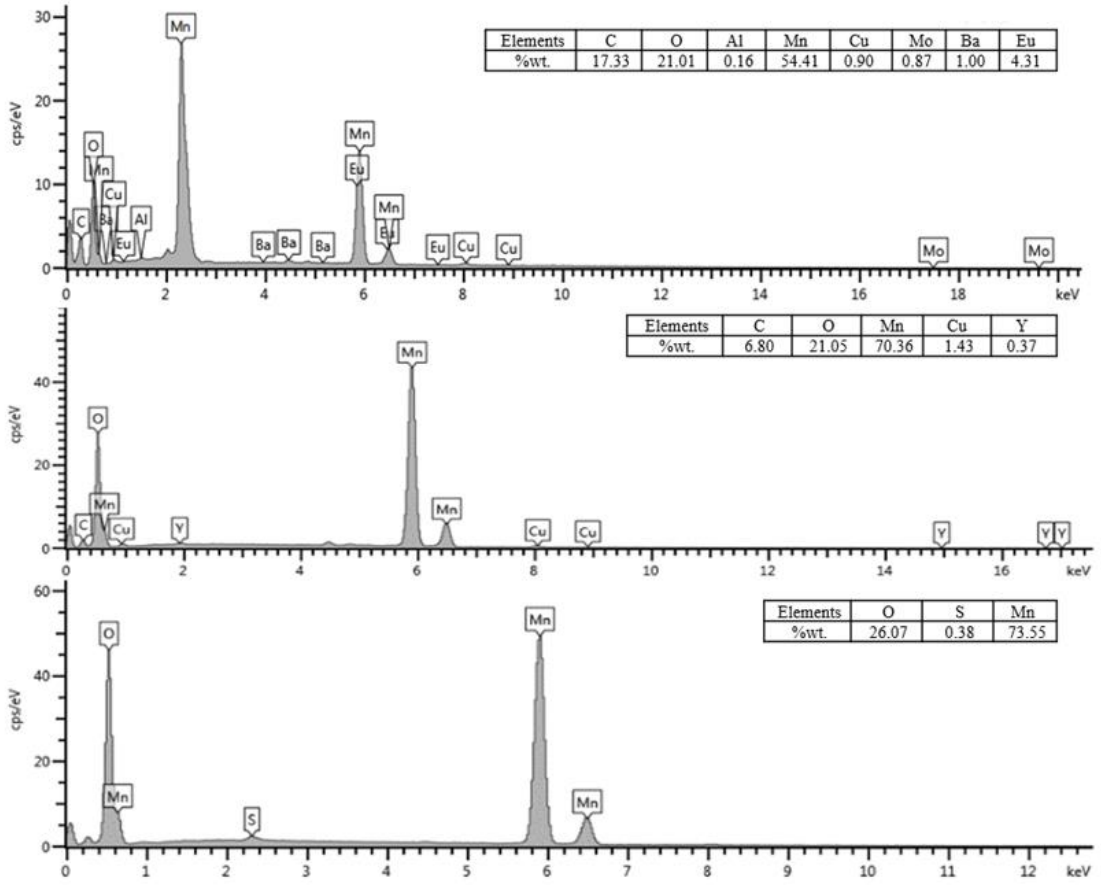

Figure 5:6 : EDX spectra of nano magnetic impurities.

5.4.4 Characterization of Manufactured Magnetic Nano Particles

Diffraction spectrums, shown in Figure 5:7 confirmed that the starting material is MnO_2 and post heat treatment formation of Mn_3O_4. MnO_2 spectrum shows peaks which are due to the following planes: (110), (101), (200), (111), (210), (211), (220), (002), (310) and (301). These planes are characteristic peaks of MnO2 beta phase [47] [48], which has a tetragonal crystal structure [48]. The lattice parameters are calculated to be a = b = 4.388 Å and c = 2.865 Å.

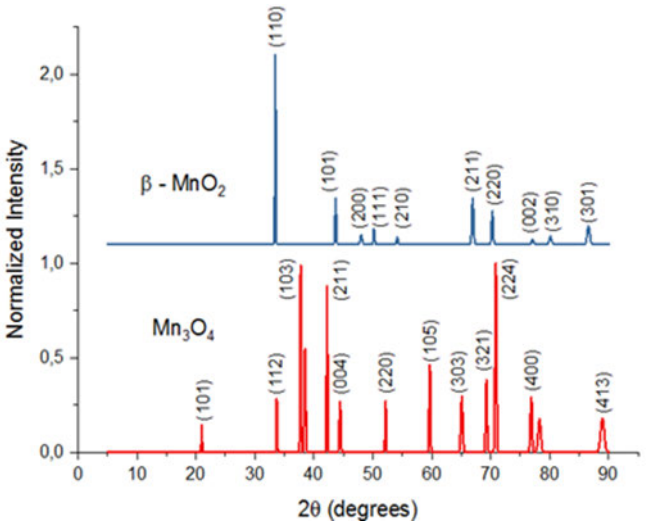

Figure 5:7: XRD spectra of MnO_2 and Mn_3O_4.

The diffraction spectrum of the Mn_3O_4 powder can be seen to have the following peaks: (101), (112), (200), (103), (211), (004), (220), (105), (312), (303), (321), (224), (400) and (413) which are characteristic peaks of Mn_3O_4 [49] [50]. These crystals have a tetragonal hausmannite [49] [50] phase with lattice parameters a = b = 5.762 Å and c = 9.476 Å.

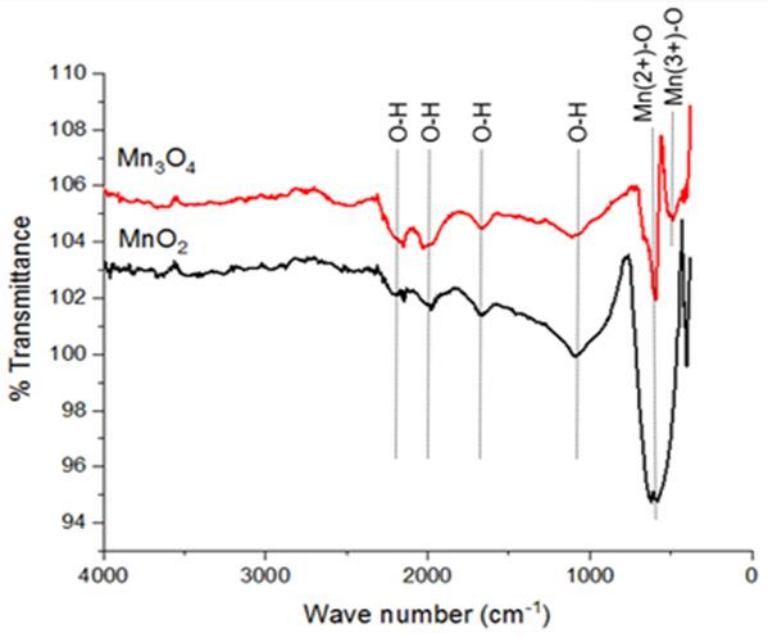

Figure 5:8: FTIR spectra of MnO_2 and Mn_3O_4.

The FTIR spectrum for MnO_2 and Mn_3O_4 is seen in Figure 5:8. The peaks observed at 1084 cm^{-1} is due to O-H bond bending vibrations more specifically γ-OH and δ-2 OH combined with Mn atoms [48] [50] [51]. These O-H bonds are a result of absorbed moisture [48] [50]. The peaks observed at 1663 cm^{-1}, 1986 cm^{-1} and 2223 cm^{-1} is a result of vibrations of weakly

bonded water molecules [48] [50]. The peak at 604 cm^{-1} is due to the vibration of Mn^{2+}-O bonds at the tetrahedral sites [48] [49]. The Mn^{2+}-O peak is seen to be much larger in MnO_2 than in the Mn_3O_4 spectrum. This is due to the oxidation of MnO_2 to form Mn_3O_4. This results in a reduction of Mn^{2+} tetrahedral sites and the formation of Mn^{3+} ions in the octrahedral sites [52]. The formation of these trivalent manganese ions can be observed by the Mn^{3+}-O peak at 500 cm^{-1} [49] [50] which occurs in the Mn_3O_4 spectrum but not in the MnO_2 spectrum.

5.4.5 Critical Transition Temperature Analysis of TS-GO and TU-GO doped YBCO

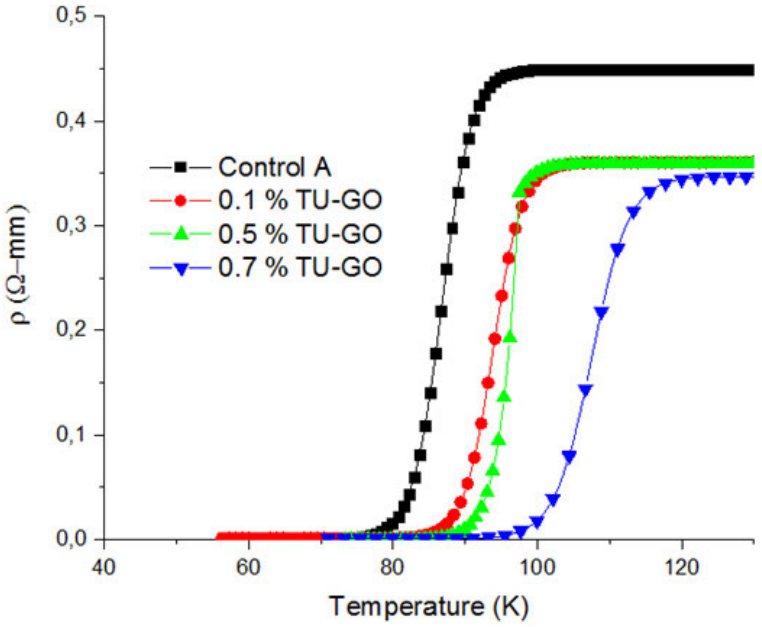

Figure 5:9: ρ vs T curves for TU-GO doped samples.

The ρ vs. T curves for TU-GO and TS-GO doped samples are shown in Figure 5:9 and Figure 5:10 respectively. Resistivity decreased in both TU-GO and TS-GO doped samples. This decrease in resistivity is due to improved grain connectivity. This is caused GO in the grain boundary region being reduced to graphene during the sintering process. Since graphene is a good conductor thus it improves grain connectivity [16] [17]. The reduction in resistivity was greater in the TS-GO doped samples as compared to the TU-GO doped samples. This can be attributed to a higher amount of impurities in the TU-GO doped samples, as there were fewer washing cycles used compared to TS-GO. From past research its observed that majority of the impurity elements increase resistivity of YBCO. Sulphur doped YBCO has resulted in multiphase material [53]. This would result in an increase in resistivity. Addition of Mo, K, or Mn to YBCO increases the resistivity [30] [54] [55]. Doping YBCO with Al results in a

decrease in resistivity [56]. Thus having all these impurities in TU-GO doped samples results in a greater resistivity in TU-GO doped samples compared to TS-GO. Resistivity values at 120 K for TU-GO and TS-GO samples can be seen in Table 5:2.

The T_{Cmid} of both TS-GO and TU-GO doped samples increase with an increase in dopant amount seen in Table 5:2. One explanation for the increase in T_C up to the limit of T_{Cmax} = 93 K, may be attributed to the oxygen in the functional groups of TS-GO and TU-GO being removed during the sintering process and entering the Cu-O chains of YBCO. This increase in oxygen content is shown in Table 5:2. TU-GO doped samples have higher $T_{C's}$ than TS-GO doped samples, which can be seen in Figure 5:9 and Figure 5:10. It has been suggested that this increase in oxygen content is the main factor in increasing T_C up to 93 K and beyond [14 - 17]. We do not agree with this explanation beyond 93 K as the optimum oxygenation of YBCO Y123 results in a maximum T_C of 93 K [1] [25].

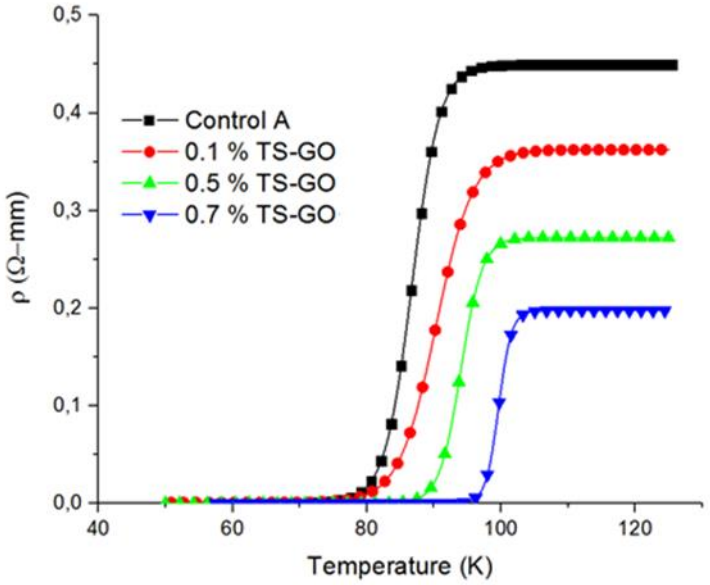

Figure 5:10: ρ vs T curves for TS-GO doped samples.

We suggest an alternative T_C increasing mechanism. Given the fact that from our XRD analysis we have a single Y123 phase there was a focus on impurities within all samples. Table 5:1 and Figure 5:6 shows all impurities present in YBCO samples: Mn, Na, K, S, Mo, Al and Eu. The effects of doping with these impurity elements have on T_C of YBCO were investigated. Past research has shown that doping YBCO with Na and S does not cause any change in T_C [53] [57]. Certain S and K doping experiments have shown a enhancement in T_C but not greater than 93 K [53] [54]. On the otherhand some K and S doped YBCO experiments has shown a decrease in T_C [54] [58]. Doping of YBCO with Mo and Al in the past has shown a decrease in T_C [55] [59]. Doping of YBCO with Eu results in an enhancement in T_C but not greater than 93 K [60]. Upon further investigation research has shown that doping with Mn and Mn_3O_4 particles has been seen to increase the T_C of YBCO above 93 K [29 - 32] [61] [62]. This resulted in a focus

on Mn impurities in the YBCO doped samples. It was also noted that Mn impurities had the highest concentration of all impurities in doped YBCO samples. According to past research the sintering temperature of 950˚C is the temperature at which YBCO-Mn composites are sintered to achieve optimum T_C [63]. This is the equivalent to the sintering temperature used in this research.

The source of Mn is attributed to the synthesis of GO via the popular used Hummers' method. GO analysis has found that the majority manganese impurities are Mn^{2+} ions [27]. MnO_2 is a result of the decomposition of $KMnO_4$ used during the Hummers' method [27]. Taking into account the sintering profile in which doped YBCO samples are sintered, one can deduce that MnO_2 could be further oxidized to Mn_3O_4 magnetic nano-particles [33], and Mn which have been found as inclusions in the YBCO matrix [32].

5.4.6 Critical Transition Temperature Analysis of Manganese Oxide doped YBCO

In order to confirm the effect of Mn doping on YBCO's T_C [29 - 32] Mn doping experiments were conducted. Control B was prepared using the adjusted sintering profile and has a T_{Cmid} of 90 K seen in Figure 5:11. This is an 8 K improvement on the T_C of the previous control (control A) and was achieved by increasing the duration of the sintering time. This increase in sintering time in the adjusted sintering profile results in an increase in non-stochiometric oxygen content hence increasing T_C [14] [17] [24].

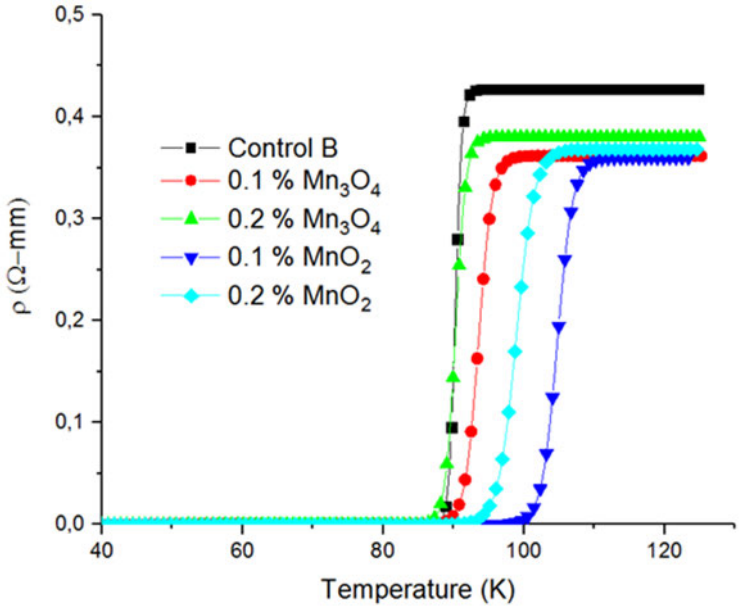

Figure 5:11: ρ vs T curves for MnO_2 andMn_3O_4 doped samples.

The MnO_2 and Mn_3O_4 powders were sonicated for 1 hour to reduced particle size. Thus, allowing for a more even distribution of dopant material. Thereafter each doped sample was mixed with an agate pestle and motar for 20 min, before being pressed at 45 MPa into a pellet

of radius 12 mm and 3 mm thickness.

The doping of YBCO with 0.1 %wt. Mn_3O_4 is seen to increase the T_{Cmid} to 94 K. Increasing the doping concentration to 0.2 %wt. Mn_3O_4, results in a decrease of T_{Cmid} to 88 K. Doping with MnO_2 in 0.1 and 0.2 %wt., increased T_{Cmid} to 104 K and 98 K respectfully. ρ vs. T curves can be seen in Figure 5:11.

The decrease in T_C in the Mn_3O_4 0.2 %wt. doped sample, may be due to excessive concentration of the magnetic particles [31], as magnetic fields oppose the formation of the superconducting state. Unlike MnO_2, Mn_3O_4 is a stable compound during sintering [32]. During sintering the MnO_2 dopant would decompose to Mn and O, and later form Mn oxides such as Mn_3O_4, Mn_2O_3 or remain as Mn inclusions in the YBCO matrix [32] [33].

5.4.7 AC Susceptibility

Magnetic measurements were conducted to confirm T_C resistivity measurements. Fundamentally, it is the diamagnetic response of the superconducting state that is important.

Table 5:3: T_{CONSET} from ρ vs. T curve and χ' vs. T curves

Sample	Control A	Control B	0.1 %wt. MnO_2	0.7 %wt. TU-GO
T_{Conset} (K) (ρ vs. T)	91.3	91.8	109.2	114.11
T_{Conset} (K) (AC susceptibility)	92.4	92.1	111.4	115.7

AC susceptibility versus temperature (χ' vs. T) measurements of control A, control B, 0.7 %wt. doped TU-GO and 0.1 %wt. doped MnO_2 samples are shown in Figure 5:12. These samples were selected as they displayed the greatest increase in T_{Cmid} of 101 K and 104 K respectively as shown in Figure 5:9 and Figure 5:11.

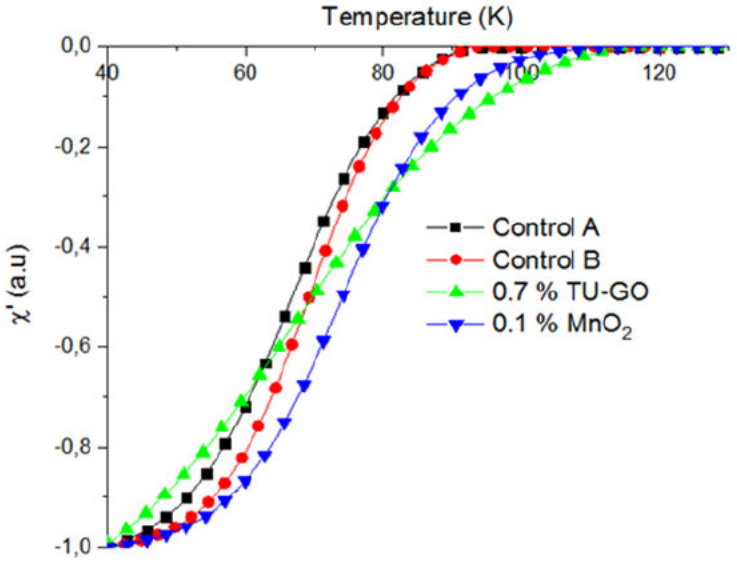

Figure 5:12: AC susceptibility versus temperature curves.

Table 5:3 shows a comparison of T_{Conset} measured from the ρ vs. T data, with T_{Conset} measured from the χ' vs. T data. It is observed that the T_{Conset} determined using the AC susceptibility measurements is marginally greater than that from the ρ vs. T measurements. As well as the superconducting phase change is broader in the AC susceptibility measurement when compared to the ρ vs. T measurements. These observations are a result of the AC susceptibility measurement being a bulk response were as the ρ vs. T measurement gives a response local to part of the material. Therefore AC susceptibility measurement's will identify any superconducting state change irrespective of it being intra-grain or inter-grain were as ρ vs. T measurements will identify superconductivity only if it is both intra-grain and inter-grain [64].

5.4.8 Interpretation of TS-GO and TU-GO results

TU-GO samples have greater Tc's than TS-GO samples. However, the TU-GO samples seem to have a maximum doping concentration of 0.7 %wt., were as doping with TS-GO doping concentrations can go above 0.7 %wt..

As mentioned, doping YBCO with GO has seen an increase in T_{Cmid} above 93 K in this and other research. Previously offered explanations for this increase have been attributed to an increase in oxygen due to GO doping. This explanation contradicts the maximum T_C = 93 K from optimum oxygen annealing single crystal YBCO experiments.

From our research it was found that Mn impurities are introduced to YBCO material via GO doping. This led to MnO_2 doping experiments of YBCO, which confirmed Mn doping increased T_C above 93 K. This is the first recorded explanation citing the presence of Mn as the reason for an increase in T_C in GO doped YBCO experiments.

Current hypotheses regarding YBCO T_C values above 93 K when doping YBCO with Mn oxides are attributed to the creation of mobile holes that populate the copper oxide planes [32] found in YBCO, or improved orthorhombicity [29] [32].

The lattice strain seen in Table 5:2, of TS-GO doped and TU-GO doped samples all show a decrease when compared to the control YBCO sample. This suggests that there are fewer defects in the crystal structure. Analyzing the T_C values of doped TS-GO and TU-GO samples against lattice 'a' and 'b' parameters (Table 5:2) reveals a noticeable trend of T_C increasing with an increase in the CuO_2 planes' area (a x b), which is plotted in Figure 5:13. This is not surprising as superconductivity occurs in the CuO_2 planes, hence structural parameters of these planes may affect T_C.

We propose this increase in area trend is associated with the CuO_2 planar buckling angle, which

is a measure of the buckling of the plane i.e., where plane oxygen atoms are out of the plane of the copper atoms. A suppression of this planar feature, which induces a change in electronic structure, has been linked to an increase in T_C [65]. In the cuprate superconductor family, the increase of T_C is observed with the increase in the number of CuO_2 planes per unit cell up to n = 3 (n is the number of CuO_2 planes per unit cell), for n > 3 the T_C starts to decrease. There also exists a link between T_C and the flatness of the CuO_2 planes, for example, Hg cuprate superconductors with the highest T_C = 135 K has the flattest CuO_2 planes.

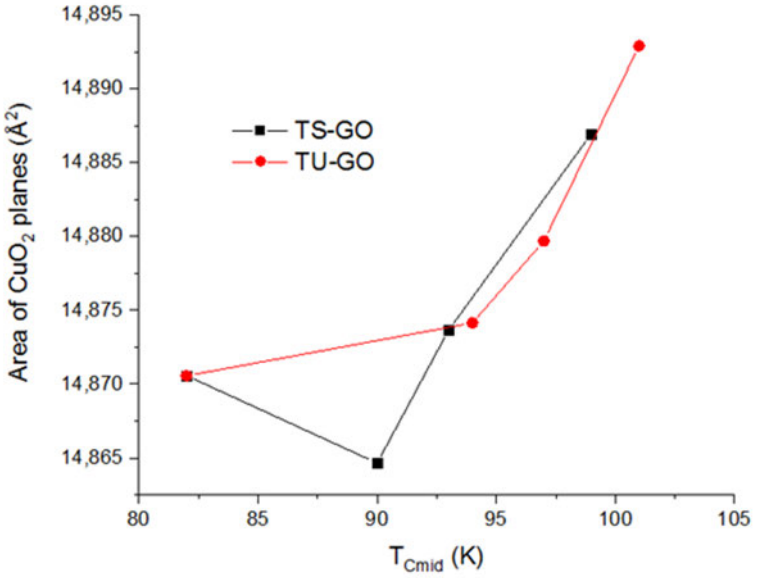

Figure 5:13: Relationship between T_C and the area of CuO_2 planes.

5.5 Conclusion

The T_C of TU-GO and TS-GO doped samples is seen to increase with increasing doping concentration in the range of 0.1 - 0.7 %wt. This results in a maximum T_C of 101 K and 99 K in the 0.7 %wt. TU-GO and TS-GO doped samples respectively. The oxygen content in the samples do increase with GO doping but the increase of T_C above 93 K is not fully explained by the increase in oxygen content.

Samples' T_{Cmid} were achieved using ρ vs. T measurements and confirmed with magnetic measurements.

XRD spectrum results show no evidence of the formation of other YBCO phases other than the Y-123 in TS-GO and TU-GO doped samples. This rules out phases with T_C great-er than 93 K such as Y124 under pressure.

EDX showed the presence of manganese in TS-GO and TU-GO dopant material. Magnetic manganese impurities formed in TS-GO and TU-GO doped YBCO samples. The impurities were confirmed magnetic with a magnet, and they consisted of oxygen and manganese.

To show a direct link with Mn and the change in T_C, YBCO was doped with MnO_2 and Mn_3O_4 in 0.1 and 0.2 %wt. concentrations. The sintering profile was adjusted from the GO experiment to allow for optimum oxygenation of YBCO, which resulted in a control B sample with a T_{Cmid} = 90 K. It was observed that the T_{Cmid} was 104 K and 94 K respectively for the MnO_2 and Mn_3O_4 0.1 %wt. doped samples. T_{Cmid} was 98 K and 88 K respectively for the 0.2 %wt. MnO_2 and Mn_3O_4 doped samples. In our research we showed a T_C trend that crossed across all GO doped samples, that is, T_C increased with an increase in CuO_2 plane area. Therefore, it is concluded that the T_C for TS-GO and TU-GO doped YBCO samples is largely affected by the presences Mn impurities found in GO dopant.

References

[1] M. K. Wu, J. R. Asburn, C. J. Torng, P. H. Hor, R. L. Meng, L. Gao, Z. J. Huang, Y. Q. Wang and C. W. Chu, "Superconductivity at 93 K in a New Mixed-Phase Y-Ba-Cu-O Compound System at Ambient Pressure," *Physical Review Letters,* vol. 58, no. 9, pp. 908-910, 1987.

[2] J. MacManus-Driscoll and S. Wimbush, "Future Directions for Cuprate Conductors," *IEEE Transactions on Applied Superconductivity,* vol. 21, no. 3, pp. 2495-2500, 2011.

[3] B. Sahoo, K. L. Routray, G. C. Mirdha, S. Karmakar, A. K. Singh, D. Samal and D. Behera, "Investigation of microhardness and superconducting parameters of CNTs blended YBCO superconductor," *Ceramics International,* vol. 45, pp. 22055 - 22066, 2019.

[4] Y. Slimani, M. A. Almessiere, E. Hannachi, M. Mumtaz, A. Manikandan, A. Baykal and F. B. Azzouz, "Improvement of flux pinning ability by tungsten oxide nanoparticles added in $YBa_2Cu_3O_y$ superconductor," *Ceramics International,* vol. 45, no. 6, pp. 6828 - 6835, 2019.

[5] S. Hamideh, S. S. Hosseini, S. S. Ghotb, B. H. Sichani and P. Sepideh, "Magnetic doping effects on the superconductivity of $Y_{1-x}M_xBa_2Cu_3O_{7-\delta}$ (M = Fe, Co, Ni)," *Ceramics International,* vol. 47, pp. 10635 - 10642, 2021.

[6] S. A. Alotaibi, Y. Slimani, E. Hannachi, M. A. Almessiere, G. Yasin, F. O. Al-qwairi, M. Iqbal and F. B. Azzouz, "Intergranular properties of polycrystalline $YBa_2Cu_3O_{7-\delta}$ superconductor added with nanoparticles of WO_3 and $BaTiO_3$ as artificial pinning centers," *Ceramics International,* vol. 47, no. 24, pp. 34260 - 34268, 2021.

[7] H. Huhtinen, V. P. S. Awana, A. Gupta, H. Kishan, R. Laiho and A. V. Narlikar, "Pinning centres and enhancement of critical current density in YBCO doped with Pr, Ca and Ni," *Superconducting Science and Technology,* vol. 20, pp. S159 - S166, 2007.

[8] O. Cicek and K. Yakinci, "Enhanced superconducting properties of multi-wall carbon nanotubes added YBCO-123 superconducting system," *Journal of Molecular Structure,* vol. 1211, 2020.

[9] E. Hannachi, M. A. Almessiere, Y. Slimani, A. Baykal and F. B. Azzouz, "AC susceptibility investigation of YBCO superconductor added by carbon nanotubes," *Journal of Alloys and Compounds,* vol. 812, p. 152150, 2020.

[10] E. Hannachi, M. A. Almessiere, Y. Slimani, R. B. Alshamrani, G. Yasin and F. B. Azzouz, "Preparation and characterization of high- Tc $(YBa_2Cu_3O_{7-\delta})1-x/(CNTs)x$ superconductors with highly boosted superconducting performances," *Ceramics International,* vol. 47, no. 16, pp. 23539-23548, 2021.

[11] N. A. Khalid, M. M. A. Kechik, N. A. Baharuddin, C. S. Kien, H. Baqiah, L. K. Pah, A. H. Shaari, Z. A. Talib, A. Hashim, M. Murakami and M. Miryala, "Carbon nanofibers addition on transport and superconducting properties of bulk $YBa_2Cu_3O_{7-x}$ material prepared via co-precipitation," *Journal of Material Science : Mater Electron,* vol. 31, pp. 16983-16990, 2020.

[12] S. Falahati, S. Dadras and J. Mosqueira, "Graphene doping effects on the magnetic and transport

properties of $YBa_2Cu_3O_{7-\delta}$ high temperature superconductor," *Physica B: Physics of Condensed Matter* , vol. 644, 2022.

[13] M. Z. Gaffoor, A. L. L. Jarvis, J. C. Archer and S. Perumal, "Effect of Graphene Oxide Doping on Bulk High Temperature Superconductors For Power Applications," in *SAUPEC/RobMech/PRASA*, Bloemfontein, 2019.

[14] S. Dadras, S. Falahati and S. Dehghani, "Effects of graphene oxide doping on the structural and superconducting properties of $YBa_2Cu_3O_{7-x}$," *Physica C,* vol. 548, pp. 65-67, 2018.

[15] B. Sahoo, A. K. Singh and D. Behera, "Graphene Oxide Modified Superconducting and Elastic Parameters of YBCO Superconductor," *Material Chemistry and Physics*, vol. 240, p. 122252, 2020.

[16] M. Z. Gaffoor and A. L. L. Jarvis, "Comparison of the Effect of Graphene and Graphene Oxide Doping on YBCO," *Journal of Physics:Conference Series,* vol. 1559, pp. 20-28, 2020.

[17] S. Dadras, S. Dehghani, M. Davoudiniya and S. Falahati, "Improving Superconducting Properties of YBCO High Temperature Superconductor by Graphene Oxide Doping," *Materials Chemistry and Physics,* vol. 193, pp. 496-500, 2017.

[18] B. Sahoo and D. Behera, "Study of Transport and Elastic Properties of YBCO Superconductors by Inclusions of GnPs," *Physica C : Superconductivity and its Applications,* vol. 578, p. 1353748, 2020.

[19] B. Sahoo, K. L. Routray, D. Samal and D. Behera, "Effects of Artificial Pinning Centers on YBCO High Temperature Superconductors Through Substitution of Graphene Nano-platelets," *Materials Chemistry and Phsyics,* vol. 223, pp. 784-788, 2019.

[20] J. Wang, Q. Zhang, C. Liu and X. Zhang, "Improvement of the pinning property in $YBa_2Cu_3O_{7-X}$ films below 35 K by doping with graphene oxide," *AIP Advances,* vol. 9, no. 1, 2018.

[21] S. Falahati, S. Dadras and J. Mosqueira, "Investigation of the Magnetic and Transport Properties of $YBa_2Cu_3O_{7-\delta}$ High Temperature Superconductor Doped with Graphene Oxide," *Journal of Superconductivity and Novel Magnetism* , vol. 32, pp. 3755 - 3760, 2019.

[22] M. Z. Shoushtari, M. Akbari and Y. Hajati, "Study of $YBa_2Cu_3O_{7-\delta}$ Superconductor/Graphene Oxide Composite," *Journal of Superconductivity and Novel Magnetism,* vol. 31, pp. 2733 - 2739, 2018.

[23] K. Wei, K. Ing, M. S. Hamdan, S. Radiman and R. Adb-Shukor, "AC Susceptibility and Superconducting Properties of Graphene Added YBa2Cu3O7−d," *Journal of Superconductivity and Novel Magnetism,* vol. 31, pp. 2699 - 2703, 2018.

[24] P. Benzi, E. Bottizzo and N. Rizzi, "Oxygenation Determination from Cell Dimentions in YBCO Superconductors," *Journal of Crystal Growth,* vol. 269, no. 2-4, pp. 625-629, 2004.

[25] L. Pintschovius, D. Reznik, W. Reichardt, Y. Endoh, H. Hiraka, J. M. Tranquada, H. Uchiyama, T. Masui and S. Tajima, "Oxygen phonon branches in $YBa_2Cu_3O_7$," *Physical Review B,* vol. 69, no. 21, p. 214506, 2004.

[26] W. S. Hummers and R. E. Offeman, "Preparation of Graphitic Oxide," *Journal of the American Chemical Society,* vol. 80, no. 6, p. 1339, 1958.

[27] C. Wong, Z. Sofer, M. Kubešová, J. Kucera, S. Matejková and M. Pumera, "Synthetic Routes

Contaminate Graphene Materials with a Whole Spectrum of Unanticipated Metallic Elements," *Proceedings of the National Academy of Sciences of the United States of America,* vol. 111, no. 38, pp. 13774-9, 2014.

[28] A. M. Panich, A. Shames and N. A. Sergeev, "Paramagnetic Impurities in Graphene Oxide," *Applied Magnetic Resonance,* vol. 44, pp. 107-116, 2012.

[29] A. Salama, M. El-Hofy, Y. Rammah and M. Elkhatib, "Effect of Magnetic and Nonmagnetic Nano Metal Oxides Doping on the Critical Temperature of a YBCO Superconductor," *Advanced Natural Science: Nanoscience and Nanotechnology,* vol. 6, no. 4, p. 045013, 2015.

[30] A. Salama, M. El-Hofy, Y. Rammah and M. Elkhatib, "The Influence of Magnetic Nano Metal Oxides Doping on Structure and Electrical Properties of YBCO Superconductor," *Advances in Natural Sciences: Nanoscience and Nanotechnology,* vol. 7, no. 1, p. 015011, 2016.

[31] Y. Rammah, A. Salama and M. Elkhatib, "Magnetic Moment and its Correlation with the Critical Temperature in YBCO," *Interceram,* vol. 68, no. 5, pp. 34 - 41, 2019.

[32] A. Ponchanthai, T. Nilkamjon, S. Sujinnaparm, T. Kruaehong, S. Tiyasri, W. Wongphakdee and P. Udomsamuthirun, "The Variation of Superconducting Critical Temperature of the Mn_3O_4 Doped- and Mn_3O_4 Composited-Y145 Superconductor," *Progress in Applied Scince and Technology,* vol. 10, no. 2, pp. 28-36, 2020.

[33] D. Tinsley and J. Sharp, "Thermal Analysis of Manganese Dioxide in Controlled Atmospheres," *Journal of Thermal Analysis,* vol. 3, no. 1, pp. 43-48, 1971.

[34] D. C. Marcano, D. V. Kosynkin, J. M. Berlin, A. Sinitskii, Z. Sun, A. Slesarev, L. B. Alemany, W. Lu and J. M. Tour, "Improved Synthesis of Graphene Oxide," *ACS NANO,* vol. 4, no. 8, p. 4806–4814, 2010.

[35] Y. Qiu, F. Guo, R. Hurt and I. laots, "Explosive thermal reduction of graphene oxide-based materials: Mechanism and safety implications," *Carbon,* vol. 72, pp. 215-223, 2014.

[36] F. Kim, J. Luo, R. Cruz-Silva, L. J. Cote, K. Sohn and J. Huang, "Self-Propagating Domino-like Reactions in Oxidized Graphite," *Advanced Functional Materials,* vol. 20, no. 17, pp. 2867-2873, 2010.

[37] S. Stankovich, D. Dikin, R. Piner, K. Kohlhaas, A. Kleinhammes, Y. Jia, Y. Wu, S. Nguyen and R. Ruoff, "Synthesis of graphene-based nanosheets via chemical reduction of exfoliated graphite oxide," *Carbon,* vol. 45, no. 7, pp. 1558-1565, 2007.

[38] M. Z. Gaffoor, A. L. L. Jarvis and S. Perumal, "Comparison of Graphene Oxide and Reduced Graphene Oxide Doping on YBCO For Power Applications," in *Southern African Universities Power Engineering Conference/Robotics and Mechatronics/Pattern Recognition Association of South Africa (SAUPEC/RobMech/PRASA),* Bloemfontein,South Africa, 2020.

[39] "Crystallographic Resources," International Union of Crystallography, 15 October 2021. [Online]. Available: https://www.iucr.org/resources/other-directories/software/maud. [Accessed 8 July 2022].

[40] S. S. Babet and A. L. L. Jarvis, "A DSP-enhanced AC susceptometer for characterisation of superconductors," in *Africon,* Pointe aux Piments, Mauritius, 2013.

[41] M. S. Eluyemi, M. A. Eleruja, A. V. Adedeji, B. Olofinjana, O. Fasakin, O. O. Akinwunmi, O. O. Ilori, A. T. Famojuro, S. A. Ayinde and E. O. B. Ajayi, "Synthesis and Characterization of Graphene Oxide and Reduced Graphene Oxide Thin Films Deposited by Spray Pyrolysis Method," *Graphene,* vol. 5, no. 3, pp. 143-145, 2016.

[42] H. R. Thomas, S. P. Day, W. E. Woodruff, C. Valles, R. J. Young, I. A. Kinloch, G. W. Morley, J. V. Hanna, N. R. Wilson and J. P. Rourke, "Deoxygenation of Graphene Oxide: Reduction or Cleaning?," *Chemistry of Materials,* vol. 25, no. 18, pp. 3580 - 3588, 2013.

[43] R. Muzyka, S. Drewniak, T. Pustelny, M. Chrubasik and G. Gryglewicz, "Characterization of Graphite Oxide and Reduced Graphene Oxide Obtained from Different Graphite Precursors and Oxidized by Different Methods Using Raman Spectroscopy," *materials,* vol. 11, no. 7, p. 1050, 2018.

[44] P. Sreekanth, S. Pranitha, P. Rose and P. Reji, "White Light Z-scan Measurements of Ultrafast Optical Nonlinearity in Reduced Graphene Oxide Nanosheets in the 400–700nm Region," *Applied Physics Letters,* vol. 107, no. 5, p. 051104, 2015.

[45] F. Johra, J. Lee and W. Jung, "Facile and safe graphene preparation on solution based platform," *Journal of Industrial and Engineering Chemistry,* vol. 20, no. 5, p. 2883–2887, 2014.

[46] M. Sohail, M. Saleem, S. Ullaha, N. Saeed, A. Afridi, M. Khan and M. Ari, "Modified and improved Hummer's synthesis of graphene oxide for capacitors applications," *Modern electronic materials,* vol. 3, no. 3, pp. 110-116, 2017.

[47] S. Ozcan, A. Guler, T. Cetinkaya, M. O. Guler and H. Akbulut, "Freestanding Graphene/MnO_2 Cathodes for Li-Batteries," *Beilstein Journal of Nanotechnolgy,* vol. 8, no. 1, pp. 1932-1938, 2017.

[48] V. Sannasi and K. Subbian, "Influence of Moringa Oleifera Gum on Two Polymorphs Synthesis of MnO_2 and Evalution of the Pseudocapacitance activity," *Journal Material Science: Mater Electron,* vol. 31, no. 19, pp. 7120-17132, 2020.

[49] R. Tholkappiyan, A. N. Naveen, K. Vishista and F. Hamed, "Investigation on the Electrochemical Performance of Hausmannite Mn_3O_4 Nanoparticles by Ultrasonic Irradiation Assisted Co-precipitaion Method for Supercapacitor Electrodes," *Journal of Taibah University for Science,* vol. 12, no. 5, pp. 669-677, 2018.

[50] J. S. Sherin, J. K. Thomas and J. Suthagar, "Combustion Synthesis and Magnetic Studies of Hausmannite Mn_3O_4 Nanoparticles," *International Journal of Engineering Research and Development,* vol. 10, no. 7, pp. 34-41, 2014.

[51] B. C. Smith, Infrared spectral Interpretation: A Systematic Approach, CRC Press, 1998.

[52] P. R. G. Gonçalves, H. A. Abreu and D. H. Anderson, "Stability, Structural and Electronic Properties of Hausmannite (Mn_3O_4) Surfaces and Their Interaction with Water," *The Journal oof Physical Chemistry,* vol. 122, no. 36, pp. 20841-0849, 2018.

[53] S. G. Cooke, J. Allison and R. C. Woods, "High-temperature resistivity measutements of $YBa_2Cu_3O_{7-X}$ doped with sulphur," *Solid State Communications,* vol. 112, pp. 229-233, 1999.

[54] S. Celebi, A. Ozturk, I. Karaca and U. Kolemen, "The Effect of Potassium Doping on Resistive Transitions and Transport Critical Current of Bulk YBCO high-Tc Superconductors," *Turkish Journal of Physics,* vol. 24, no. 4, pp. 567-576, 2000.

[55] M. El-Hofy, M. El-Shahawy and R. Ebrahimi, "Crystal Field Modification by Doping in HTC YBCO," *Defect and Diffusion Forum,* pp. 197- 0, May 2004.

[56] A. Mellekh, M. Zouaoui, F. B. Azzouz, M. Annabi and M. B. Salem, "Nano - Al_2O_3 particle addition effects on $YBa_2Cu_3O_y$ superconducting properties," *Solid State Communication,* vol. 140, pp. 318-323, 2006.

[57] Z. H. Wang, X. W. Zou, T. Yang, H. Zhang, J. Fang, Z. Huang, L. Qiu, J. L. Chen and S. Y. Ding, "Transport properties in melt-textured-growth-$YBa_{1.9}Na_{0.1}Cu_3O_{7-x}$ crystals," *Physica C,* vol. 366, pp. 195-202, 2002.

[58] I. Matsubara, H. Tanigawa, T. Ogura and S. Kose, "Effects of Sulfur Addition on the Superconductivity of Y-Ba-Cu-O Compound," *Japanese Journal of Applied Physics,* vol. 27, 1988.

[59] V. Antal, M. Kanuchova, M. Sefcikova, J. Kovac, P. Diko, M. Eisterer, N. Horhager, M. Zehetmayer, H. W. Weber and X. Chaud, "Influence of Al doping and oxygenation on the superconducting properties of TSMG YBCO bulks," *Journal of Physics: Conference Series,* vol. 234, p. 012002, 2010.

[60] M. Y. Li, Q. Fang, X. F. Hu, Z. Y. Liu, Y. Q. Guo, Y. M. Lu, C. Y. Bai and C. B. Cai, "Microstructures Property and Improved Jc of Eu-Doped $YBa_2Cu_{3.6}O_{7-\delta}$ Thin Films by Trifluoroacetate Metal Organic Deposition Process," *Journal of Superconductivity and Novel Magnetism,* vol. 30, pp. 1137-1143, 2016.

[61] S. Regnier, C. Alfred-Duplan, G. Vacquier and J. Marfaing, "Effect of Mn Inclusion in Superconducting YBCO-Based Composites," *Applied Superconductivity,* vol. 4, no. 112, pp. 41-51, 1996.

[62] S. Regnier and J. Marfaing, "Detailed Analysis of the Zero Critical Temperature Improvement in Mn-$YBa_2Cu_3O_{7-x}$ Composites from Electrical and Structural Studies," *Materials Science and Engineering B,* vol. 34, no. 2-3, pp. 116-123, 1995.

[63] S. Regnier and J. Marfaing, "Effect of sintering on the transport properties and microstruetures of Mn-YBCO composites," *Physica C,* vol. 235, pp. 1513-1514, 1994.

[64] D. Pelc, V. Marija, M. S. Grbić, M. Požek, G. Yu, T. Guichuan, M. Greven and N. Barišić, "Emergence of superconductivity in the cuprates via a universal percolation process," *Nature Communications,* vol. 9, no. 1, pp. 1-10, 2018.

[65] O. Chmaissem, J. D. Jorgensen, S. Short, A. Knizhnik, Y. Eckstein and H. Shaked, "Scaling of transition temperature and CuO_2 plane buckling in a high-temperature superconductor," *Nature,* vol. 397, pp. 45-48, 1999.

Chapter 6

Concluding Remarks

In this research, the T_C of YBCO has been improved due to GO and rGO doping. The increase in T_C in GO doped samples is greater than rGO doped samples due to GO having a high oxygen content or more manganese impurities The diffusion of oxygen content into the YBCO structure thus increasing the non-stoichiometric oxygen there by increasing T_C. This increase in non-stoichiometric oxygen content has been confirmed by iodometry and validated using XRD. This explanation does not explain Tc beyond 93 K.

The weak-link effect was also improved significantly in both GO and rGO doped samples. This was observed by the reduction in the R(T) foot structure in GO and rGO doped samples. This reduction in the weak-link effect is due to graphene nano-particles at grain boundaries which has been observed by TEM imaging. The conductivity of graphene is high therefore it improves grain boundary connectivity. The graphene nano-particles also increase the number of flux pinning sites. This reduction in the weak-link effect and increase in flux pinning sites allows us to deduce that there will be an improvement in J_C.

The micro-hardness of GO and rGO samples increased. The HK model best described this improvement in micro-hardness. This is attributed to GO and rGO sheets filling voids and pores between grains thus reducing porosity, improving grain boundary connectivity and preventing dislocation motion resulting in locking of defects thus preventing crack propagation. This was confirmed by porosity calculations and by the decrease in lattice strain. The mechanical parameters B, E, Y and K_{IC} were enhanced by GO and rGO doping's. The improvement in mechanical parameters were greater in GO doped samples than in rGO samples. Due to the oxygen content being higher in GO doped samples than in rGO doped samples.

It was also observed that there was an increase in T_C to temperatures above 93 K in certain GO doped samples. This increase above 93 K has been observed by a number of research groups mentioned in references [27] [28] in Chapter 1, with only the above increase in oxygen explanation. The increase in T_C above 93 K cannot be attributed to an increase in non-stoichiometric oxygen content as the maximum T_C of YBCO at optimum oxygenation is 93 K, as observed in single crystal oxygenation experiments.

Therefore there had to be another mechanism acting in conjunction with the increasing oxygen content allowing for this increase. This increase above 93 K was explained by the combined effect of the increasing non-stoichiometric oxygen content and the formation of Mn_3O_4 magnetic nano-particle impurities. The formation of these manganese impurities is a result of producing GO via the Hummers method with additional potassium permanganate and the sintering process. The mechanism hypothesized for this increase in T_C above 93 K is that the manganese impurities increase the buckling angle of the of the CuO_2 planes which in turns increases the area and enhances the flatness of CuO_2 planes. The enhancement in the flatness of the CuO_2 planes has been seen to enhance T_C.

Future work to be carried out is to determine the exact position in which these manganese particles assume in the YBCO crystalline structure and carry out measurements to calculate the buckling angle of the CuO_2 planes in GO, rGO and manganese oxide doped YBCO.

Appendix A – R vs. T Experimental Procedure

In order to carry out R vs. T measurements in FC and ZFC conditions an experimental stage was designed and implemented. This can be seen in Figure A:1 attached to the cold head of a PT415 CryoMech pulse tube cryo-cooler which was used to cool the stage. The stage consisted of a PT100 temperature sensor, a 32 W-50 Ω heater and Helmholtz coils seen in Figure A:2.

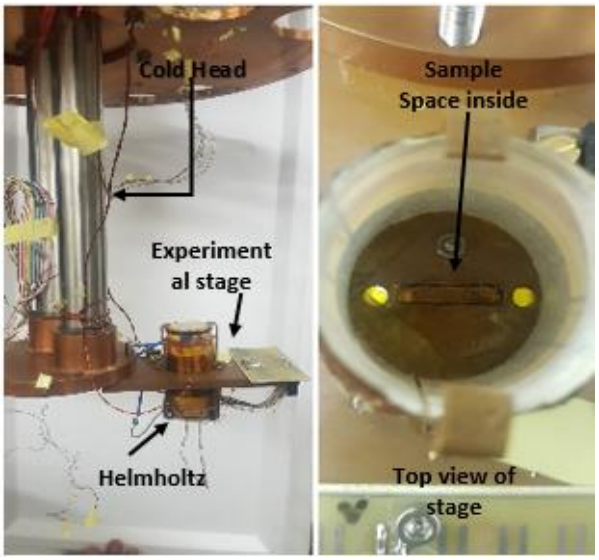

Figure A:1 : Experimental stage attached to cold head

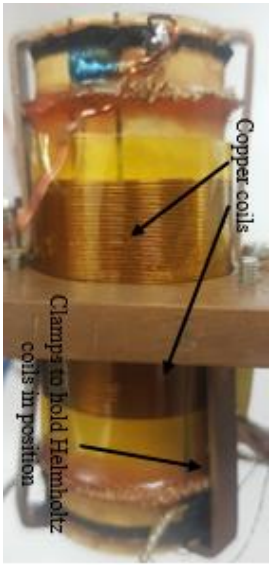

Figure A:2 : Helmholtz coils

The heater and the temperature sensor allowed for temperature control of the stage by using a Lakeshore temperature controller seen in Figure A:4 and Figure A:5.

Helmholtz coils were used to generate a magnetic field in order to carry out measurements in FC conditions. These coils were designed with a diameter of 26 mm and 124 turns per coil. Figure A:3 shows the calibration of the coils.

$$B = \left(\frac{4}{5}\right)^{\frac{3}{2}} \frac{\mu_0 NI}{R} \qquad \text{(A.1)}$$

Equation A.1 shows the relationship between the current flowing through the coils and magnetic flux density produced by the coils. In the equation N is the number of turns in the coil, B is the magnetic flux density, μ_0 is the permeability of free space, I is the current flowing through the coils and R is radius of the coil.

.

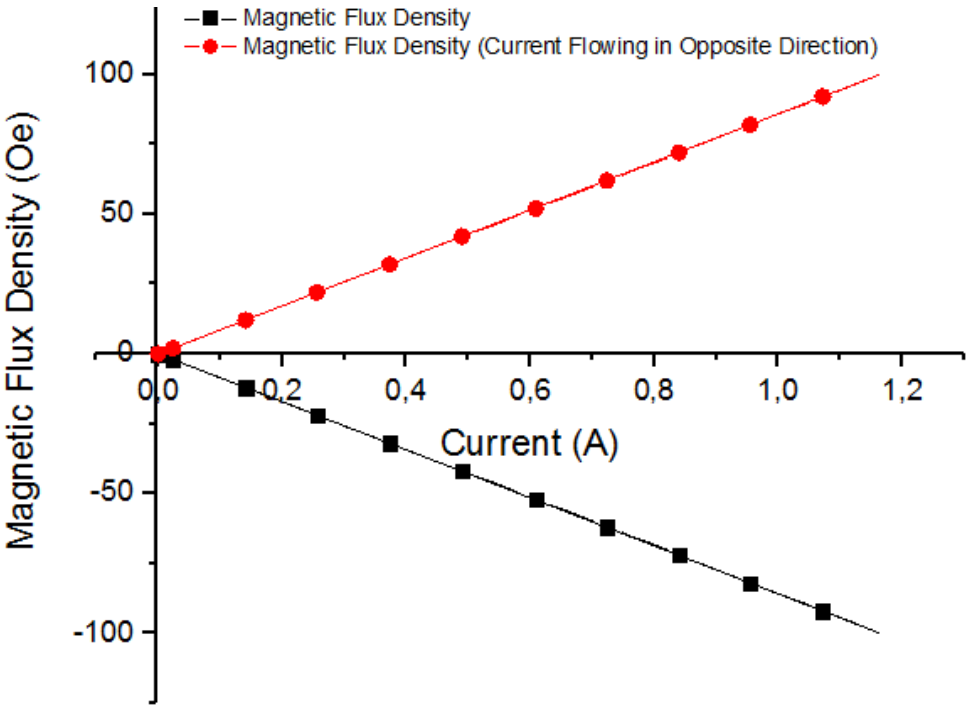

Figure A:3 : Graph showing the relationship between the amount of current passing through the coil and magnetic field generated by the coil.

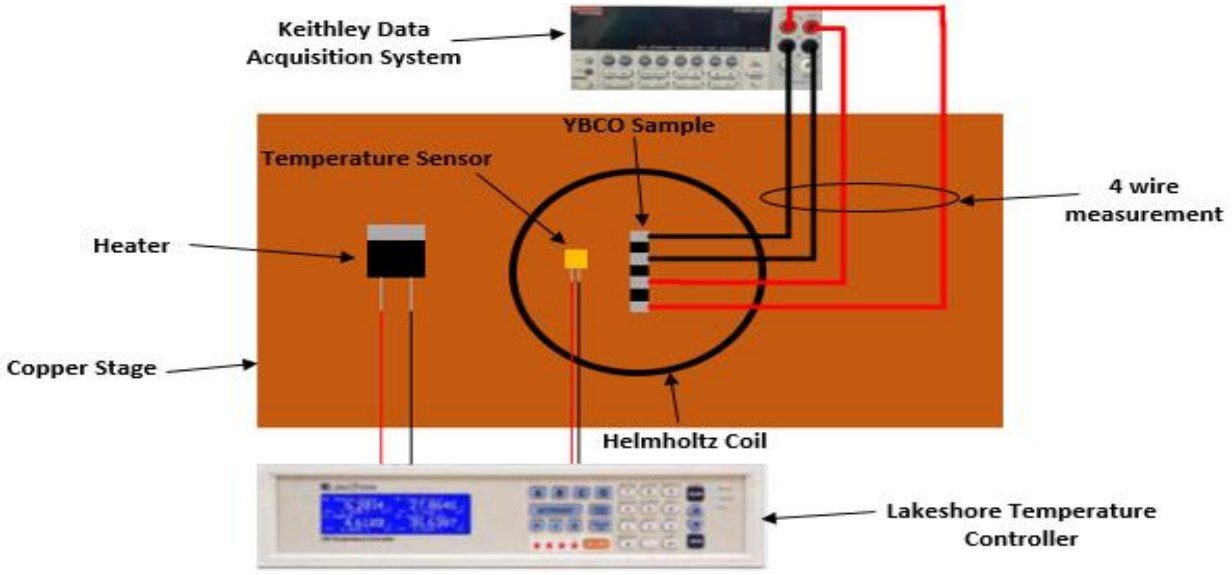

Figure A:4 : Experimental stage in ZFC conditions

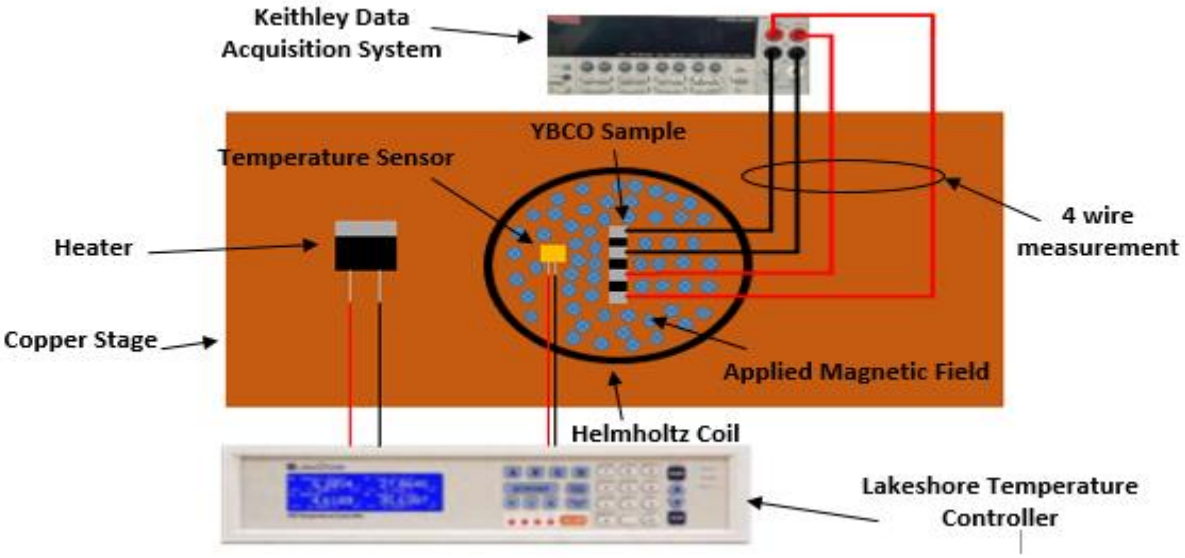

Figure A:5 : Experimental stage in FC conditions

Diagrams showing the functioning of the stage in ZFC and FC conditions can be seen in Figure A:4 and Figure A:5

Appendix B – AC Susceptibility Experimental Procedure

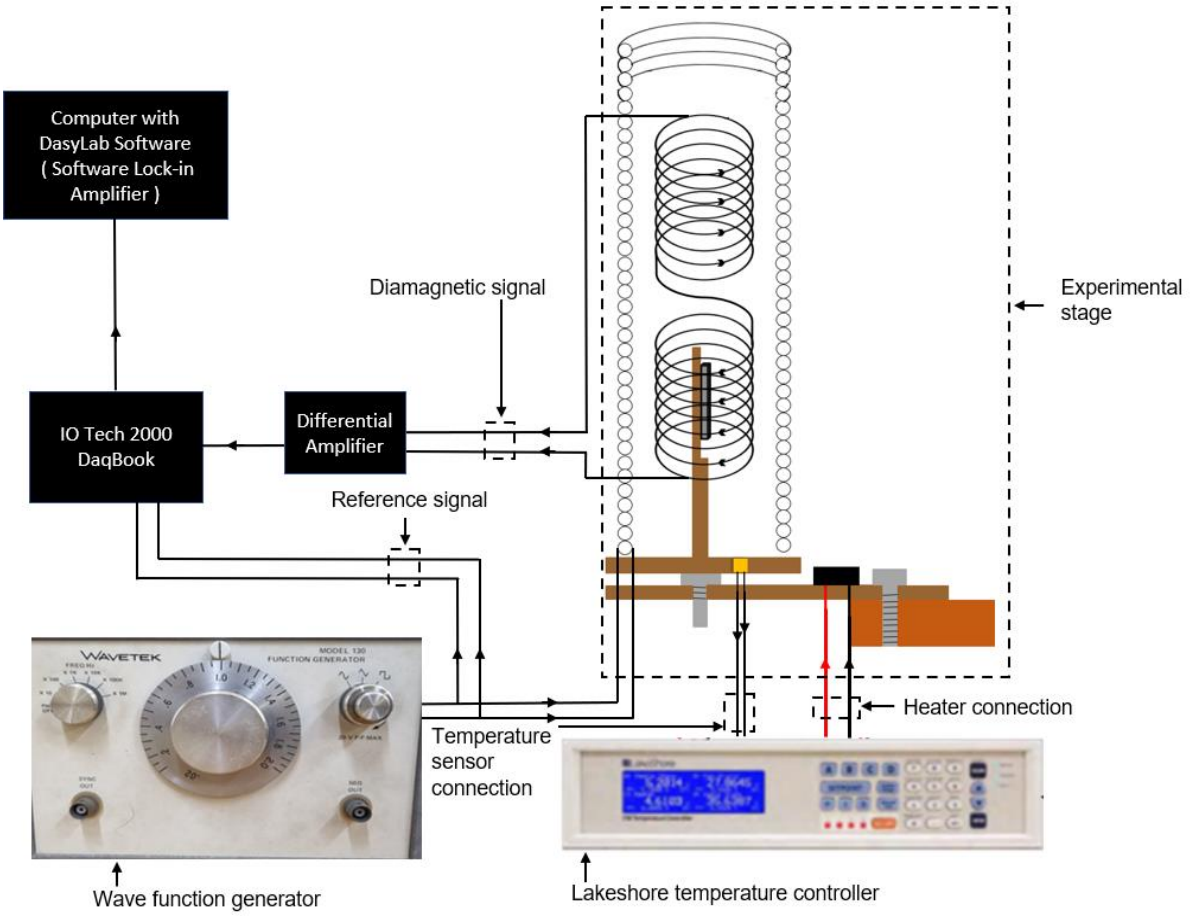

Figure B:1: Diagram of AC susceptibility experiment.

The AC susceptibility measurement was carried out to obtain χ' vs T. This was done using the experimental setup shown in Figure B:1. The wave function generator is used to supply a sine wave of frequency 1 kHz. That drives the primary coil shown in Figure B:1, Figure B:2 and Figure B:7. The temperature of the stage is controlled using a Lakeshore temperature controller shown in Figure B:1 in combination with a PT100 temperature sensor and 50 Ω 20 W heater which can be seen in Figure B:1, Figure B:2 and Figure B:8

The experimental stage consists of 3 coils a primary coils, reference coil and a sample coil which can be seen in Figure B:7 and Figure B:8. The dimensions of these coils is shown in Figure B:4 and Figure B:5. The primary coils were designed with 650 turns and the reference and sample coil has 150 turns each. The reference and sample coil are wound in opposite directions for current to flow in a clockwise and ani-clockwise direction. This allows for equal and opposite voltage signals which balance each other out resulting in a signal of zero in the presence of no superconductor.

In the presence of a superconductor a diamagnetic signal is generated. This signal is thereafter passed through a differential amplifier which can be seen in Figure B:1 and Figure B:3. This differential amplifier was designed using an INA128P instrumentational amplifier. The purpose of the differential amplifier is to reduce noise and amplify the signal. All common mode noise is removed due to the fact that the differential amplifier only reacts to the difference in the 2 signals, this can be seen by output equation B.1.

$$V_{output} = G(V_{in}^{+} - V_{in}^{-}) \tag{B.1}$$

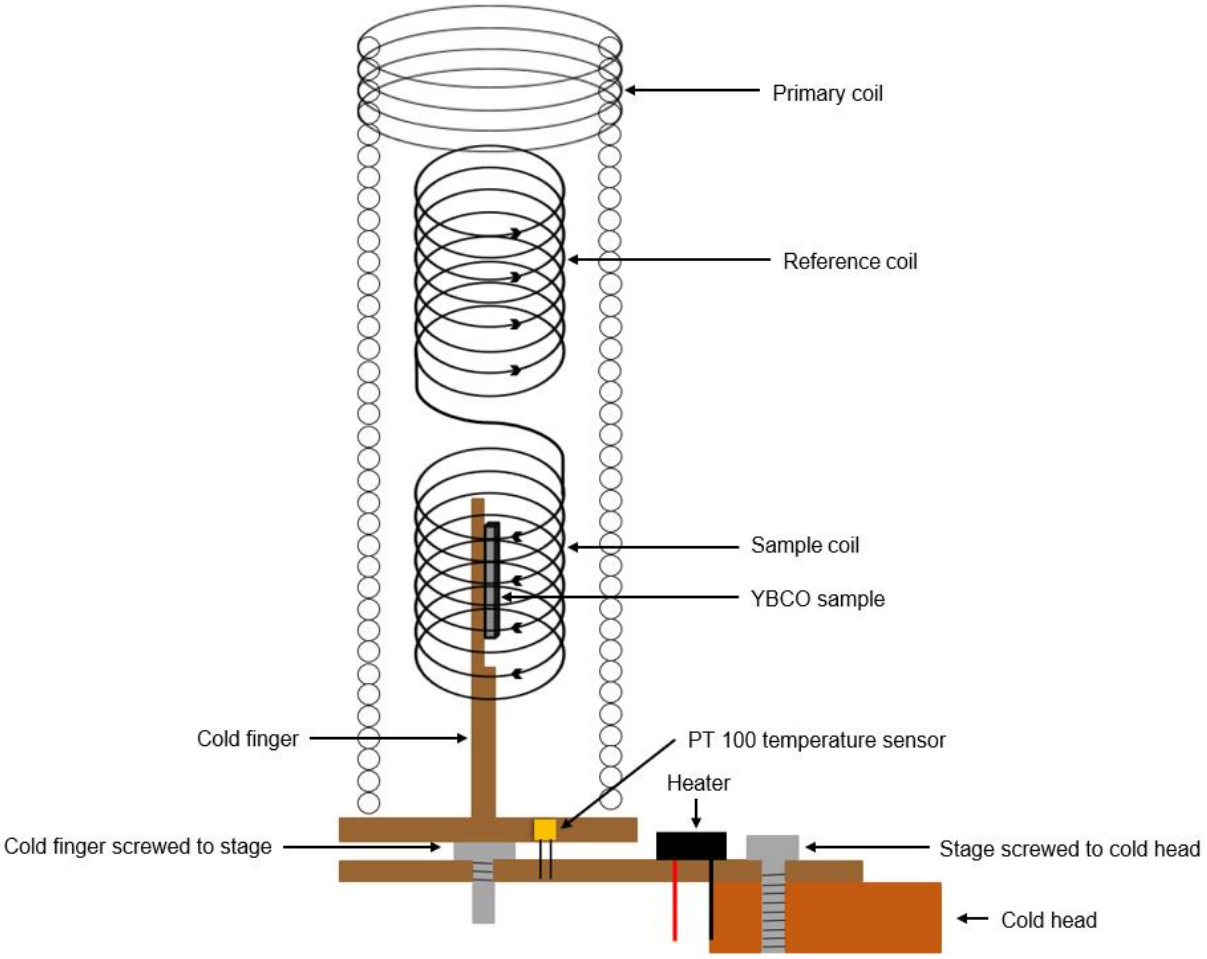

Figure B:2: Experimental stage for AC susceptibility experiment.

In equation B.2 G is the gain of the amplifier. For the amplifier designed R_G is equivalent to 470 Ω (shown in Figure B:3) which results in gain of 106.38.

$$G = 1 + \frac{50\ K\Omega}{R_G} \tag{B.2}$$

The output of the differential amplifier and reference signal is measured by the IO tech 2000 Daqbook in combination with DasyLab 10 software. This can be seen in Figure B:1. These signals were thereafter processed using a software lock-in amplifier which acts as a discriminatory voltmeter. This means that the lock-in amplifier will measure the in phase and out of phase components of signals only at the reference signal frequency and all other

frequencies will be blocked.

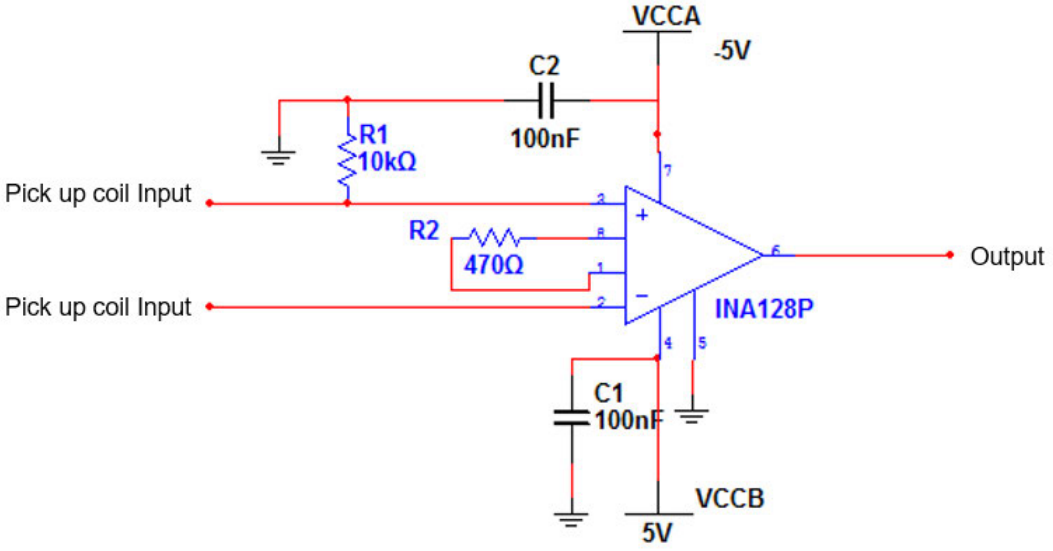

Figure B:3: Circuit diagram of differential amplifier

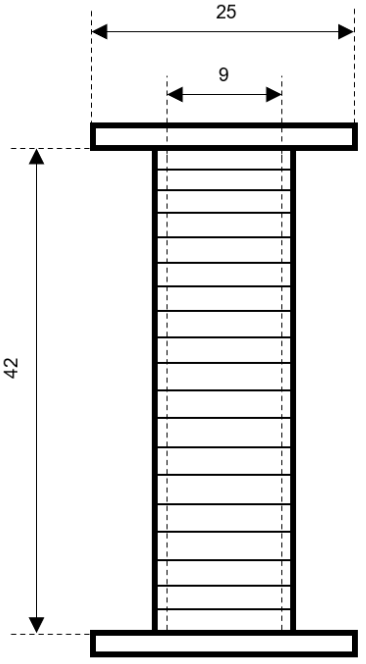

Figure B:3: Dimensions of primary coil (mm)

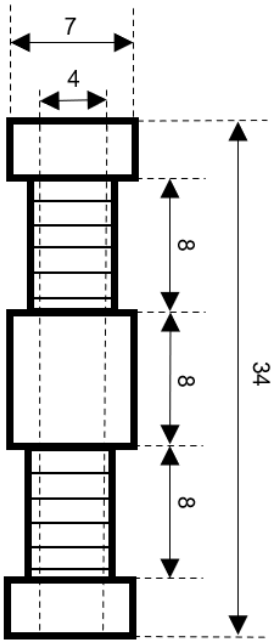

Figure B:4: Dimensions of sample and reference coil (mm)

In the lock-in amplifier the input diamagnetic signal is passed through a bandpass filter. Thereafter the mixer multiplied the reference signal which has been phase shifted. This can be seen in Figure B:6. The output of the mixer was passed through a lowpass filter to extract real and imaginary components at the reference frequency.

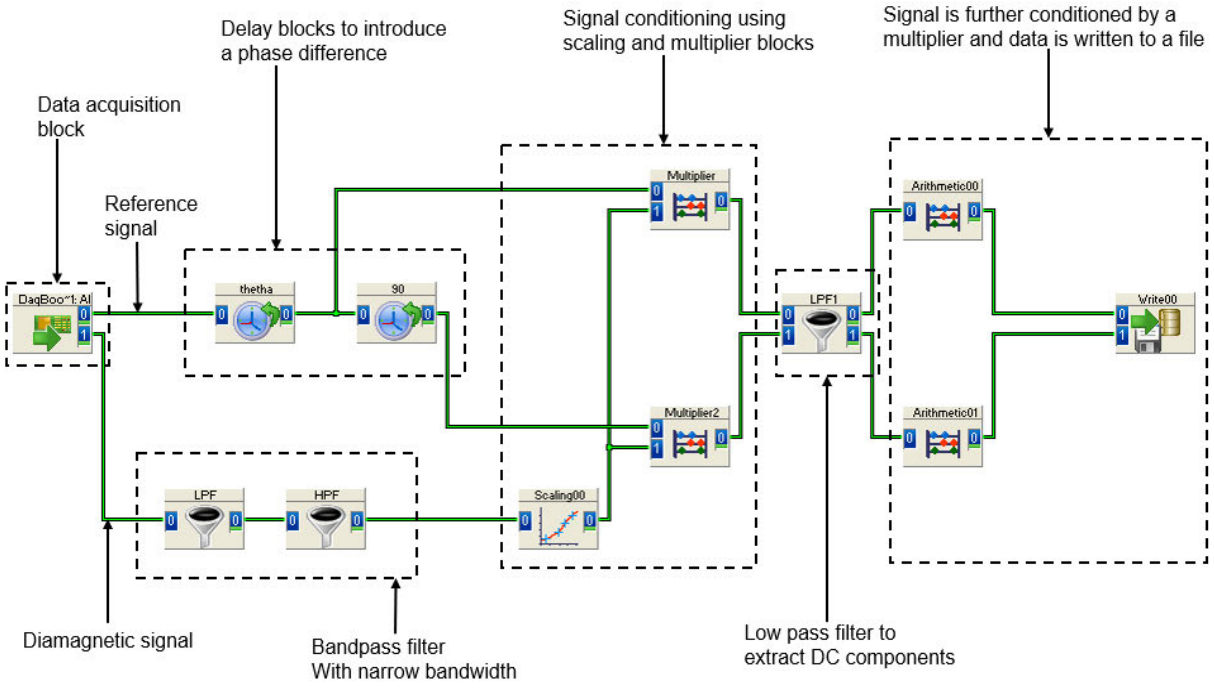

Figure B:5: Block diagram of lock-in amplifier

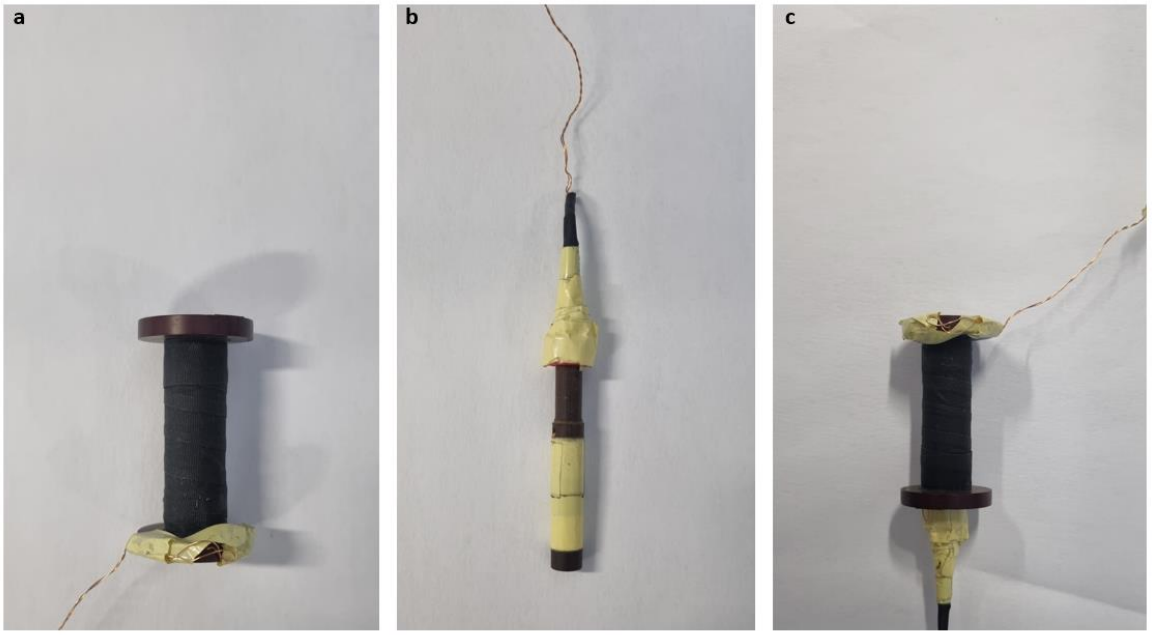

Figure B:6: a) Primary coil b) Reference and sample coil c) Reference and sample coils inside primary coil

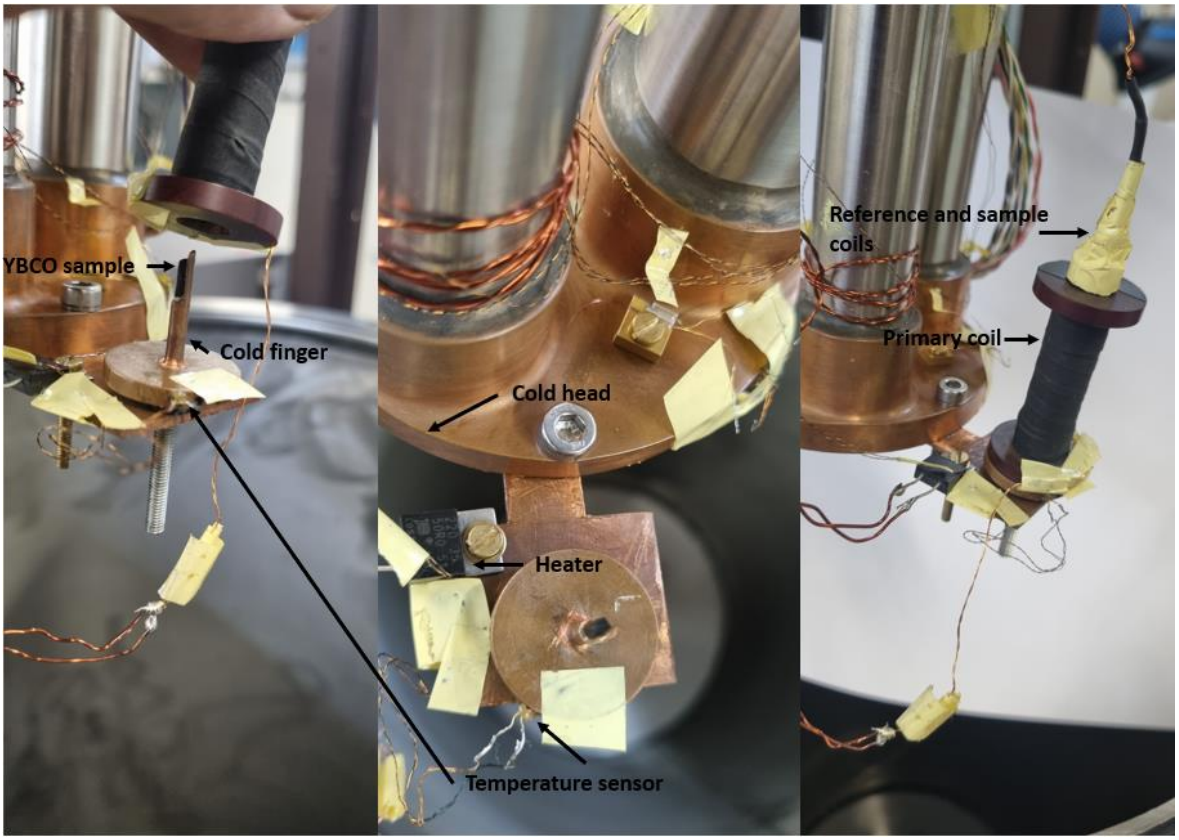

Figure B:7: Experimental stage for AC susceptibility experiment